UNIVERSITY OF CALIFORNIA

Los Angeles

A Study on the Characteristics of Liquid Based Mechanical Interfaces

A dissertation submitted in partial satisfaction

of the requirements for the degree

Doctor of Philosophy in Mechanical Engineering

by

Jinda Zhuang

2016

ABSTRACT OF THE DISSERTATION

A Study on the Characteristics of Liquid Based Mechanical Interfaces

by

Jinda Zhuang

Doctor of Philosophy in Mechanical Engineering

University of California, Los Angeles, 2016

Professor Yongho Ju, Chair

Most existing approaches for flexible and stretchable electronics are based on directly bonding semiconductor devices onto stretchable substrates. They require fragile 3D interconnects, stretchable conducting polymeric materials, or liquid metals to accommodate mechanical deformation while often providing limited optoelectronic functionality and mechanical robustness. An intriguing alternative strategy for realizing flexible electronics is to integrate brittle semiconductor chips onto flexible substrates using capillary confined microscale

liquid bridges as mechanical interfaces. This approach allows the use of standard electronic or optoelectronic devices fabricated on “thick” substrates as opposed to simplified circuits built on highly customized ultra-thin semiconductor membranes.

For the first part of this thesis, studies on the statics and dynamics of the liquid based mechanical interface for rigid devices are present. We first introduce a design of the mechanical interface using capillary confined microscale liquid bridges between a rigid component and a flexible substrate. Numerical modeling methods are developed and validated by corresponding experiments to precisely predict the liquid bridge topologies, capillary forces under various loading conditions. This work establishes the engineering and scientific foundation for fabrication and optimization of such liquid interfaces for flexible electronics in future research.

We then continue to investigate the dynamics of such mechanical liquid interfaces. A liquid bridge is the basic element of the mechanical liquid interface. The dynamic behaviors of a liquid bridge confined between two coaxial disks are comprehensively investigated through a combined modeling and experimental study. The effects of the stretching velocity, liquid properties, and liquid volume on the dynamics of liquid bridges are systematically studied to provide a direct experimental validation of our numerical model as well as offer further physical insights for stretching velocities as high as 3 m/s.

We also present a numerical modeling approach that fully captures the dynamics of a capillary self-alignment process, where a solid object floating on a liquid bridge is aligned by capillary forces of the underlying liquid bridge onto the target position. By directly coupling fluid dynamics, solid mechanics along with the additional line friction from moving contact line, model predictions have shown good agreement with experimental measurements. This work

provides an experimentally validated modeling approach and physical insights to help establish foundation for systematic further studies and applications of capillary self-alignment and other related applications of the mechanical liquid interfaces.

The second part of this thesis discusses the applications, designs and experimental characterizations of such mechanical interface for flexible devices. We introduce a design concept for a deployable planar microdevice based on a thin film liquid bridge and the modeling and experimental validation of its mechanical behaviors. We develop and experimentally validate theoretical models based on the energy minimization approach to examine the conformality and figures of merit of the device. This study establishes an early foundation for the mechanical design of this and related deployable planar microdevice concepts.

We lastly present a tunable platform for incorporating flexible and yet *non-stretching* device layers on a hemispherical structure. A mechanical model is developed to elucidate the dependence of the conformality of the petal structures on their elastic modulus and thickness and the liquid surface tension. This platform will enable facile integration of *non-stretching* electronic and optoelectronic components prepared using established planar fabrication techniques on tunable hemispherical surfaces.

The dissertation of Jinda Zhuang is approved.

Chang-Jin Kim

Nasr M. Ghoniem

Qibing Pei

Yongho Ju, Committee Chair

University of California, Los Angeles

2016

TABLE OF CONTENTS

LIST OF FIGURES

ACKNOWLEDGEMENTS

This work would not have been possible without the support of many people. First and foremost, I would like to express my sincere appreciation and gratitude to my advisor, Dr. Yongho Ju, for his enthusiastic guidance and insightful advices throughout my PhD research. I would also like to thank the committee members, Dr. Nasr Ghoniem, Dr. Qibing Pei, and Dr. Chang-Jin Kim, for their valuable suggestions and encouragement.

I would like to thank my former and current colleagues in UCLA Multiscale Thermosciences Laboratory: Youngsuk Nam, Gillwan Cha, Tanye Tang, Katie Bulgrin, Stephen Sharratt, Yujia Zhan, Yanbing Jia, Cheng Peng, Yang Shen, Zezhi Zeng, Yide Wang, Chao Fan, Navid dehdari ebrahimi and Abolfazl Sadeghpour for their help during my stay at UCLA.

Last but not least, I would like to thank my family and friends for their love, encouragement and continued support over the years. My deepest gratitude goes to my parents and my wife for their unconditional love and support.

VITA

2007-20111	B.S., Mechanical Engineering Tsinghua University Beijing, China
2011-2016	Graduate Student Researcher/Teaching Assistant Mechanical and Aerospace Engineering Department University of California, Los Angeles

PUBLICATIONS

Journal Publications

J. Zhuang and Y. S. Ju, "A Combined Experimental and Numerical Modeling Study of the Deformation and Rupture of Axisymmetric Liquid Bridges under Coaxial Stretching," Langmuir, vol. 31, no. 37, pp. 10173–10182, Sep. 2015.

J. Zhuang and Y. S. Ju, "A tunable hemispherical platform for non-stretching curved flexible electronics and optoelectronics," J. Appl. Phys., vol. 116, no. 4, p. 044508, Jul. 2014.

J. Zhuang and Y. S. Ju, "Deployable and Conformal Planar Micro-Devices: Design and Model Validation," Micromachines, vol. 5, no. 3, pp. 528–546, Aug. 2014.

Y. Zhan, G. Cha, **J. Zhuang**, Y. Jia, and Y. S. Ju, "Microscale liquid-based mechanical elements for multifunctional integration," J. Compos. Mater., vol. 47, no. 1, pp. 65–75, Jan. 2013.

Conference Proceedings and Presentations

J. Zhuang and Y. S. Ju, "Deployable MEMS Devices for Minimally Invasive Monitoring of Cortical Activities," p. V010T11A007, Nov. 2013.

Chapter 1

Introduction

1.1 Flexible/stretchable and deployable electronics

Most of prevailing forms of electronic/optoelectronic technologies in the world use planar and rigid substrates as basic and functional elements. Such devices require high stability and are fragile to environmental loadings during operation. However, recent design of bio-inspired devices demands high adaptability to curved surfaces and deformations from the human body. Due to the natural rigidity, electronic devices suffer from various loadings such as tension and bending when used in such applications and result in performance degradation or even failure. The so called “flexible electronics” is then developed by researchers as a solution. This strategy avoids the brittle, rigid and planar nature of commercial electronics and enables the flexibility of electronic elements to operate under non-planar surfaces and multiple loadings without compromising performance.

The attempts to design flexible circuits start with paper-like displays and gradually expand to more challenging applications in various areas. Early methods try to achieve bendability of brittle elements and reduce the strain by using ultra-thin films since bending strain is directly proportional to thickness [1]. Another way to further bear strain is to embed functional elements into the mechanical neutral plane of a supporting layer [2]. Later methods to enable stretchability of circuits without performance degradation are to combine strain reducing and

isolation mechanisms with layouts enabling out-of-plane motions of the functional elements [3]–[5]. An example of this design is thin arrays of wavy silicon ribbons made by releasing flat ribbons that bond with pre-strained elastomeric substrate [3]. Due to the deformation of buckling ribbons, such device can stand high levels of strain. Other designs that do not specifically exploit out-of-plane motions use spring structures as interconnects to bear large deformations [6]. The mechanisms and strategies mentioned above can be combined to construct stretchable electronic/optoelectronic integrated systems. Some successful demonstrations have been reported using stretchable metal interconnects and wavy membranes [6], [7] as strain reducer or isolator to enable the operation of electronic/optoelectronic elements under curvilinear applications.

Another variation of electronic devices that also demands high flexibility or stretchability is designed to have the ability to be deployable in the field. Deployable devices that can be introduced into a region of interest in their compact collapsed states and then deployed to cover large volumes or surface areas are of great interest to various engineering and biomedical applications [8]–[12]. Incorporating electronic components on such deployable devices is challenging as the electronic components must be able to undergo large deformations in highly dynamic situations. Deployable electronics are promising in applications such as stents/catheters/opto-electrode arrays for minimally invasive diagnosis and treatments of cardiovascular and neuronal diseases, deployable sensor networks for structural health monitoring or robotics applications and compact launch-volume structures for space applications.

Currently available deployable devices and tools, in particular those employed for minimally invasive bio-medical procedures, are mostly limited to mechanical functionalities. Most of these devices target limited geometries and rely on inflatable balloons for deployment [13], [14]. A

highly desirable design of flexible electronics should be able to adapt planar configurations while at the same time providing the ability to incorporate electrical, optoelectronic and other sensing and actuation capabilities. Such design provides opportunities to further expand the usage of deployable devices and to facilitate the exploration of novel applications.

1.2 Liquid based mechanical interfaces

Despite these methods mentioned in Section 1.1 are able to reduce strain at certain degree, the active elements are not directly isolated from strain. As a result, the device performance can be slightly changed under stretching or bending. This is critical for integrated and sophisticated circuits based on CMOS transistors. We report an alternative approach where we mechanically decouple functional elements from load bearing support structures using capillary-confined liquid bridges. This approach allows the use of standard electronic or optoelectronic devices fabricated on "thick" substrates as opposed to simplified circuits built on highly customized ultra-thin semiconductor membranes.

Figure 1.1 schematically illustrates our concept under two basic types of mechanical deformation. An array of liquid bridges is formed between a flexible bottom substrate and a top rigid plate emulating a functional semiconductor chip. In response to mechanical tension or bending applied to the bottom substrate, the liquid bridges deform or rupture while protecting the brittle top plate.

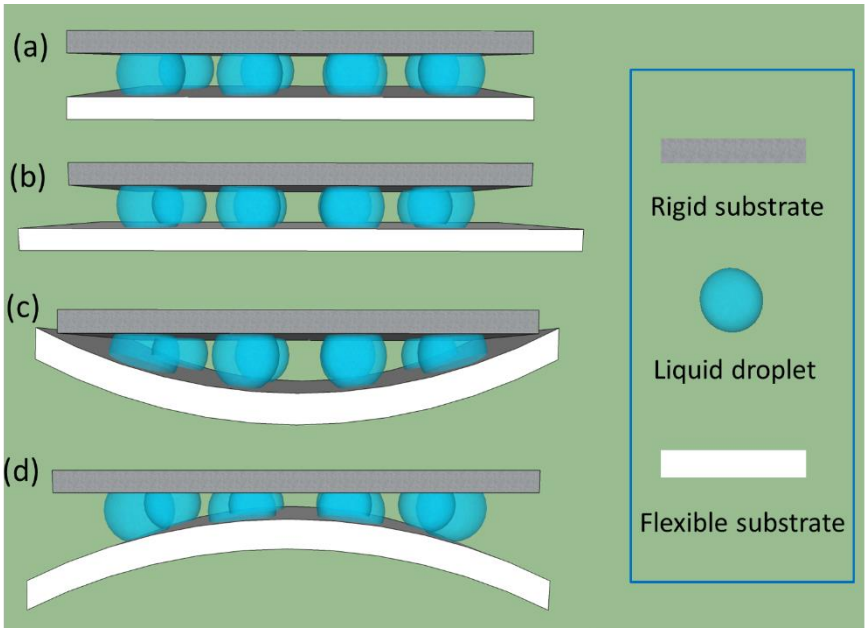

Figure 1.1 Scheme of the mechanical liquid interface under various loadings: (a) unloaded; (b) tensile; (c) upward bending; (d) downward bending.

Microscale liquid bridges offer unique mechanical characteristics. They can undergo significant deformation without transferring large shear stress to solid support structures and can be perfectly healed even after they are completely ruptured. They can also withstand cyclic loads without suffering from any fatigue-induced failure. At microscale, liquid elements made of non-evaporating materials, such as ionic liquids with virtually zero vapor pressure, can be effectively confined without requiring any physical seals due to the predominance of surface tension over gravity or other inertia forces.

As an interface between rigid component and flexible substrate, the liquid interface connects two parts through surface tension forces. The capillary forces exerted on the rigid object is determined by the meniscus shape of the liquid film, which changes with the distance between the two parts. The flexible substrate might undergo significant amount of deformation by

horizontal stretching or vertical bending in different loading situations. Thus it is important to study the interactions between the liquid interface and the rigid component.

1.3 Elasto-capillarity: liquid solid interaction

Although negligible at macroscopic scales, capillary forces become important at sub-millimetric scales. Elastocapillary liquid solid interactions involving elastic deformation of solid objects due to capillary effects of liquid droplets/films are observed in various fields such as biology and microelectromechanical systems (MEMS). It is of great interest to understand the physical mechanisms underlying these phenomena for the design of mechanical interface for non-stretching flexible or deployable electronics.

1.3.1 Elasto-capillary length

The elasto-capillary length is a characteristic length scale to quantify the relative importance of surface tension over elasticity.

For an elastic plate (length L, width w and thickness h) coated with a thin layer of liquid (surface tension γ), when it comes in contact with a rigid cylinder (radius R) coated with the same liquid, the plate wraps around the cylinder by surface tension forces (Figure 1.2) [15]. By considering the surface energy and elastic energy, the elasto-capillary length can be obtained as

$$L_{EC} = \sqrt{\frac{B}{\gamma}} \sim \sqrt{\frac{Eh^3}{\gamma}} \quad (1.1)$$

Where $B = Eh^3 / 12(1 - \nu^2)$ is the bending modulus of the thin plate.

Elasto-capillary length sets a typical length scale that a structure is significantly deformed by surface tension forces if its length is larger than L_{EC}. In the contrary, if its length is much smaller than this length scale, then surface tension has a negligible effect on the structure.

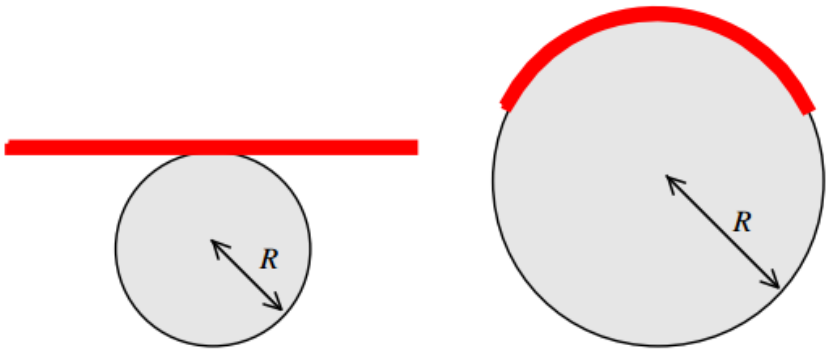

Figure 1.2 An illustration of the elasto-capillary length L_{EC}: a flexible sheet is put in contact with a cylinder of radius R coated with a wetting liquid [15].

1.3.2 Elasto-capillarity for thin films

As the elasto-capillary length scales with the thickness of a plate or a sheet (Equation 1.1), the surface tension tends to have a significant effect on thin slender structures such as plates and sheets. In fact, capillary forces have been used for deforming thin plates or sheets into predictable or controllable manner, including self-folding thin sheets into 3D microstructures [16]–[18]and self-assembly of micro parts. In these applications, a thin sheet self-wraps around a liquid droplet and becomes a predefined structure. Based on different templates and configurations, they can be constructed into various shapes or origamis (Figure 1.3). The self-folding or self-wrapping happens as a result of minimization of the surface of the liquid in contact with air. These techniques provide way to produce 3D microstructures that are difficult with conventional etching and layer deposition techniques from micro-electronic fabrications for mostly planar objects.

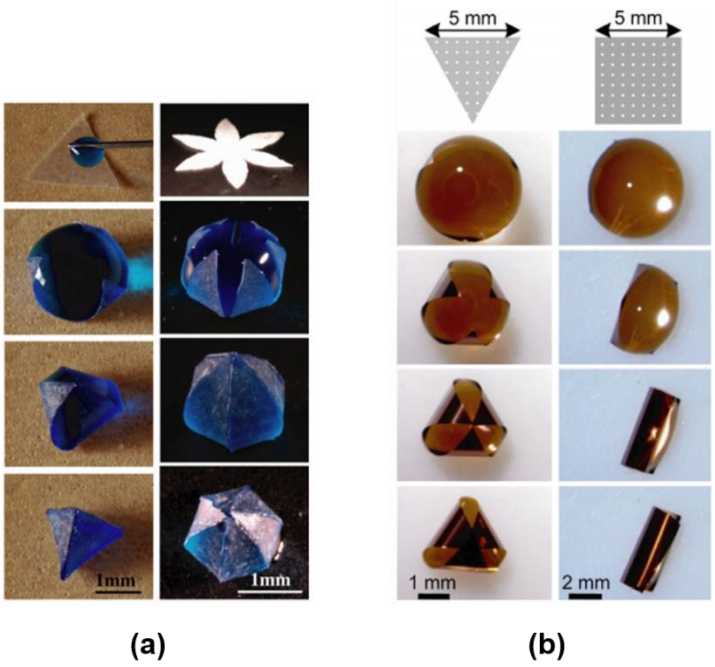

Figure 1.3 Self-wrapping of a flexible sheet (PDMS and silicon) around a droplet of water leading to different 3D structures from [16] and [19] respectively.

1.4 Numerical simulation methods

1.4.1 Surface Evolver

Surface Evolver[20] is widely used for the study of liquid surfaces based on minimization of surface energy. By specifying the initial surface, constraints and an energy function, the evolution of the surface shape are determined so as to minimize the energy (Figure 1.4). The energies in Surface Evolver include surface tension, gravitational energy and user defined integrals. Surface Evolver can handle complicated topology, volume constraints, boundary conditions and other user defined constraints.

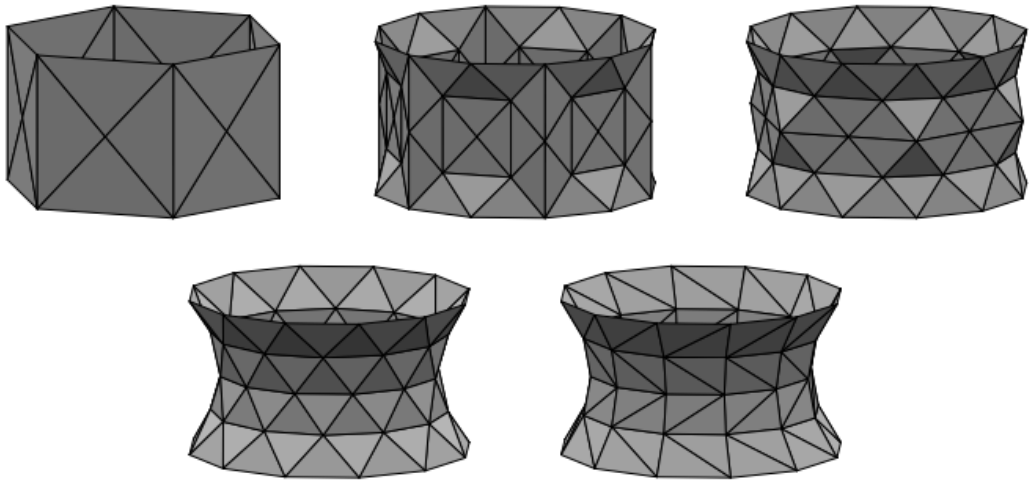

Figure 1.4 Evolution of a liquid bridge in Surface Evolver [20].

Surface Evolver is used for studies of different aspects of static or quasi-static behaviors of a fluid element. Previous studies have reported static simulations of liquid bridges that were formed between two rigid objects such as parallel plates or spheres[21]–[24]. The geometries of the liquid bridge at equilibrium state are obtained using Surface Evolver under various surface conditions. The contact angles determined from the meniscus thus can be used to calculate capillary forces exerted on the rigid objects. Another use case is to study the rupture distance of a liquid bridge, which is the maximum distance between two parallel plates when the liquid fails to maintain a bridge.

Although Surface Evolver is accurate and convenient for surfaces at equilibrium states, it is not able to handle dynamic situations where the liquid is far from equilibrium and the inertial effect is not negligible. To fully capture the dynamics of fluid under high frequency or large displacement, a more comprehensive simulation model is necessary.

1.4.2 Dynamic modeling methods

Computational fluid dynamics (CFD) is an important branch of fluid dynamics, which combines numerical analysis and computational algorithms to solve and analyze fluid flow problems. The Navier-Stokes equation that defines a single-phase fluid flow is the fundamental basis of CFD flow problems. Of all methods for CFD problems, two-phase flow model is a promising solution for such situations. The key factor of two-phase modeling is to accurately track the interface between two fluids. There are various methods for two-phase flow problems to track the two-phase interface such as Volume of Fluid (VOF), Marker particles, Level set/Phase field and Moving mesh methods.

In Volume of Fluid method[25], the phase interface is represented by volume fraction ψ in each cell of the fixed mesh grid. Volume fraction ranges from 0 to 1 with 0 represents completely fills with fluid 1 and 1 represents completely fills with fluid 2. The evolution of volume fraction is governed by the transport equation

$$\frac{\partial \varphi}{\partial \mathrm{t}} + u \cdot \nabla \varphi = 0 \quad (1.2)$$

The interface geometry is reconstructed by the populated volume fraction in each cell and geometric flux calculation is performed. The normal direction to the interface is calculated and the normal plane at each cell is determined assuming the interface in each cell is planar.

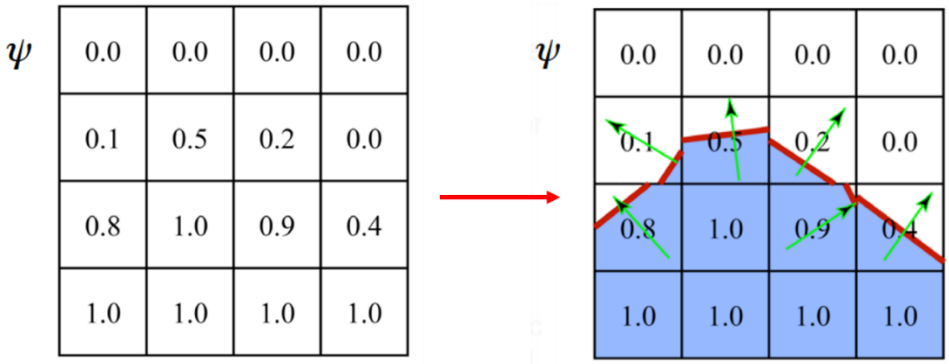

Figure 1.5 The reconstruction of interface in Volume of Fluid method.

In practical applications [26], [27], VOF methods can achieve good volume conservation and be able to track the interface during the evolution. However, the reconstruction of the interface geometry is still challenging and the normal interface movement is not straightforward.

Level set method and phase field method are another methods to solve two-phase flow problem. In level set method [28], the phase interface is represented by the level set function φ with φ = 0 for fluid 1 and φ = 1 for fluid 2. The interface is the contour where φ = 0.5. The motion of the interface is tracked by the transport equation

$$\frac{\partial \varphi}{\partial t} + u \cdot \nabla \varphi = \gamma \nabla \cdot (\varepsilon \nabla \varphi - \varphi(1-\varphi)\frac{\nabla \varphi}{|\nabla \varphi|}) \quad (1.3)$$

The parameter ε determines the thickness of the interface where φ varies smoothly from 0 to 1. The parameter ε is typically of the same order as the size of the elements of the mesh grid. The parameter γ determines the amount of stabilization of the level set function. By solving the transport equation, the phase interface can be tracked. Level set method allows a simple interface geometry reconstruction and automatically handles the normal interface movement. However,

the volume conservation is inherently not supported and might significantly affect the accuracy of results.

The phase field method[29] offers an attractive alternative to solve multiphase flow problems. In phase field method, the phase interface is tracked by phase field variable instead of directly tracking the interface between two fluids. By default, the surface tension force is inherently coupled with the Navier-Stokes equations as a body force. The evolution of the phase field variable is governed by the Cahn-Hilliard equation

$$\frac{\partial \varphi}{\partial \mathrm{t}} + u \cdot \nabla \varphi = \gamma \nabla \cdot \nabla G \quad (1.4)$$

where G is the chemical potential and γ is the mobility. Different from the level set method where the fluid interface is simply advected with the flow field, the Cahn-Hilliard equation does not only convect the fluid interface but also ensure the total energy of the system diminishes correctly. Both level set and phase field handles topology changes inherently. However, both suffer from volume conservation issues. In addition, due to the finite thickness of the interface, typically very fine mesh is necessary to achieve accurate results, which means more computation and time cost.

Different from the methods discussed above, in moving mesh method, the phase interface is represented by mesh nodes on the interface. The movement of the interface is directly coupled to the movement of the mesh grid, which is tracked by Arbitrary Lagrangian-Eulerian (ALE) moving mesh method[30]–[32]. The deformation of the interface is directly reflected on the mesh grid, which might result in large mesh deformations and thus periodically remeshing is necessary for convergence and accurate results. Moving mesh method is very accurate for small deformation on the interface, but it typically fails to capture topology changes and normal

movement of the interface. It is more complex to implement and required more computational and time cost.

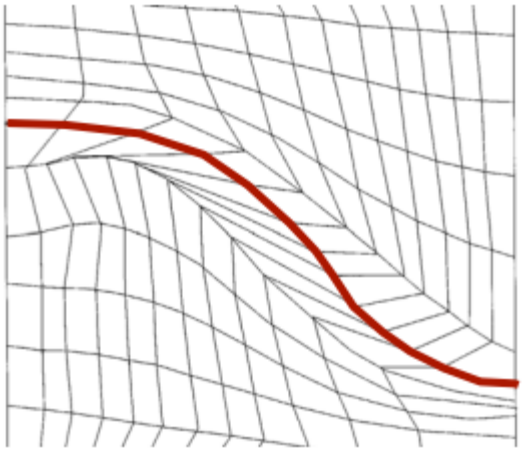

Figure 1.6 The representation of the interface in moving mesh method [31].

1.5 Scope of research

The present work studies mechanical liquid interfaces for flexible, stretchable and/or deployable electronics.

Chapter 2 presents a mechanical liquid interface with capillary confined microscale liquid bridges. A combined modeling and experimental study is performed to investigate the mechanical characteristics of such integrated structures under quasi-static conditions and demonstrate their feasibility. This work establishes an early feasibility of flexible electronics based on liquid-based mechanical interfaces and a design tool to enable their systematic mechanical design and optimization.

Chapter 3 explores the characteristics of a micro scale liquid bridge of the mechanical interface under various dynamic conditions. The deformation and rupture of axisymmetric liquid

bridges being stretched between two fully wetted coaxial disks are studied experimentally and theoretically. The effects of the stretching velocity, liquid properties, and liquid volume on the dynamics of liquid bridges are systematically investigated to provide direct experimental validation of our numerical model for stretching velocities as high as 3 m/s.

Chapter 4 discusses a numerical model coupling solid mechanics and fluid dynamics to fully simulate the dynamic process of capillary self-alignment. This model solves the time-dependent Navier−Stokes equations while tracking the deformation of the liquid−air interface using the arbitrary Lagrangian−Eulerian (ALE) moving mesh method to fully account for fluid dynamics in the supporting liquid film. This work provides an experimentally validated modeling approach and physical insights to help establish foundation for systematic further studies and related applications of capillary self-alignment.

Chapter 5 introduces a design concept for a deployable planar microdevice and the modeling and experimental validation of its mechanical behaviors based on elasto-capillary interaction. Such a deployable device can be introduced into a region of interest in its compact "collapsed" state and then deployed to conformally cover a large two-dimensional surface area for minimally invasive biomedical operations and other engineering applications. This study establishes an early foundation for the mechanical design of this and related deployable planar microdevice concepts.

Chapter 6 explores a tunable platform for incorporating flexible and yet *non-stretching* device layers on a hemisphere for possible application of incorporating electronics or optoelectronics on curved surfaces. A mechanical model is developed to elucidate the dependence of the conformality of the petal structures on their elastic modulus and thickness and

the liquid surface tension. This platform will enable facile integration of *non-stretching* electronic and optoelectronic components prepared using established planar fabrication techniques on tunable hemispherical surfaces.

Chapter 2

Microscale Liquid-based Mechanical Interfaces for Flexible and Stretchable Electronics

Most existing approaches to flexible and stretchable electronics are based on directly bonding semiconductor devices onto stretchable substrates. They require fragile 3D interconnects, stretchable conducting polymeric materials, or liquid metals to accommodate mechanical deformation while often providing limited optoelectronic functionality and mechanical robustness. We report an alternative strategy for realizing flexible electronics where we integrate brittle semiconductor chips onto flexible substrates using capillary confined microscale liquid bridges as mechanical interfaces. We performed a combined modeling and experimental study to investigate the mechanical characteristics of such integrated structures and demonstrate their feasibility. The experimentally determined topology and rupture characteristics of microscale liquid bridges formed between a brittle glass substrate and a stretchable polymer substrate agree well with the prediction from a quasi-static model based on the surface energy minimization algorithm. The present work establishes an early feasibility of flexible electronics based on liquid-based mechanical interfaces and a design tool to enable their systematic mechanical design and optimization.

2.1 Background

The majority of existing electronics and optoelectronics are based on functional elements built on rigid planar semiconductor substrates. The emergence of so-called flexible and stretchable electronics for biomedical, energy, and other applications, however, necessitates adaptation of such functional elements and related interfaces to accommodate stretching, bending, and other types of mechanical deformation [33].

Previous studies reported various strategies to realize flexible and stretchable electronics. These include, for example, the use of ultra-thin semiconductor membranes, flexing 3D metal or liquid-metal interconnects, and stretchable organic conductors and semiconductors [1]–[4], [6], [7], [34].

We report an alternative approach where we mechanically integrate functional elements onto supporting substrates using capillary-confined microscale liquid bridges. This approach allows the use of standard electronic or optoelectronic devices fabricated on "thick" substrates as opposed to simplified circuits built on highly customized ultra-thin semiconductor membranes.

Microscale liquid bridges offer unique mechanical characteristics. They can undergo significant deformation without transferring large stress to brittle functional elements and can be perfectly healed even after they are completely ruptured. They can also withstand cyclic loads without suffering from fatigue-induced failure. At microscale, liquid elements made of non-evaporating materials, such as ionic liquids with virtually zero vapor pressure, can be effectively confined without requiring any physical seals due to the predominance of surface tension over gravity and inertia forces.

Figure 2.1 schematically illustrates our concept under two basic types of mechanical deformation. An array of liquid bridges is formed between a flexible bottom substrate and a top rigid plate emulating a functional semiconductor chip. In response to mechanical tension or bending applied to the bottom substrate, the liquid bridges deform or rupture while protecting the brittle top plate.

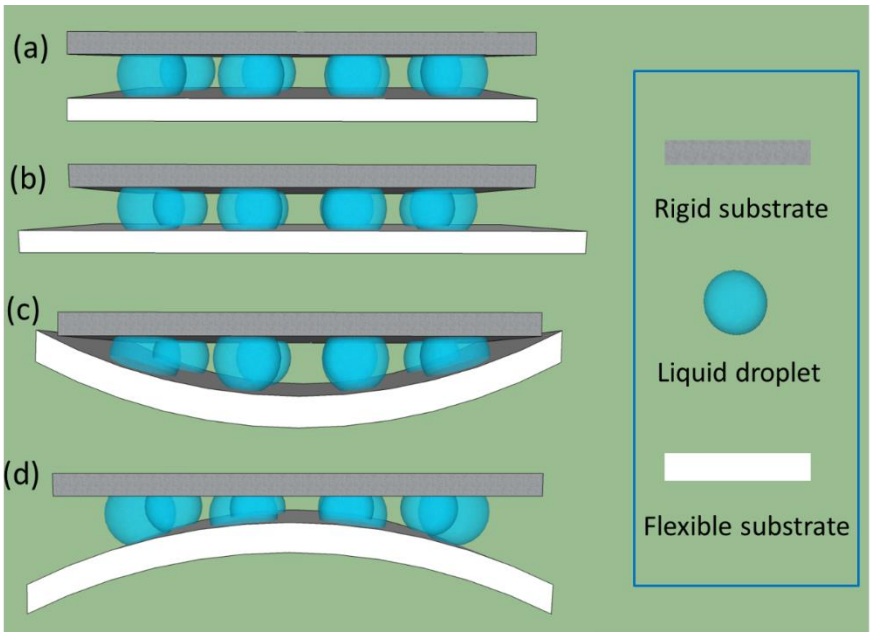

Figure 2.1: Scheme of the mechanical liquid interface under various loadings: (a) unloaded; (b) tensile; (c) upward bending; (d) downward bending.

To demonstrate the feasibility of and help establish technical foundation of this approach, we first develop numerical models based on the surface energy minimization algorithm to predict the topology of liquid bridges under different mechanical loading conditions. A set of

companion experiments is then conducted to validate the model predictions and directly demonstrate the feasibility of liquid-based flexible interfaces.

2.2 Experimental

We use a glass slide to emulate as a rigid inorganic semiconductor chip and a cast PDMS (polydimethylsiloxane) plate as a flexible and stretchable substrate. The surfaces of both glass and PDMS substrates are coated with hydrophobic layers, which are patterned to create arrays of circular islands of radius 500 μm. The circular islands on the PDMS substrate, which are initially hydrophobic, are treated with oxygen plasma to render them hydrophilic. Liquid droplets are manually dispensed on the rigid substrate, which is then aligned and brought near the flexible substrate to form liquid bridges. To minimize evaporation during our experiments, a mixture of glycerin and water (4:5) is used to create liquid bridges.

The integrated assembly is placed on rigid cylinders of different radii to subject it to various levels of bending. Optical images of the liquid bridges are captured using a video microscopy system. Figure 2.2 shows representative optical images of the liquid bridges under positive or negative bending as characterized by the radius of curvature.

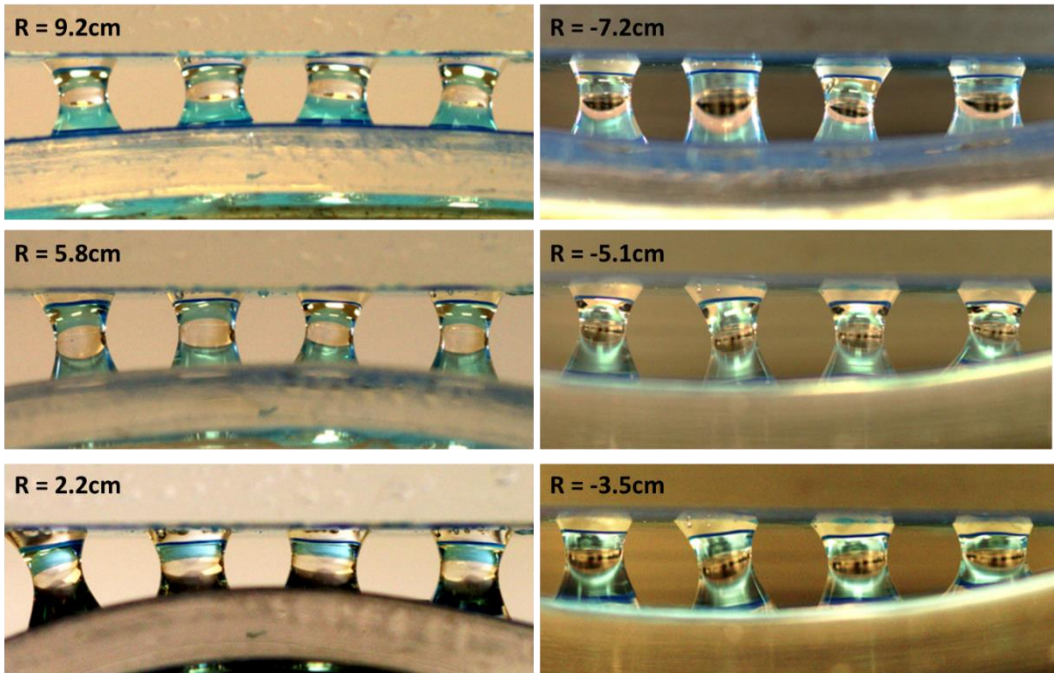

Figure 2.2: Liquid bridges under positive or negative bending of increasing magnitudes. *R* is the bending radius of flexible substrate.

2.3 Modeling

Previous studies reported analytical and numerical methods to modeling capillary phenomena involving liquid bridges that were formed between two rigid objects [21]–[24]. We consider an array of liquid bridges formed between a deformable bottom substrate and a rigid top substrate. The substrate surfaces are hydrophobic except within circular hydrophilic islands of radius r_s. For a given intrinsic surface contact angle $\theta_{intrinsic}$ of the hydrophilic regions and liquid volume V_0, the shape of the liquid bridges is predicted using the surface energy minimization algorithm. Capillary forces are calculated using both the virtual work model and the integration of the surface tension and the Laplace pressure forces. We verify that the two approaches yield

the same numerical results to within 5%. To facilitate generalization of our results, we define the normalized gap $g_n = g/r_s$, the normalized force $F_n = F/ 2\pi\gamma r_s$, and the normalized volume $V_n = V/r^3$, where γ is the surface tension coefficient.

Under uniform tension, the hydrophilic patterns on the bottom substrate translate laterally and deform from circles of radius R to ellipses of major axis b and minor axis a as illustrated in Fig. 2.3a. Here, $a = 2\, r_s\, (1 - \nu\varepsilon)$, $b = 2\, r_s\, (1 + \varepsilon)$, and $ds = \varepsilon\, dp$. The Poisson ratio is denoted as ν, and the applied strain as ε.

Under pure bending, we consider a liquid bridge that is located a distance l from the symmetric plane (Fig. 2.3b). As the radius of curvature R of the bottom substrate is larger than the hydrophilic pattern radius r_s, we approximate that the hydrophilic pattern on the bottom substrate remains flat. The angle between the pattern and the original substrate plane is denoted as $\beta = \arctan(L/R)$.

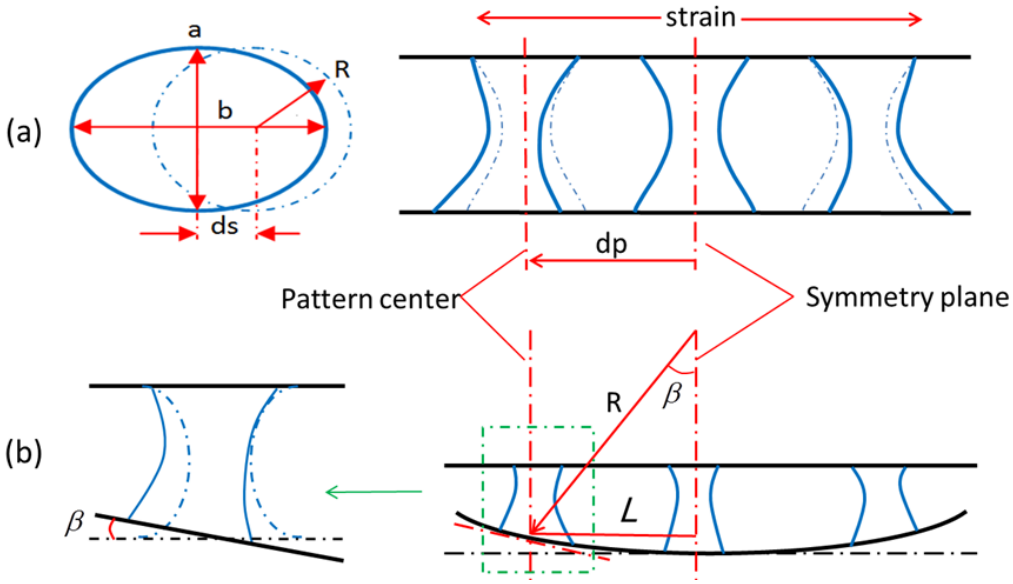

Figure 2.3: Geometric models used to represent a liquid bridge as the bottom substrate is subjected to tensile (a) or bending (b) loading.

2.4 Results and Discussion

Figure 2.4 shows the predicted shapes of liquid bridges and the corresponding optical images under different bending conditions. The apparent contact angles of the liquid bridge on the bottom substrates change their magnitudes substantially and become asymmetric to accommodate the substrate bending. In contrast, the apparent contact angles on the top substrate are relatively unchanged as the top substrate remains undeformed. The predicted liquid bridge shapes agree well with the experimental results.

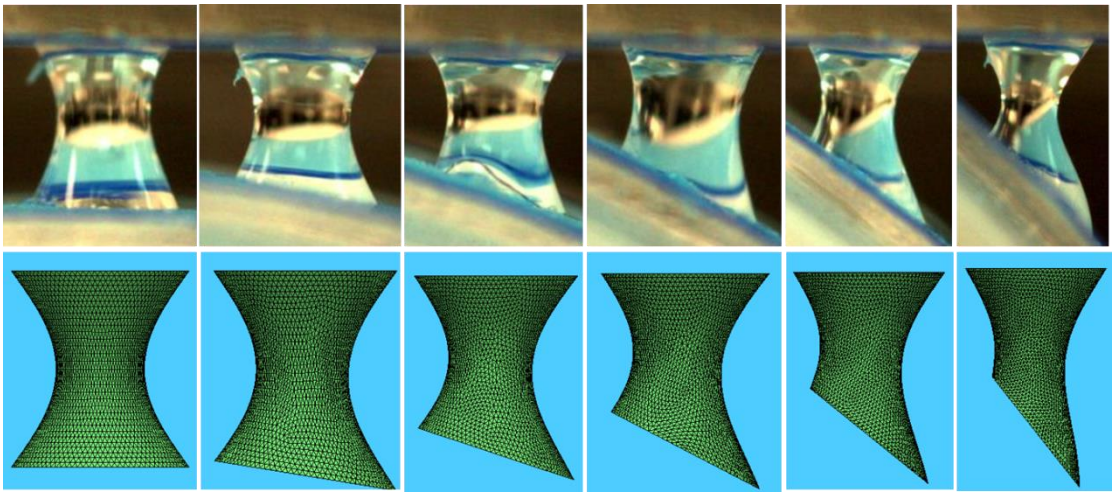

Figure 2.4: The shapes of a liquid bridge under different bending conditions. (top) experimentally obtained optical images; (bottom) model prediction.

2.4.1 Capillary Forces

To help systematically design liquid interfaces, we next examine the dependence of the capillary force on the liquid volume and the gap between the substrates.

For a given liquid volume, the shapes of liquid bridges at different gaps are predicted. Different components of the capillary force of liquid bridge are calculated for both tensile and bending situations. The apparent contact angles at the top left edge θ_1 and at the top right edge θ_2 are defined as shown in Fig. 2.5. R_1 and R_2 are the two principal curvature radii of the liquid bridge.

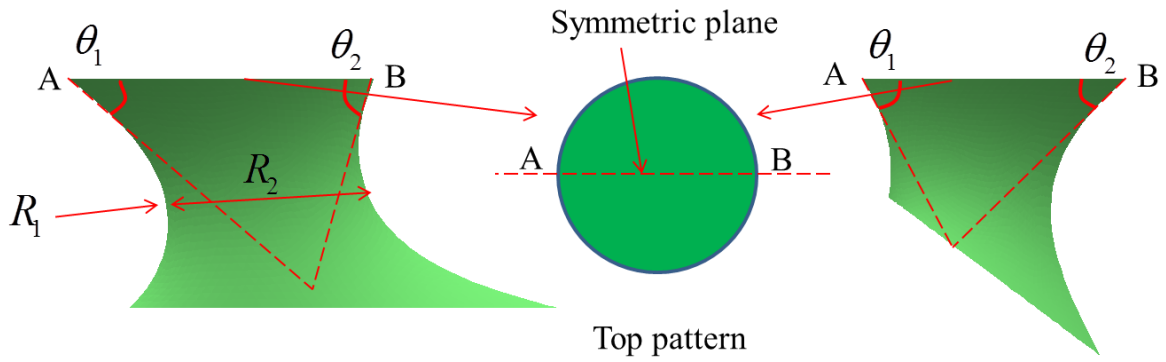

Figure 2.5: Definition of the top left and right apparent contact angles and the two principal radii of curvature.

The vertical force F_v is the sum of vertical surface tension force S_v and Laplace pressure force F_P. The S_v is obtained by integrating the vertical component of surface tension along the wetting perimeter, namely $S_v = \oint \gamma \sin\theta dl$, where θ is the contact angle. Due to the symmetry of liquid shape, $S_v = \oint \gamma \sin\theta dl = 2\int_A^B \gamma \sin\theta dl$ ($\theta_1 < \theta < \theta_2$). The contact angles between A

and B are continuous and the integral can be evaluated by studying the two contact angles θ_1 and θ_2 at the edge.

Under tensile loading (Fig. 2.6(a), (c)), at a small gap ($g_n = 0.6$) the liquid is highly compressed resulting in large θ_1 and θ_2 ($90° < \theta_1 < \theta_2$). As the two substrates are gradually pulled apart, the two contact angles decreases. At first both θ_1 and θ_2 is larger than 90°, S_v increases with gap. After θ_1 is below 90° while θ_2 is larger than 90°, S_v continues increasing while with a smaller slope. At certain point, S_v reaches the maximum and decreases when both θ_1 and θ_2 is smaller than 90°.

The Laplace pressure force is obtained as $F_P = -\gamma(\frac{1}{R_1} + \frac{1}{R_2})A_W$, where A_W is the wetting area (constant). At small gap, the pressure is very high due to small positive curvature radii R_1 and R_2. As the gap increases, R_1 starts to decrease and become negative whereas R_2 increases slightly. Consequently, the repulsive pressure force F_p decreases in magnitude. At large gap, the change of R_2 dominates the change of F_p, which therefore increases with gap. The vertical force F_v as a function of gap can be obtained by the sum of S_v and F_p.

The shear force F_s is obtained by integrating the horizontal component of surface tension force along the wetting perimeter on the top substrate, namely $F_s = \oint \gamma(\cos\theta)\, \vec{n} \cdot \overrightarrow{dl}$, where $\vec{n}$ is the vector of horizontal direction. Due to the symmetry of liquid shape, $F_s = \oint \gamma(\cos\theta)\, \vec{n} \cdot \overrightarrow{dl} = 2\int_A^B \gamma(\cos\theta)\, \vec{n} \cdot \overrightarrow{dl}$ ($\theta_1 < \theta < \theta_2$).

As the gap increases, the two contact angles decreases. When θ_1 is below 90° while θ_2 is larger than 90°, F_s increases with gap. After θ_2 is reduced below 90° and gets closer to θ_1,

shear force reaches a maximum and then gradually decreases, eventually reaching zero when the liquid ruptures.

The vertical force F_v of the bending situation (Fig. 2.6(b);(d)) can be explained similarly with the tensile situation. As for shear force F_s, it decreases monotonously to zero. At small gap, θ_1 is below 90° while θ_2 is above 90°. The large difference of the two contact angles results in a large F_s. When the two substrates are pulled apart, the difference between θ_1 and θ_2 becomes less and less. As a result, F_s decreases and reaches zero at certain gap.

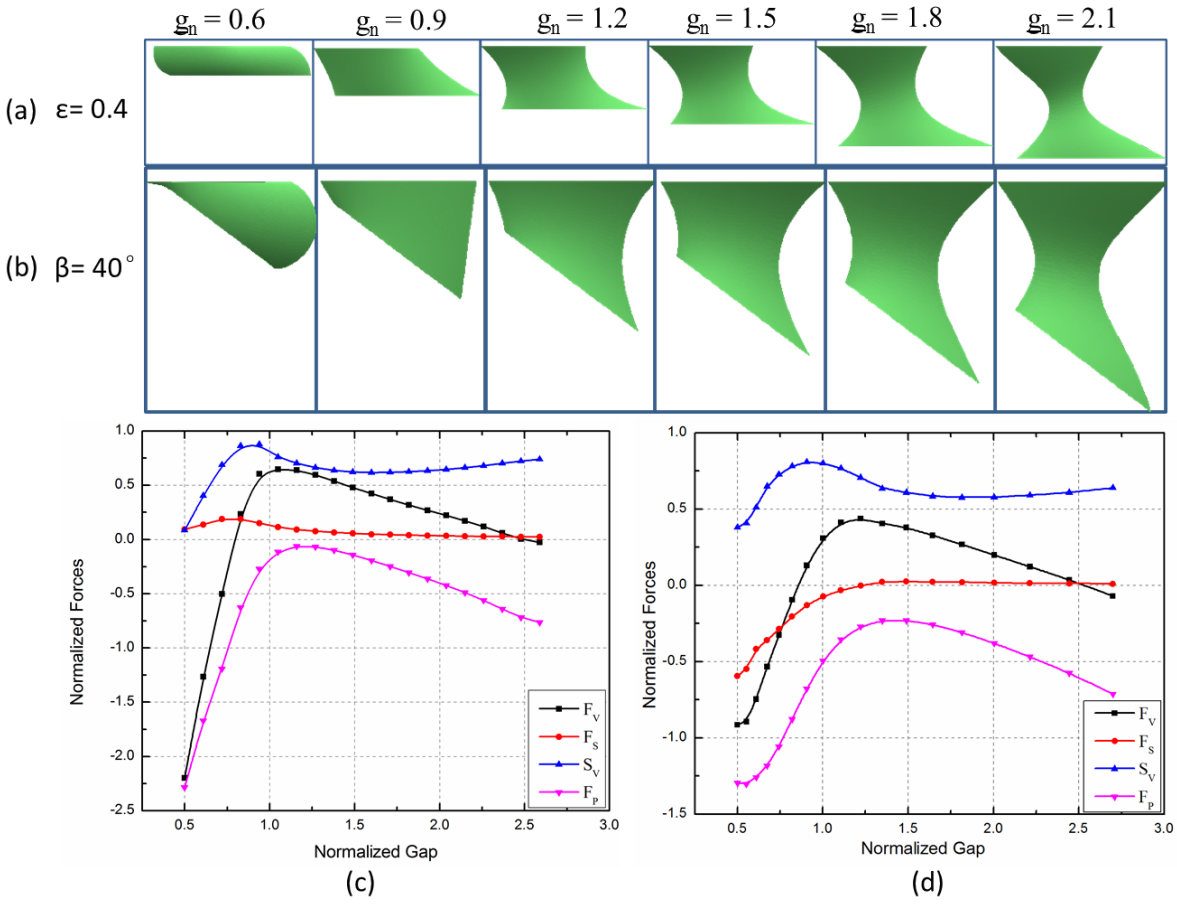

Figure 2.6: Liquid shapes and capillary forces with different gaps under certain loading level (V_n = 2.8). Liquid shapes evolvement under tensile strain =0.4 (a) and bending angle = 40° (b); Capillary forces: tensile loading (c); bending loading (d).

For a given normalized gap, the shapes of liquid bridges at different volumes are predicted (Fig. 2.7). The dependence of S_v on the liquid volume is similar for both tensile and bending situations. As the liquid volume increases, both θ_1 and θ_2 increase. When the two contact angles are less than 90°, S_v increases with the liquid volume. When θ_2 is larger than 90°, The S_v reaches a maximum value and then decreases with further increase in the liquid volume.

Under tensile loading, the change in R_2 dominates the change of pressure force F_p at small liquid volume resulting in increasing F_p. As the liquid volume further increases, R_1 becomes positive, dominating the change of F_p. Consequently, F_p decreases with liquid volume. Under bending loading, the pressure force F_p is positive at small liquid volume and decreases monotonously with the liquid volume. The vertical force F_v can then be obtained and explained as a sum of S_v and F_p.

The shear force F_s under tension first increases with liquid volume due to the enlarging difference between θ_1 and θ_2. The difference of two contact angles decreases when the liquid volume is further increased, resulting in decreasing shear force F_s. Under bending loading, the shear force F_s decreases below zero after a slight increase at first.

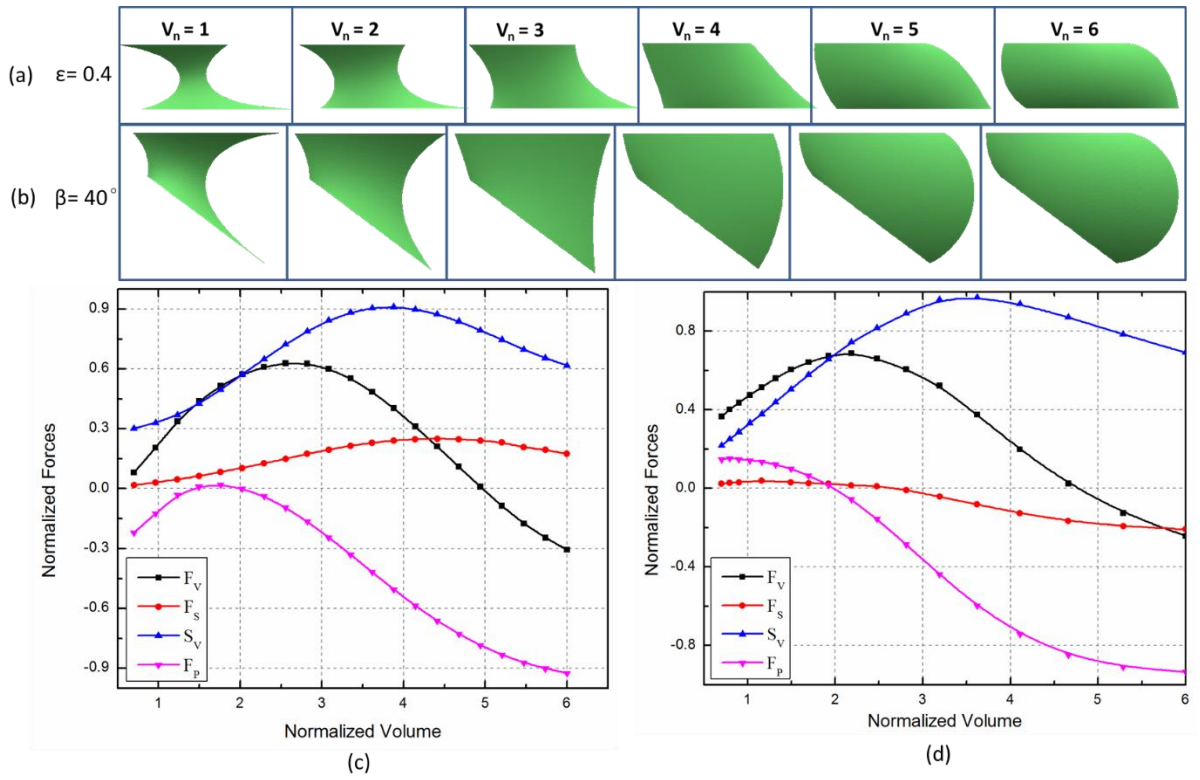

Figure 2.7: Liquid shapes and capillary forces with different volumes under certain loading level (g_n=1.2). Liquid shapes evolvement under tensile strain=0.4 (a) and bending angle=40° (b). Capillary forces: tensile loading (c); bending loading (d).

2.4.2 Loading effect

The relation between loading levels and forces are also studied. There are two regimes considering the states of liquid bridges: the repulsive regime when the liquid is compressed and the vertical force is repulsive and the attractive regime the liquid is stretched and the vertical force is attractive.

Figure. 2.8 shows the capillary forces under different strain levels ranging from 0 to 1. In the repulsive regime ((a);(c)), the gap is small and the volume is large enough for the liquid to wet the hydrophobic area beyond the patterns, therefore the two contact angles θ_1 and θ_2 are larger than 90° at zero strain. When the substrate is stretched, θ_1 decreases and θ_2 increases as the applied strain. The vertical surface tension force S_v thus has a slight increase at first and then remain almost constant. Meanwhile, the two principal curvature radii R_1 and R_2 increases as the strain. As a result, the pressure force F_p decreases and then slight increases in magnitude. As a sum of S_v and F_p, the repulsive vertical force F_v decreases significantly at small strains and remain almost constant at large strains. The shear force F_s, as indicated in the Fig.8(c), increases with the applied strain and remain constant at large strains.

In the attractive regime, as the strain increases, θ_1 decreases while θ_2 increases to above 90°. The S_v has a slight change while the negative pressure force increases significantly in magnitude, resulting in decreasing vertical force F_v. Meanwhile, the shear force F_s increases monotonously with the strain.

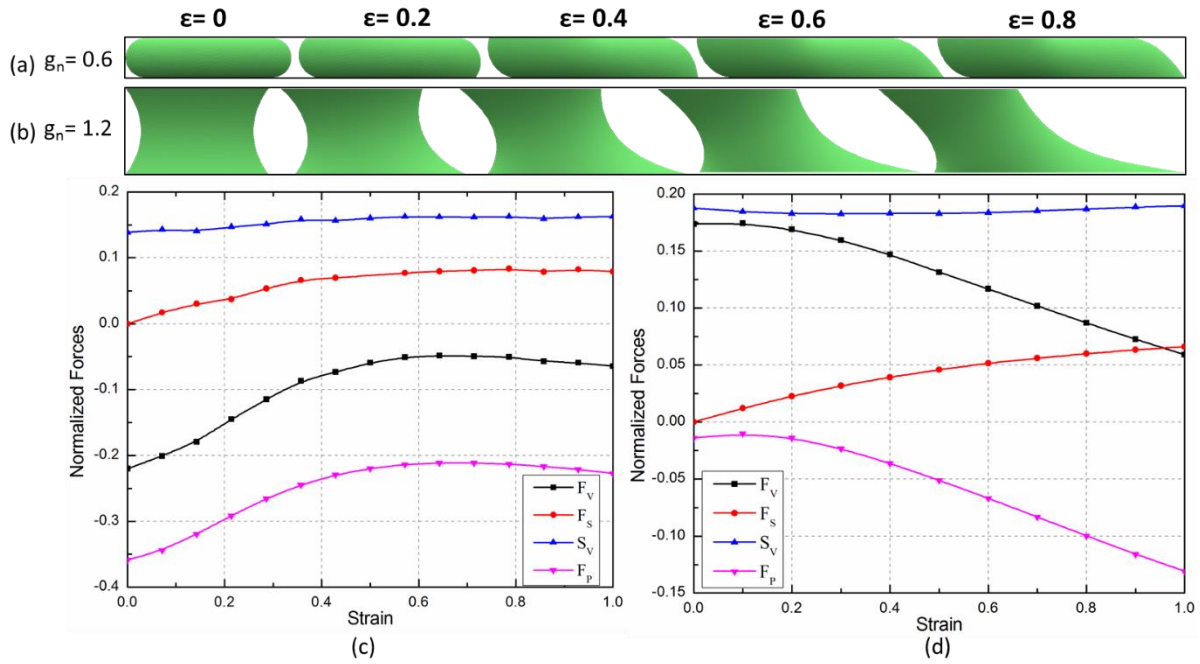

Figure 2.8: Liquid shapes and capillary forces under different strain levels (V_n = 2.8). Liquid shapes evolvement in the repulsive (a) and attractive (b) regimes. Capillary forces in the repulsive (c) and attractive (d) regimes.

Figure 2.9 shows the capillary forces under different bending angles ranging from 0° to 70°. When the substrate is bent, the liquid wets beyond the pattern area and therefore the two contact angles θ_1 and θ_2 are larger than 90° at zero bending. In the repulsive regime, as the bending angle increases, θ_1 decreases below 90° while θ_2 remains constant. As a result, the S_v increases with bending angle and then has a slight decrease. Meanwhile, the F_p decreases with bending angle in magnitude. The repulsive vertical force F_v in magnitude thus decreases at small bending angles and remain almost constant at high bending angles. The shear force F_s, in contrast, increases monotonously with bending angles.

In the attractive regime, the vertical force F_v has the same tendency as the repulsive regime. The shear force F_s first slightly increases and then decreases with bending angle. At certain point, the F_s changes direction and increases in magnitude.

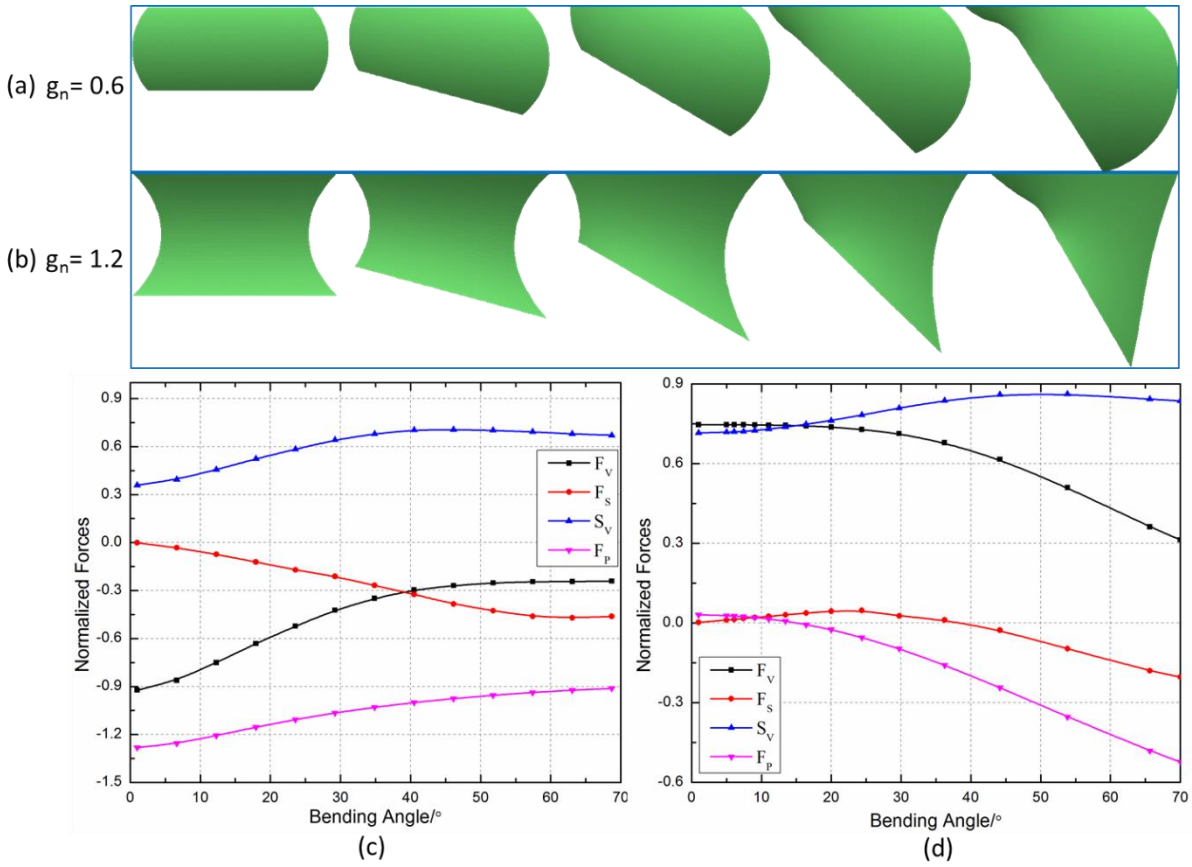

Figure 2.9: Liquid shapes and capillary forces under different bending levels (V_n = 2.8). Liquid shapes evolvement in the repulsive (a) and attractive (b) regimes. Capillary forces in the repulsive (c) and attractive (d) regimes.

Generally, the applied loadings weakens the vertical force and the higher loading level is, the lower the force is. Shear force, however, increases with applied loading levels except for the slight fluctuation at bending attractive regime.

2.4.3 Rupture distance

At sufficiently high level of bending, some of the liquid bridges will eventually rupture. Such rupture may be deliberately designed to occur at each location to protect the brittle top substrate. Previous studies reported detailed modeling results of rupture distances for liquid bridges formed between two parallel rigid substrates under axial loading. The model we developed to predict liquid shapes and forces is also used to obtain the rupture behaviors of the liquid of flexible substrates under tensile and bending loadings. We predict the rupture distance by searching the gap where the minimum diameter of the liquid bridge reaches or highly close to zero. The gap slightly increases by a constant value Δg each step and the minimum diameter of liquid bridge is obtained. The liquid is considered rupturing when the minimum diameter is less than the pre-set value d_c. The searching procedure continues until the desired gap distance is found.

The measured and modeled rupture distances of the new liquid as a function of the bending angle are shown in Fig. 2.10. A liquid droplet with a normalized volume of 2.12 first forms liquid bridge between two substrates. The flexible substrate is bent by attching it to cylinders with different radii. The top substrate are then pulled apart gradually until the liquid bridge ruptures. The rupture distance is obtained by the captured image at rupture.. From the results, a larger bending angle leads to a larger rupture distance. The reason is thatwhen the flexible

substrate is bent, the liquid shape becomes asymmetric. A larger bending angle will increase the asymmetry of the liquid bridge and thus the ability to withstand rupture.

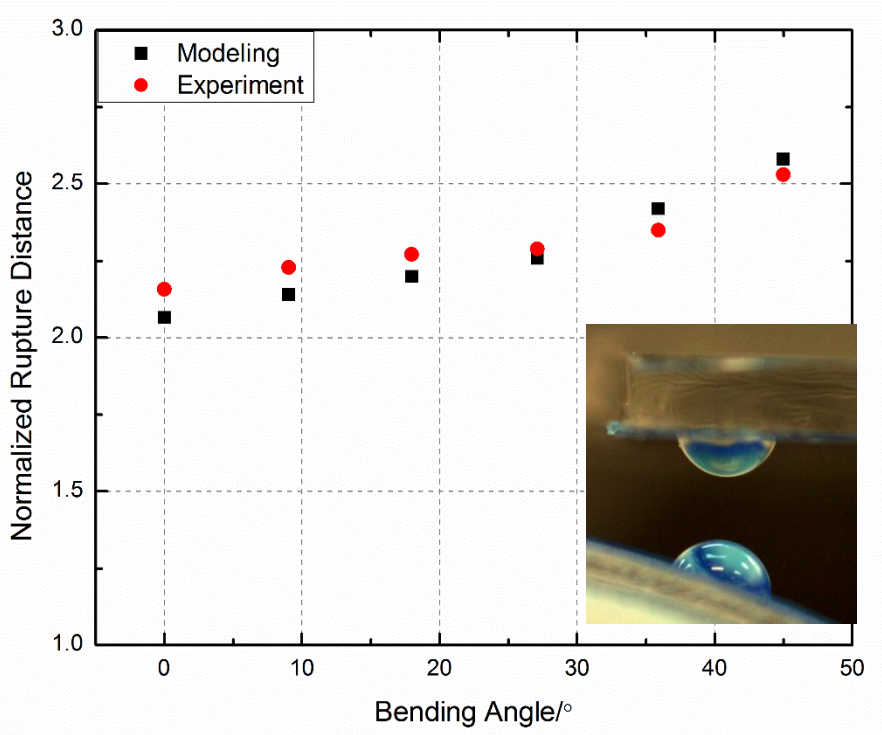

Figure 2.10: Modeling and experimental results of rupture distance as a function of the bending angle (V_n = 2.12).

2.5 Summary

In this chapter, a new approach based on mechanical liquid interface for flexible electronics is proposed and its feasibility is demonstrated. The implement of "perfectly" flexible liquid droplets decouples the load bearing structures from brittle electronic elements, enabling the direct use of commercial circuits. Numerical modeling methods are developed and are proved to

precisely predict the liquid topologies, capillary forces and stress/strain distributions under various loading levels. The modeling and experimental results show the high loadbearing ability and flexibility of the mechanical liquid interface. Our work has established the engineering and scientific foundation for fabrication and optimization of such liquid interfaces for flexible electronics in future research.

Chapter 3

A Combined Experimental and Numerical Modeling Study of the Deformation and Rupture of Axisymmetric Liquid Bridges under Coaxial Stretching

The dynamics of liquid bridges has been attracting a lot of attention and research efforts. In this chapter, the deformation and rupture of axisymmetric liquid bridges being stretched between two fully wetted coaxial disks are studied experimentally and theoretically. We numerically solve the time-dependent Navier-Stokes equations while tracking the deformation of the liquid-air interface using the Arbitrary Lagrangian-Eulerian (ALE) moving mesh method to fully account for the effects of inertia and viscous forces on bridge dynamics. The effects of the stretching velocity, liquid properties, and liquid volume on the dynamics of liquid bridges are systematically investigated to provide direct experimental validation of our numerical model for stretching velocities as high as 3 m/s. The Ohnesorge number (*Oh*) of liquid bridges is a primary factor governing the dynamics of liquid bridge rupture, especially the dependence of the rupture distance on the stretching velocity. The rupture distance generally increases with the stretching velocity, far in excess of the static stability limit. For bridges with low Ohnesorge numbers, however, the rupture distance stay nearly constant or decreases with the stretching velocity within certain velocity windows due to the relative rupture position switching and the thread shape change. Our work provides an experimentally validated modeling approach and

experimental data to help establish foundation for systematic further studies and applications of liquid bridges.

3.1 Background

The statics and dynamics of liquid bridges have been extensively studied for their importance in such diverse areas as crystal growth [35], spraying and atomization of liquids [36], fiber spinning [37], measurements of surface tension and viscosity [38], agglomeration of particles [39], and drop formation through capillary breakup [40]. Recent studies also investigated capillary forces mediated by liquid bridges for enhanced wet adhesion [41]–[46] and for self-alignment and self-assembly of milli- and sub-milliscale objects [47].

Many past studies of liquid bridges focused on their stability under near equilibrium or quasi-static conditions. Gillette et al. [48], for example, determined the limiting gap for the formation of a stable liquid bridge between two circular disks as a function of the liquid volume. A one-dimensional model was also developed by Rivas et al. [49] to characterize the evolution of liquid bridges around their stability limits.

Other studies examined the post-rupture behavior of liquid bridges, such as satellite droplet formation[50] and volume partitioning [51]–[53]. These phenomena are particularly relevant for printing industry. Chadov and Yakhnin [51], [52], for example, investigated liquid bridge partitioning, illustrating preferential transfer of liquid to a more wettable surface. The amount of transferred liquid was also shown to increase with the difference in contact angle between the two surfaces. The separation speed and liquid properties, most notably viscosity and surface tension, also affected the volume partitioning.

The majority of these past studies of liquid bridges relied on quasi-static approximations to model their profiles, capillary forces, and rupture dynamics. This presents fundamental limitations, however, in modeling highly dynamic phenomena where the inertia and viscous effects cannot be ignored.

As an example, microscale liquid bridges have recently been explored as a potential enabler of reversibly switchable optical [54], mechanical, electrical and thermal interfaces [55]–[58] for micro and mesoscale devices. In these applications, liquid bridges can be subjected to repeated ruptures and reformations at rates in excess of 100 Hz. Fast rupture dynamics of liquid bridges also serves as a useful analogy for drop generation from a capillary tube. As another example, in capillary-mediated self-assembly processes, liquid bridge profiles were observed to continuously change and deviate noticeably from their equilibrium states.

This motivated studies of the dynamics of liquid bridges that accounted for the inertia and/or viscous effects. Early such studies, however, were limited as they used one-dimensional or inviscid flow approximations. Meseguer [35] studied axisymmetric liquid bridges that were close to their stability limits using an inviscid slice model. The axisymmetric and non-axisymmetric oscillations of liquid bridges were theoretically investigated by Sanz et al [59], [60]. Later studies investigated the effects of finite viscosity on the dynamics of liquid bridges under different conditions, including forced oscillations [61],[62] and stretching [40],[63]. The latter studies showed that even at modest elongation rates of 0.1 s^{-1}, instantaneous bridge shapes deviate considerably from equilibrium profiles and the limiting length can significantly exceed the critical length of a static bridge at its limit of stability.

Zhang et al. [40] used an one-dimensional (1D) model based on the slender jet assumption[64] to study the deformation and breakup of axisymmetric liquid bridges. The liquid bridges were held between two parallel coaxial disks of the same radius and subjected to stretching as the disks were continually pulled apart. The predicted interface profiles and rupture lengths agreed well with experimental data when stretching velocities were below U_c, which is the capillary velocity scale $(\sigma/\rho/R)^{1/2}$ (= 0.2 m/s for a water bridge of 1.6 mm radius). Here ρ and σ are the density and surface tension of the liquid, respectively and R is the radius of the disks. The capillary velocity scale measures the relative importance of inertial forces to surface tension forces.

A follow-up 2D modeling study [65] extended model predictions to higher stretching velocities and showed that the 1D model gave qualitatively and quantitatively different results from those of a presumably more accurate 2D model at stretching velocities > U_c. Direct experimental validation of the model predictions, however, was not reported.

Building upon these past studies, we report a combined experimental and numerical modeling study of the dynamics of axisymmetric liquid bridges that are coaxially stretched between two fully wetted disks. We focus on the deformation and rupture behavior of micro-scale liquid bridges over a much wider range of stretching velocities than the previous studies, up to 3 m/s. The dependence of the rupture length and rupture location on the stretching velocity, liquid properties, and liquid volume is systematically investigated. This work provides direct experimental validation of our numerical model based on a moving mesh method and offers physical insights useful for applying deformable microscale liquid elements as reversibly switchable mechanical or thermal interfaces.

3.2 Numerical Simulation

We consider the dynamics of an axisymmetric liquid bridge confined between two parallel fully-wetted circular disks of the identical radius R and surrounded by the ambient air. The top disk is moved upward along the common axis of symmetry at a velocity u whereas the bottom disk is stationary. The common axis of the symmetry of the bridge and the disks are aligned with the gravity vector. The radial coordinate of the air-liquid interface is denoted as h.

The transient liquid flows inside the bridge and the surrounding air are modeled using the Navier-Stokes equations and associated initial and boundary conditions. Figure 3.1 shows the simulation domains and boundary conditions used in our study. The liquid and the air are assumed to be incompressible with the constant density, viscosity and liquid-air interface surface tension.

We assume that the contact lines remain pinned at the disk edges:

$$h\,(z = 0,\, t) = R,\; h\,(z = L,\, t) = R \qquad (3.1)$$

and that the no slip condition holds at the disk surfaces:

$$u_r\,(z = 0\,,\, t) = 0,\; u_z\,(z = 0,\, t) = 0 \qquad (3.2)$$

$$u_r\,(z = L\,,\, t) = 0,\; u_z\,(z = L,\, t) = u \qquad (3.3)$$

For our experiments discussed later, we indeed observed no noticeable contact line motion, at least to within our optical resolution of approximately 20 μm. The pressure outlet condition is specified at the top, bottom and outer boundaries of the air domain.

The liquid bridge is assumed initially at rest in its equilibrium condition at volume v and initial length l_0.

$$h\,(z,\, t = 0) = h_{eq}\,(z) \qquad (3.4)$$

$$u_r\,(z,\, t = 0\,) = 0,\; u_z\,(z,\, t = 0\,) = 0 \qquad (3.5)$$

The Navier-Stokes equations are solved using a time-dependent finite-element solver based on the backward difference scheme. We employ the Arbitrary Lagrangian-Eulerian (ALE) moving mesh method [66], [67] to handle dynamic deformation of the simulation domains and the moving boundaries. The evolution of the liquid-air interface is directly tracked using the instantaneous normal velocities of the fluid at the interface as obtained from solutions of the Navier-Stokes equations [68]. At each dynamically determined time step, new mesh coordinates are generated to account for the movement of the boundaries.

The mesh quality gradually degrades as the simulation domains deform. An automatic remeshing method is adopted to periodically generate a new mesh when the mesh quality index falls below a threshold value. The maximum allowed time step is limited to $10^{-6}/u$ where u is the stretching velocity. The liquid volume is monitored during the entire simulation process to confirm that any variation stays below 0.1%.

A typical simulation run starts with a liquid bridge at its equilibrium state as obtained by setting the stretching velocity u to zero. A predefined temporal velocity profile is next applied to the top disk to emulate a stretching process. The bridge shapes (as defined by the locations of the air-liquid interface) and the velocity and pressure distributions are recorded at each time step until rupture occurs. The liquid bridge is considered ruptured when the minimum radius of the liquid bridge at any point along its length reaches 0.01% of the disk radius R.

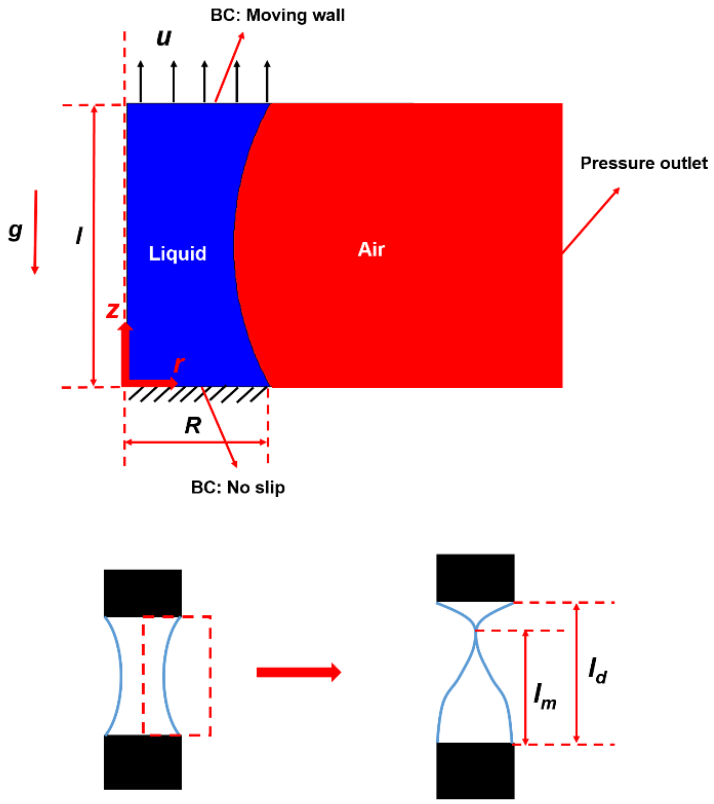

Figure 3.1: Schematic of the simulation domains and boundary conditions used to model an axisymmetric liquid bridge, which is held between two parallel coaxial disks of equal radii R (not shown) and stretched at a velocity of u. We define a cylindrical coordinate system {r, z} whose origin is located at the center of the bottom disk. The rupture distance and the rupture location are noted as l_d and l_m, respectively.

Test simulation runs were conducted with a very small disk velocity (0.001 mm/s) to confirm that we can replicate static stability limits predicted by the surface energy minimization algorithm [41]. We further confirmed that the rupture distances predicted by our numerical simulation agree with the values reported for moderate stretching velocities by Yildirim and Basaran [65] to within 2%.

A mesh independence study was also carried out. We confirmed that doubling the number of mesh elements results in less than 1% changes in the predicted rupture distances and partial liquid volumes.

To help generalize our results, we normalize relevant variables using the disk radius R as the characteristic length scale of the system and $U_c = (\sigma/\rho/R)^{1/2}$ as the characteristic velocity scale. The corresponding characteristic time scale is $t_c = (\rho R^3/\sigma)^{1/2}$. The governing dimensionless groups are: 1) the dimensionless stretching velocity $U \equiv \sqrt{\rho R u^2/\sigma}$; 2) the Ohnesorge number $Oh \equiv \mu/\sqrt{\rho R \sigma}$; 3) the Bond number $Bo \equiv g\rho R^2/\sigma$; 4) the dimensionless initial bridge length $L_0 \equiv l_0/R$; 5) the dimensionless liquid volume $V \equiv v/\pi R^3$.

The dimensionless stretching velocity can be re-expressed as $U = \sqrt{We}$, where *We* is the Weber number. The Weber number measures the importance of inertial force over surface tension force. The Ohnesorge number *Oh* measures the importance of viscous force over surface tension force and the Bond number *Bo* measures the importance of gravitational force over surface tension force. Since we are most interested in the dynamics of sub-millimeter and microscale liquid bridges, the Bond number is kept small ($Bo < 0.05$). We note that the Bond number may alternatively be defined as $Bo \equiv g\rho l^2/\sigma$, where l is the length of the liquid bridge. This may reflect the effect of the gravity more accurately but it is not convenient to use as the bridge length changes with time. The particular definition of the Bond number used should not affect our results as the gravity is explicitly accounted for in our numerical simulation.

3.3 Experiments

Experiments are conducted to allow direct validation of our predictions from the 2D axisymmetric model. To achieve stretching velocities as high as 3 m/s, we have developed an impact-driven setup schematically illustrated in Fig. 3.2. The liquid bridge is held between the parallel surfaces of two cylindrical stainless steel disks of the same radius. The disks are coaxial with the liquid bridge. The disk radius R is fixed at 0.5 mm for all the results reported in the article. The parallel surfaces of the disks are machined flat and held perpendicular to the disk axis so that the liquid completely wets the surfaces and the contact lines remain pinned on the sharp edges of the disk surfaces.

The bottom disk is fixed and the top disk is attached to a plate that can move vertically along a cylindrical slide guide. A high-striker mechanism is implemented to apply impact to this movable plate. A weight released from a certain height accelerates as it falls and activates a striker, which is coaxial with a movable plate. The plate and hence the upper disk then accelerate to a target velocity, typically within 1 ms. By changing the initial height of the falling weight, different stretching velocities can be achieved.

In a typical experimental run, two disks are first separated by a target initial distance. A liquid bridge is next formed by depositing a desired amount of liquid into the space between the two disks using a pipette with a resolution of 0.002 μL. The liquid bridge is next allowed to relax into its equilibrium state. We independently confirm the liquid volume by integrating the bridge cross section obtained through optical imaging under the assumption that the liquid bridge is axisymmetric. In one reproducibility study, the maximum difference between the targeted and

measured liquid volumes were 3% over 10 independent measurements. The measured rupture distances varied by less than 5% over these measurements.

A high speed camera (FASTCAM MC2, Photron Inc.) with a frame rate of 8000 fps is used to capture temporal trajectories of the upper disk and variations in the bridge shape. The acquired digital images are analyzed using Matlab and ImageJ to extract the instantaneous positions of the upper disk and the liquid-air interface. Representative temporal velocity profiles of the upper disk are shown in Fig. 3.3.

For each experimental condition, measurements were repeated at least 4 times to ascertain the reproducibility of the results.

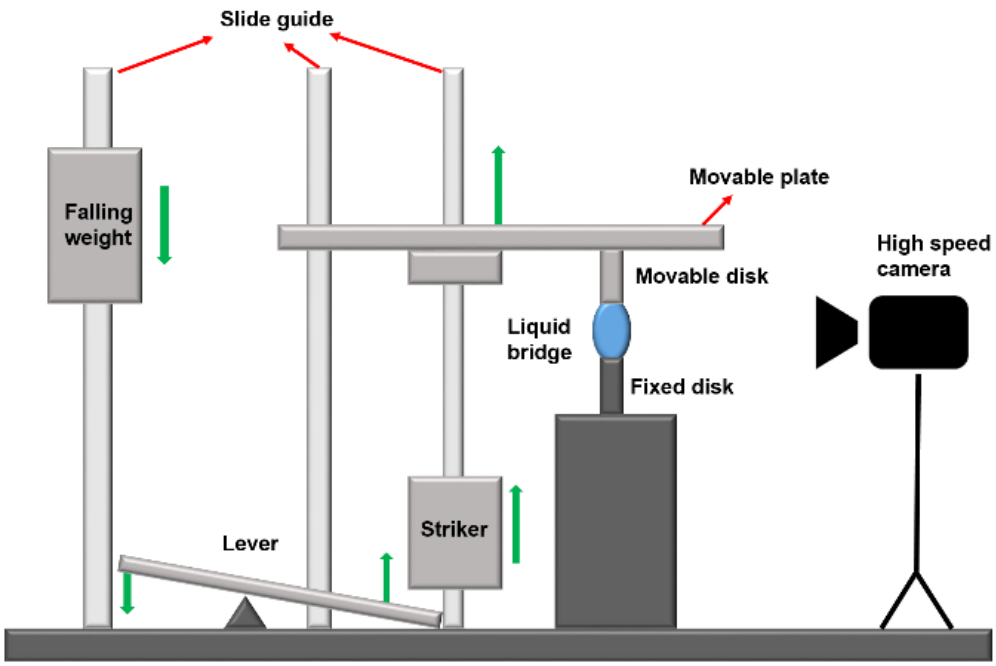

Figure 3.2: Schematic of the experimental setup used to uniaxially stretch the liquid bridge at varying stretching velocities.

To investigate the effects of the physical properties of the liquid, aqueous solutions of glycerol at different weight concentrations (0%, 20%, 40%, 60%, 80%) are used[69]. The densities and surface tensions of the aqueous solutions are similar to each other, varying by less than 30%, whereas their viscosities vary by more than three orders of magnitude. This allows us to explore large variations in the *Oh* number while maintaining the Bond number relatively constant.

Experiments were performed for different values of the velocity of the upper disk, liquid properties, and initial liquid bridge lengths. The Ohnesorge number ranges from 0.002 to 0.5, the disk velocity from 0.1 m/s to 3 m/s, and the initial dimensionless bridge length L_0 from 0.2 to 3. The dimensionless liquid volume V is fixed at 2.

While one can readily assign arbitrary temporal velocity profiles in numerical simulations, achieving infinite acceleration and maintaining a constant disk velocity in real experiments is not feasible due to finite inertia, gravity and friction.

To help present and interpret our data, we therefore performed two sets of simulations using two different sets of velocity profiles. The first set of velocity profiles (actual profiles) is obtained by analyzing the trajectories of the upper disk for direct comparison with the experimentally determined bridge profiles and rupture distances. The second set of velocity profiles is approximate idealized velocity profiles (idealized profiles) that consist of the linear ramp up phase and the constant "average" velocity phase. Simulations based on these idealized profiles are meant to help identify general trends. The average velocity is set to match the total distance traveled by the upper disk up to a bridge rupture point. Figure 3.3 shows representative actual and corresponding ideal velocity profiles, which are input into our numerical simulations.

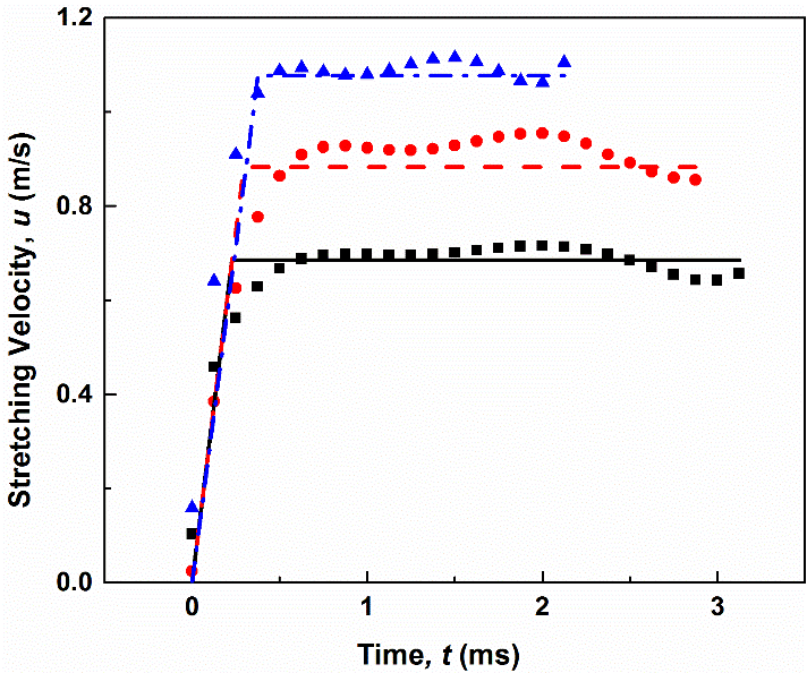

Figure 3.3: Representative actual (symbols) and idealized (lines) temporal velocity profiles of the upper disk.

3.4 Results and discussion

The dynamics of a stretching liquid bridge of a given dimensionless initial length L_0 is governed by the dimensionless groups defined earlier: the Ohnesorge number *Oh*, the dimensionless stretching velocity *U* (or the Weber number $We = U^2$), the Bond number *Bo*, and the dimensionless bridge volume *V*.

3.4.1 Validation of the model static rupture distances

As an independent validation of our numerical model, we conducted numerical simulations for a very small stretching velocity (0.001 mm/s) and compared the results with the rupture distances under quasi-static conditions reported in the literature. Under quasi-static conditions, the rupture distance is governed by the contact angles, θ_1 and θ_2, on the two disks.

Figure 3.4 compares the results obtained using the energy minimization algorithm (Surface Evolver) and the results obtained in our numerical simulations for a symmetric surface condition ($\theta_1 = \theta_2$). Figure 3.5 makes similar comparison for asymmetric surface conditions ($\theta_1 \neq \theta_2$).

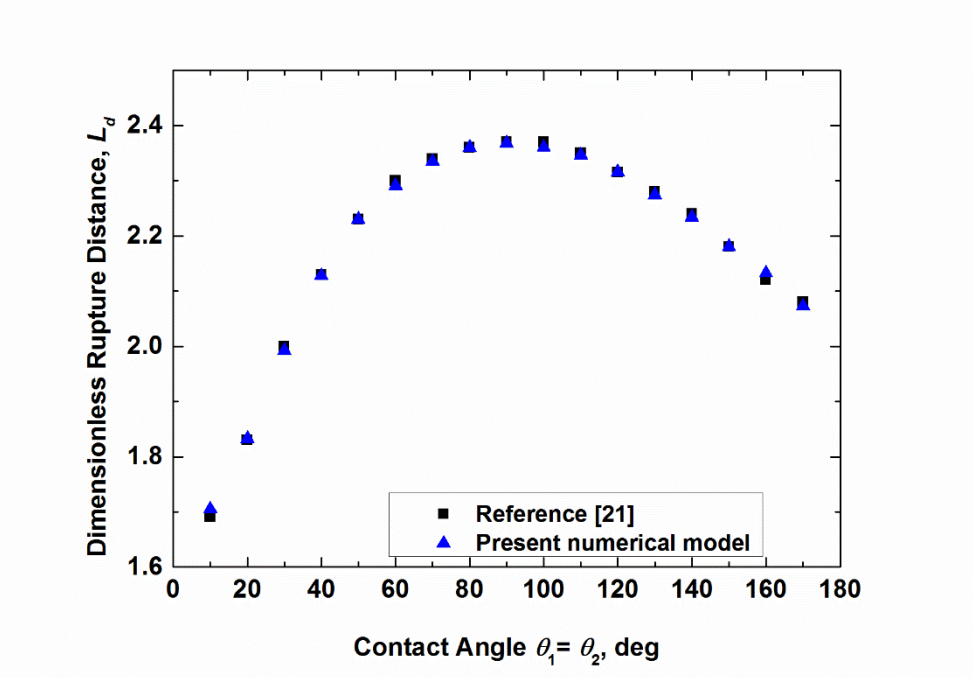

Figure 3.4: Comparison of the predicted rupture distances as a function of the contact angle (symmetric cases). The squares are the results from reference and the triangles are from our numerical simulation.

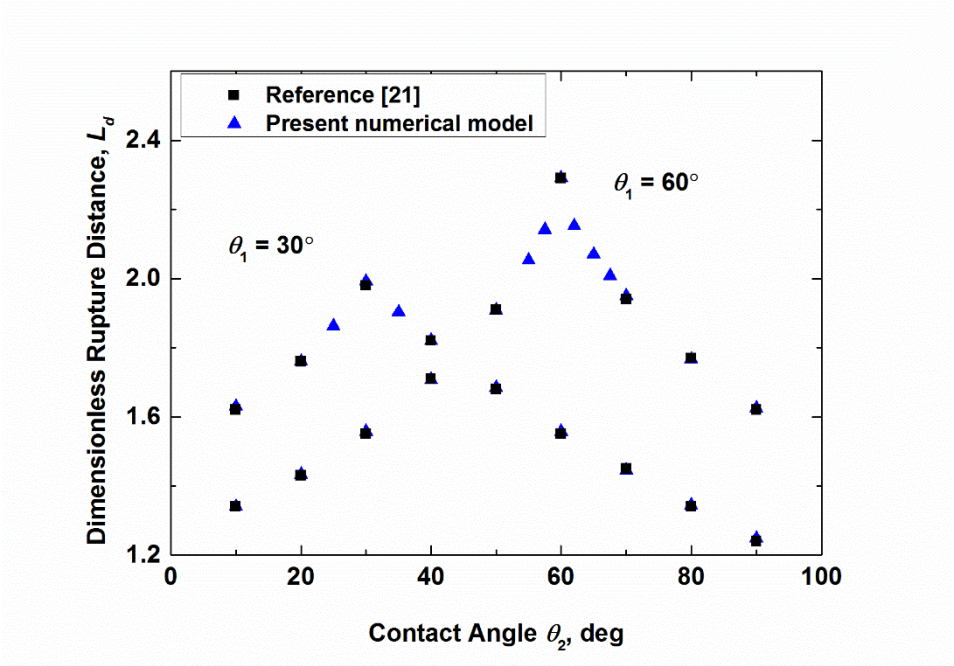

Figure 3.5: Comparison of the predicted rupture distances as a function of the contact angle on the bottom circular disk for two different values of the contact angle on the top circular disk (asymmetric cases). The squares are the results from Reference [21] and the triangles are from our numerical simulation.

3.4.2 Dynamic deformation of liquid bridges

We first compare the predicted liquid bridge profiles with the experimentally measured profiles for liquid bridges with a low (0.05) and a high (0.5) Ohnesorge number. The dimensionless stretching velocity U is fixed at 1 (U = 1). All the results presented in the article have been obtained for liquid bridges with L_0 = 2.

Figure 3.6 shows the temporal evolution of the simulated and experimentally measured shapes and minimum neck radius of the liquid bridge with an Ohnesorge number of 0.05 (a 60%

glycerol solution). As shown in the inset, the instant the bridge is stretched, necking first occurs in the upper portion of the liquid bridge. As the stretching continues, the necked portion of the liquid bridge gradually contracts further, ultimately leading to rupture. As the liquid bridge breaks up, the upper portion of the bridge forms a near spherical droplet whereas the lower portion of the bridge develops an elongated liquid thread. The temporal evolution of the dimensionless minimum neck radius h_{min}/R is shown in Fig. 3.6. The neck radius decreases at higher rates in the early stage of stretching than near rupture partly because further increase in the capillary pressure is opposed by the inertia and viscous effects.

Figure 3.7 shows the corresponding results for a liquid bridge with a higher Ohnesorge number (0.5 for an 80% Glycerol solution). The liquid bridge again first contracts at its upper portion but then develops into an almost symmetric (top to bottom) vase-like shape. A long cylinder-like liquid thread develops for the bridge with the higher Ohnesorge number. The liquid thread only gradually thin down as the stretching continues. As a result, the rupture time is significantly longer than that for the bridge with the smaller Ohnesorge number. The different manners in which the two liquid bridges evolve suggest one way to control the rupture of liquid bridges by simply choosing liquids with different Ohnesorge numbers.

For both cases, the experimental results and numerical predictions agree reasonably well in terms of the bridge shape and also the minimum neck radius. The maximum deviation is approximately 3%.

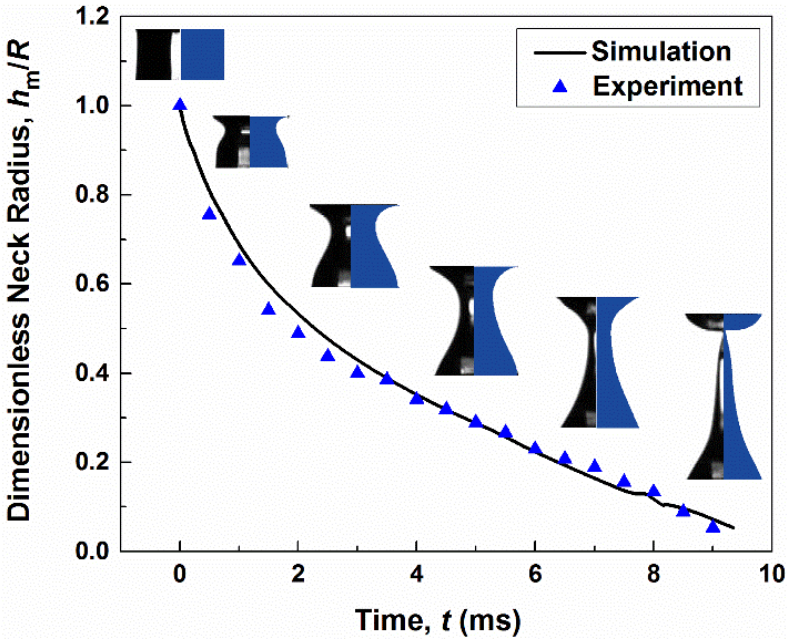

Figure 3.6: Temporal evolution of the predicted and experimentally determined minimum neck radius and bridge profiles (inset images) for a bridge with an Ohnesorge number of 0.05 (a 60% glycerol solution).

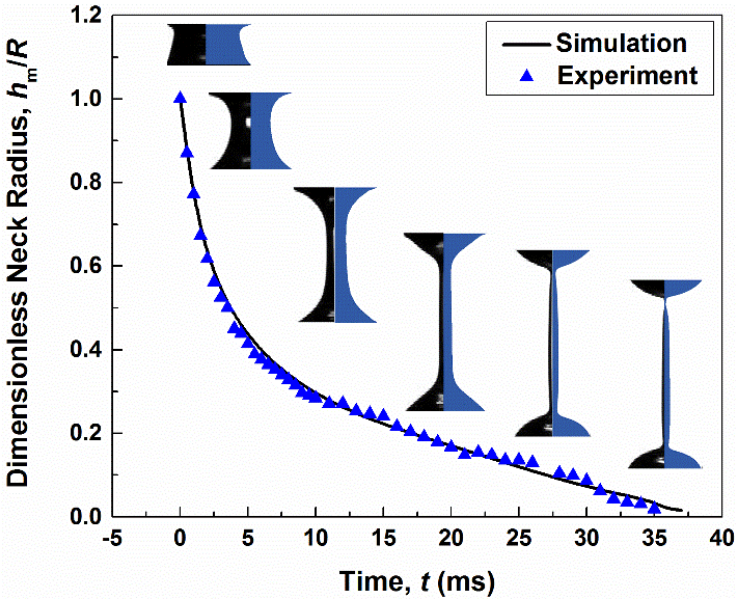

Figure 3.7: Temporal evolution of the predicted and experimentally determined minimum neck radius and bridge profiles (inset images) for a bridge with an Ohnesorge number of 0.5 (an 80% glycerol solution).

We note that, although the temporal evolution of the minimum neck radius is qualitatively similar for the two cases with different Ohnesorge numbers, the underlying details of the dynamics are very different. To gain further insights into the dynamics of liquid bridge rupture, we next examine internal pressure distributions.

Figure 3.8 shows the numerically computed liquid bridge profiles and corresponding internal pressure distributions for low and high Ohnesorge number cases. The dimensionless pressure within a liquid bridge is given, to the leading order, by $2H/Oh - \partial U_z/\partial z$. Here, H is the local mean curvature of the interface and U_z is dimensionless velocity in the z direction[65]. The capillary pressure $2H/Oh$ and the viscous pressure $\partial U_z/\partial z$ compete to determine the total pressure within the liquid bridge.

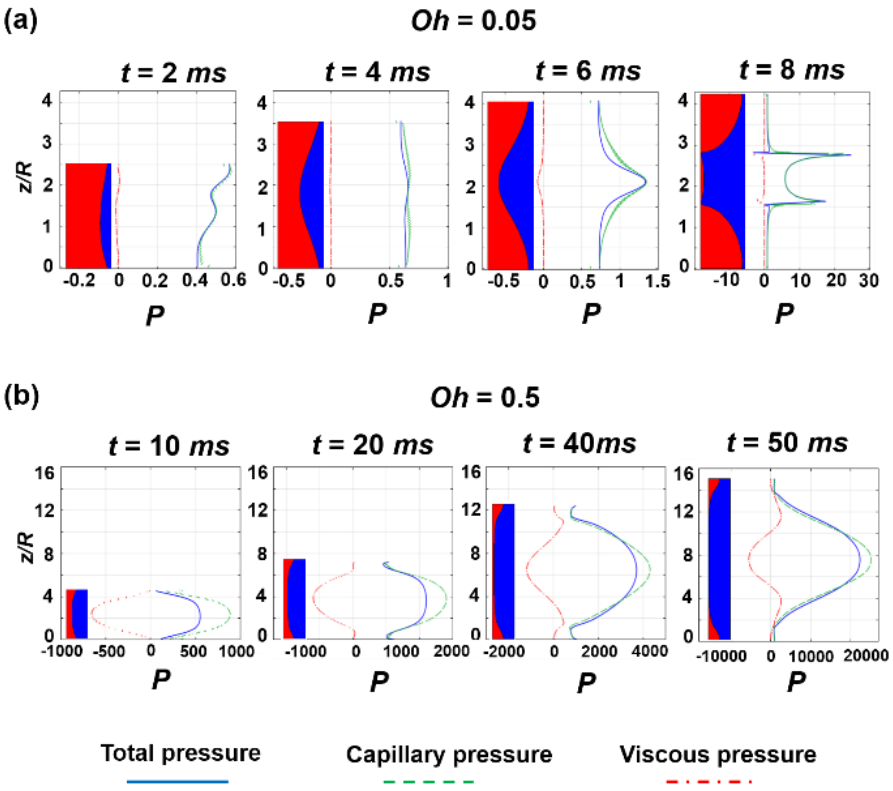

Figure 3.8: The predicted dimensionless pressures and liquid bridge profiles for a) Ohnesorge number *Oh* = 0.05 and b) Ohnesorge number *Oh* = 0.5. The dimensionless stretching velocity *U* is fixed at 1.

For the liquid bridge with the lower Ohnesorge number (Fig. 3.8a), the viscous pressure is negligible compared with the capillary pressure. As a result, the bridge generally follows a curvature-controlled rupture process. The bridge develops a necking point and the liquid is rapidly expelled away from this point due to high spatial capillary pressure gradients. This leads to a rapid bridge break up and a small rupture length.

For the liquid bridge with the higher Ohnesorge number (Fig. 3.8b), the viscous pressure can be comparable to the capillary pressure. It effectively opposes the capillary pressure gradient that expels the liquid away from the center. This drastically changes the total pressure profile.

The pressure within the bridge is more uniformly distributed and virtually symmetric. No pronounced necking point with a distinct large curvature is developed. Instead, the liquid bridge supports a long stable liquid thread, which gradually thins down until the bridge ruptures. This stabilizing effect of the viscous force delays rupture and leads to larger rupture distances.

3.4.3 Rupture distance: the effects of *U* and *Oh*

We next examine the effects of the Ohnesorge number *Oh* and the dimensionless stretching velocity *U* (or Weber number) on the rupture dynamics of liquid bridges.

We first discuss simulation results where the Bond number is set to be zero to remove any complication from the gravitational effect. This is reasonable for micro-scale liquid bridges. Numerical simulations are performed over a wide range of stretching velocities for liquid bridges with different Ohnesorge numbers. As a reminder, the rupture distance is nondimensionalized as $L_d = l_d/R$, where l_d is the separation of the two disks at the point of bridge rupture. The dimensionless rupture location is defined as $L_m = l_m/R$, where l_m is the vertical distance from the rupture point to the bottom disk (Fig. 3.1).

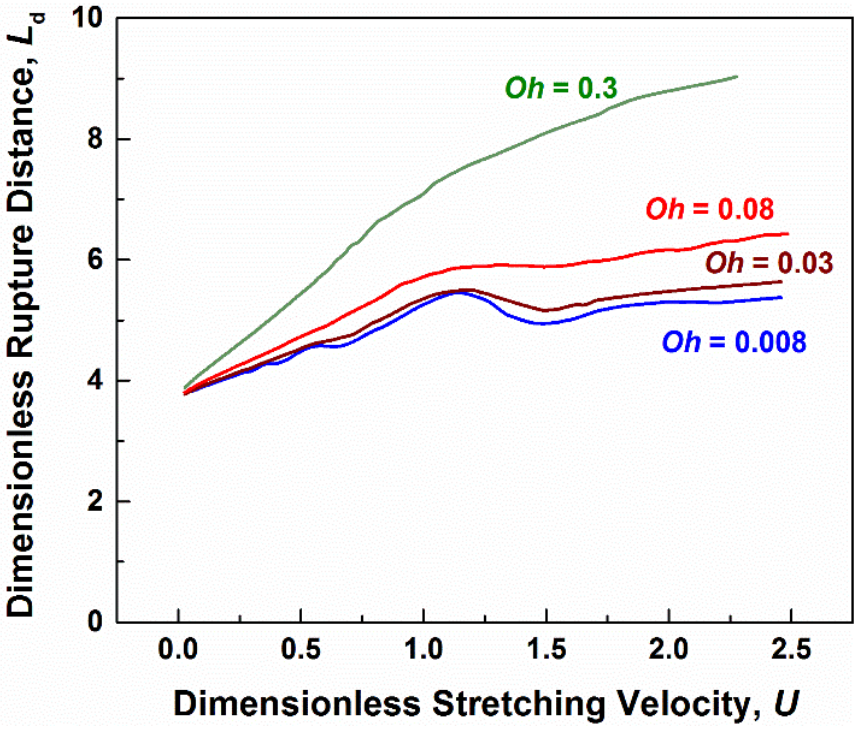

Figure 3.9: Predicted rupture distance L_d as a function of the stretching velocity U for liquid bridges with different values of the Ohnesorge number. The Bond number Bo is set to be zero.

The predicted dimensionless rupture distance L_d is shown in Fig. 3.9 as a function of the stretching velocity U for different values of the Ohnesorge number. When a liquid bridge is axially stretched at a very low velocity, the bridge shape at each instant closely resembles the quasi-equilibrium shape that it would have if the moving disk were instantaneously brought to rest and the bridge were allowed to relax to its equilibrium state. Under this condition, the rupture distance that the bridge attains exceeds the maximum stable length of a nominally identical static bridge by only a small amount. The rupture distance is also relatively insensitive to the Ohnesorge number. This is consistent with well-established static stability of liquid

bridges [70] and prior experimental measurements at low stretching velocity (< 6 mm/s) [40]. In contrast, at higher stretching velocities, the departure of the transient shapes from the equilibrium ones becomes larger and the rupture distance is increased substantially over the maximum stable length of a comparable static bridge.

For a liquid bridge with a relatively small value of *Oh* (0.008), rather complex trends are observed in the dependence of it rupture distance on the stretching velocity. These are represented by the *relative* rupture location switching and the liquid thread shape changes. Figure 3.10 shows a zoomed view of the rupture distance plot with matching bridge profiles illustrating these two phenomena.

As mentioned before, at very small stretching velocities, a liquid bridge approximately maintains its quasi-static state. Rupture occurs almost simultaneously at the upper and lower necking points. As the stretching velocity increases, however, the rupture location shifts.

For liquid bridges with small values of *Oh*, the rupture process is governed primarily by localized peaks in the capillary pressure. The rupture occurs at or near the maximum local mean curvature point(s). Two potential rupture points (one closer to the top disk; the other closer to the bottom disk) exist due to the opposite signs of the two principle curvature components contributing to the total local mean curvature. We will refer to them as the upper and lower potential rupture point, respectively.

As the stretching velocity is increased, rupture occurs first on the lower potential rupture point (Fig. 3.10 inset I). As the stretching velocity is further increased, the rupture location switches to the upper point (Fig. 3.10 inset III). We call this the relative rupture point switching. There may be additional rupture location switching events (back to the lower point and then to

the upper point) as the stretching velocity is further increased for bridges with relatively low Ohnesorge numbers. The rupture distance stays relatively constant or drops slightly with increasing stretching velocity during these switchings.

One consequence of the rupture location switching is on the trajectory of satellite droplets formed after a liquid bridge ruptures. These satellite droplets may either recoil toward the residual droplet on the bottom disk or the top disk depending in part on the relative rupture location[65].

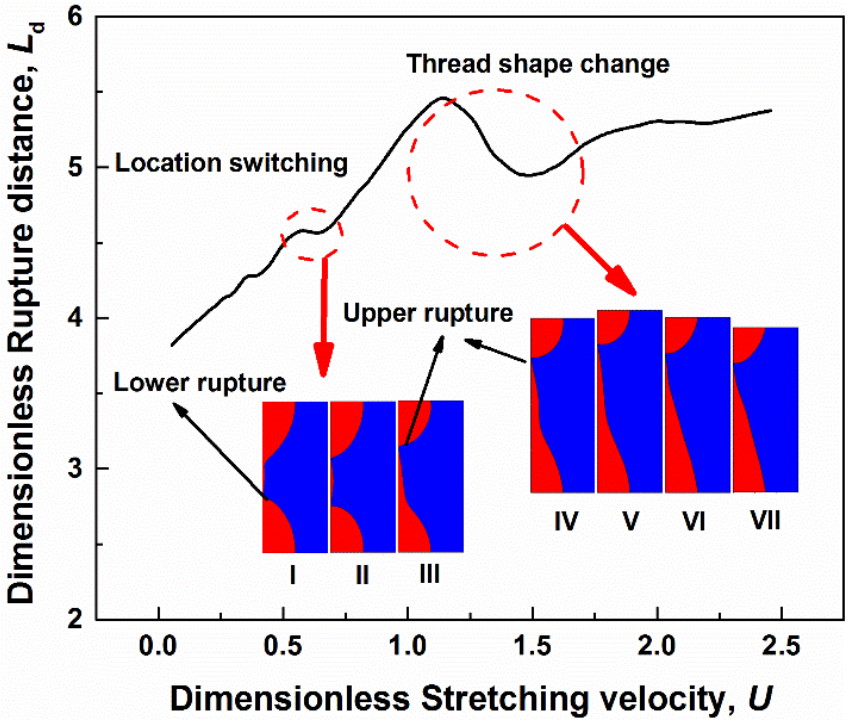

Figure 3.10: The predicted rupture distance as a function of the dimensionless stretching velocity (The case of Oh = 0.008 in Fig. 3.9). The insets illustrate the rupture location switchings and the thread shape change discussed in the text.

When the stretching velocity becomes large enough and the inertia effect is significant, a pronounced necking develops near the upper portion of the liquid bridge almost immediately after the upper disk is set into motion. This leads to a thin necked portion with a large local mean curvature. The liquid bridge then always ruptures at this upper portion (Fig. 3.10 insets IV-VII).

We consider the transition velocity U_{tr}, approximately 1 in Fig. 3.10, as the velocity above which no further rupture location switching happens for bridges with a given value of *Oh*. That is, the liquid bridges always rupture at the upper rupture points at velocities larger than this transition velocity. We performed additional simulations for liquid bridges with L_0 (= l_0/R) different from 2. The simulation results show that the transition velocity is weakly dependent on the Ohnesorge number but is a function of the initial aspect ratio, defined as $l_0/(2R)$, of the liquid bridge. The disk radius *R i*s fixed at 0.5 mm. Figure 3.11 shows the dimensionless transition velocity as a function of the aspect ratio. Long and thin (large aspect ratios) liquid bridges tend to experience the transition at lower stretching velocities than short and fat (small aspect ratios) liquid bridges. The gravity has a negligible effect on the transition velocity.

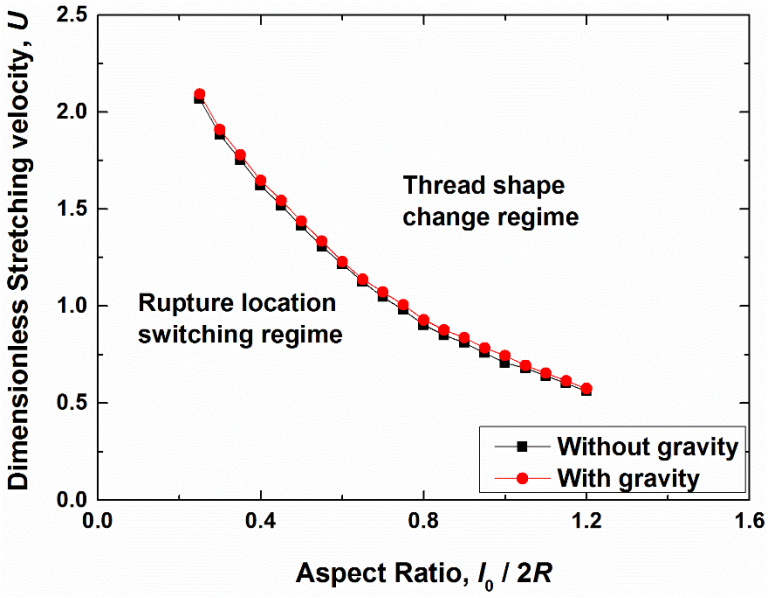

Figure 3.11: The dimensionless transition velocity as a function of the liquid bridge aspect ratio with and without the gravity. The disk radius R = 0.5 mm.

At still higher stretching velocities, even though the rupture points stay in the upper portion of the liquid bridge, we observe an additional anomaly in the stretching velocity dependence. That is, the liquid thread in the lower portion of the liquid bridge exhibits a change in shape from a long and thin needle-like structure (Fig. 3.10 insets IV-V) to a short and thick cone-like structure (Fig. 3.10 insets VI-VII). Accompanying this shape change is reduction in the rupture distance with increasing stretching velocity. In the long needle-like structure, locally enhanced capillary pressure gradients around the lower potential rupture point cause the liquid to be expelled, leading to the formation of an elongated liquid thread of varying widths. In the short and thick cone-like structure, in contrast, the lower potential rupture point becomes insignificant and the thread stays short.

Aside from these localized anomalies, the rupture distance generally increases with stretching velocity. This overall trend is consistent with the stabilizing effect of increasing inertial force over surface tension force as measured by the dimensionless velocity U (or Weber number $We = U^2$).

For liquid bridges with the larger Ohnesorge numbers (Oh = 0.08 and 0.3 in Fig. 3.9), localized anomalies are less obvious, all but indiscernible for the highest Oh considered. Increasing Oh (for example, by increasing the viscosity and/or reducing the surface tension) has added stabilizing effects on the liquid bridge, enabling the formation of highly elongated liquid threads.

We next compare our experimental results with the numerical model predictions for liquid bridges of different values of Oh. Figure 3.12 shows the experimentally captured and predicted liquid bridge profiles right before rupture for different stretching velocities. Liquid bridges with Oh = 0.005, 0.05 and 0.5 are considered. For a low Oh (A: Oh = 0.005) liquid bridge, the rupture position switching (I to III) and the thread shape change (IV to VI) are observed as predicted in our simulations. These phenomena are less obvious as the Oh number increases (B: Oh = 0.05) and all but disappear when Oh is sufficiently high (C: Oh =0.5). The transition from the rupture location switching regime to the thread shape change regime occurs between Columns II and III in Fig. 3.12 or for stretching velocities of approximately 1 for the cases considered in the present study. The experimental results agree reasonably well with the predictions.

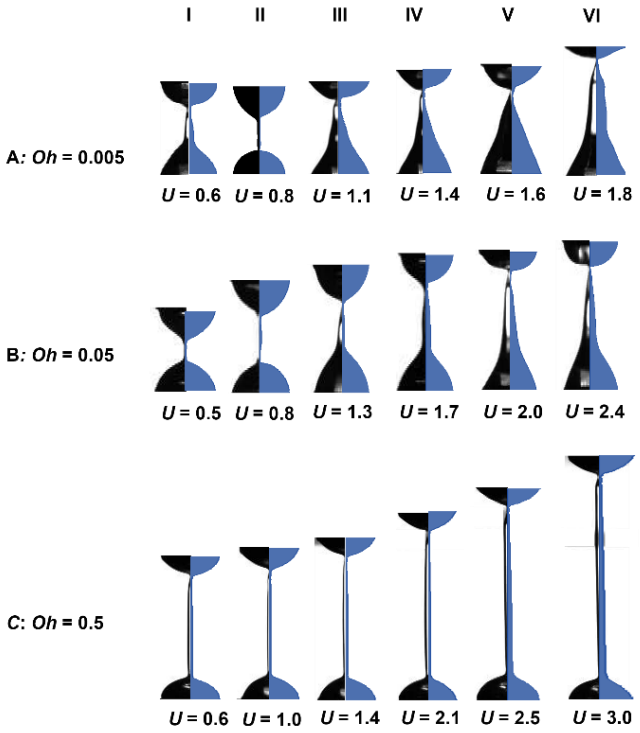

Figure 3.12: Comparison between the experimentally captured and predicted liquid bridge profiles right before rupture for different stretching velocities. Results are from liquid bridges with *Oh* = 0.005, 0.05, and 0.5.

Figure 3.13 compares the experimentally measured and predicted dimensionless rupture distances as a function of the dimensionless stretching velocity for liquid bridges with a low value of *Oh* (= 0.005). The experiments are repeated four independent times and we report the average values as the filled triangles in Fig. 3.13. Standard deviations are reported as error bars.

The hollow symbols in Fig. 3.13 correspond to the simulation results obtained using actual velocity profiles obtained for each individual experimental condition. The corresponding individual experimental results are shown as the filled diamonds. They agree reasonably well with < 10% deviation.

To help clarify a general trend, we also show the simulation results obtained using "idealized" temporal velocity profiles (Section 3, Fig. 3.3) as the solid line.

Figure 3.14 shows similar comparison for liquid bridges of a moderate value of *Oh* (= 0.05). The increase in *Oh* is mainly due to a larger viscosity of the liquid used (a 60% glycerol solution). One can notice almost monotonic increase in the rupture distance with the increasing stretching velocity. Local anomalies (the rupture location switching and the thread shape change) are barely distinguishable. Again, reasonable agreement is observed between the predicted and experimental results.

For the liquid bridge with the highest value of *Oh* we considered (Fig. 3.15), the rupture distance increases monotonically with the stretching velocity throughout the entire velocity range considered. Compared with the other liquid bridges with the lower Ohnesorge numbers, a drastically longer liquid thread is developed. As a result, the rupture distance is significantly larger for a given stretching velocity.

The observation that liquid bridges with different Ohnesorge numbers show distinct rupture behaviors can be taken advantage in designing practical devices. For example, one may choose high *Oh* liquid bridges to achieve highly stretchable liquid interconnections for flexible or reconfigurable electronic and optoelectronic devices. Alternatively, one may wish to minimize the rupture distance for fast switching of thermal or electrical conductance by identifying a local minimum in the rupture distance around the thread shape change regime.

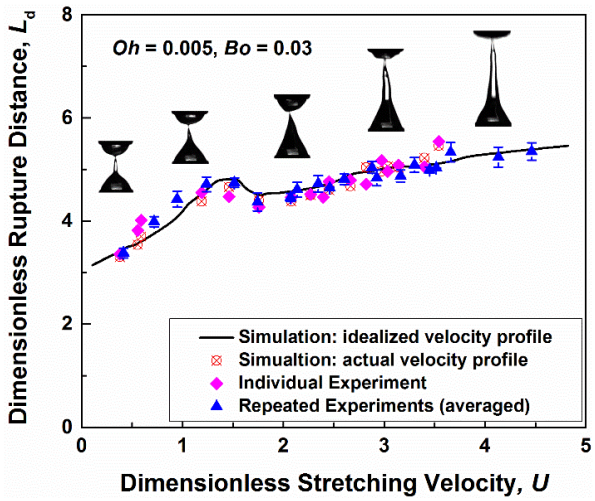

Figure 3.13: Predicted and experimentally determined dimensionless rupture distance as a function of the dimensionless stretching velocity. The bridge is made of water (*Oh* = 0.005, *Bo* = 0.03). Superposed on the plot are experimentally obtained images of the liquid bridge at the incipience of rupture at several different stretching velocities.

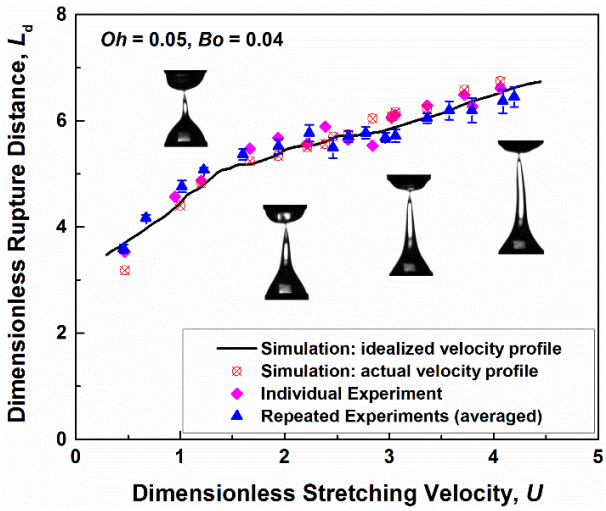

Figure 3.14: Predicted and experimentally determined dimensionless rupture distance as a function of the dimensionless stretching velocity. The bridge is made of a 60% glycerol solution (*Oh* = 0.05, *Bo* = 0.04).

Superposed on the plot are experimentally obtained images of the liquid bridge at the incipience of rupture at select stretching velocities.

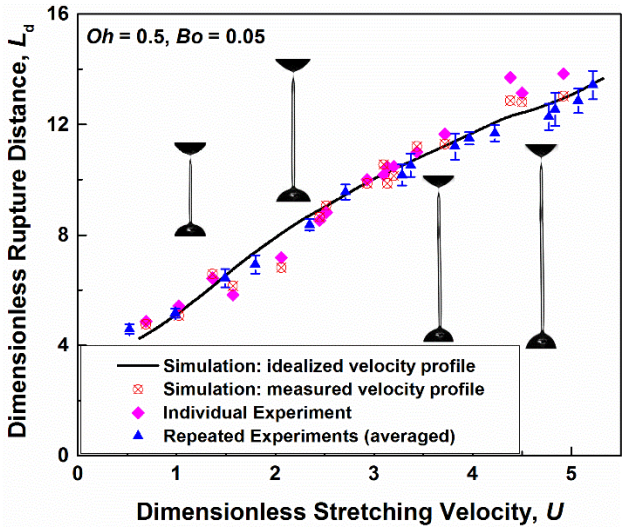

Figure 3.15: Predicted and experimentally determined dimensionless rupture distance as a function of the dimensionless stretching velocity. The bridge is made of an 80% glycerol solution (Oh = 0.5, Bo = 0.05). Superposed on the plot are experimentally obtained images of the liquid bridge at the incipience of rupture at select stretching velocities.

We note that all the results presented in the article are obtained under asymmetric stretching conditions where only the top disk is in motion and the bottom disk remains stationary. Under the symmetric stretching condition, the top and bottom disks would be stretched in opposing directions, each at half the total target stretching speed. At higher stretching velocities, where the inertia effects are significant, the rupture distances under the symmetric and asymmetric stretching conditions significantly deviate from each other. The symmetric stretching condition suppresses the development of pronounced upper potential rupture points and associated local anomalies.

The experimentally measured and predicted rupture distances as a function of *Oh* for different stretching velocities are shown in Fig. 3.16. Similar results have been reported in previous experimental [40] and numerical modeling [65] studies but only at relatively low stretching velocities. Setting aside experimental uncertainties, for a given stretching velocity, we note that the rupture distance is rather insensitive to *Oh* when $Oh < 0.01$. Relatively speaking, it increases more rapidly with *Oh* when $Oh > 0.01$ as the rupture behavior changes from the capillary controlled necking to the viscous controlled thread thinning. The experimental results agree reasonably well with the predictions with deviation < 5 %.

We note in passing that we did not observe any "pre-mature" rupture of liquid bridges that resulted in smaller rupture distances than what we predicted. This may, however, be due to a specific set of experimental approaches/protocols we used. Under certain other conditions (for example, plates and/or liquid bridges are subjected to mechanical, electrical, or magnetic oscillations in addition to unidirectional stretching at a constant speed) one may potentially observe accelerated bridge rupture.

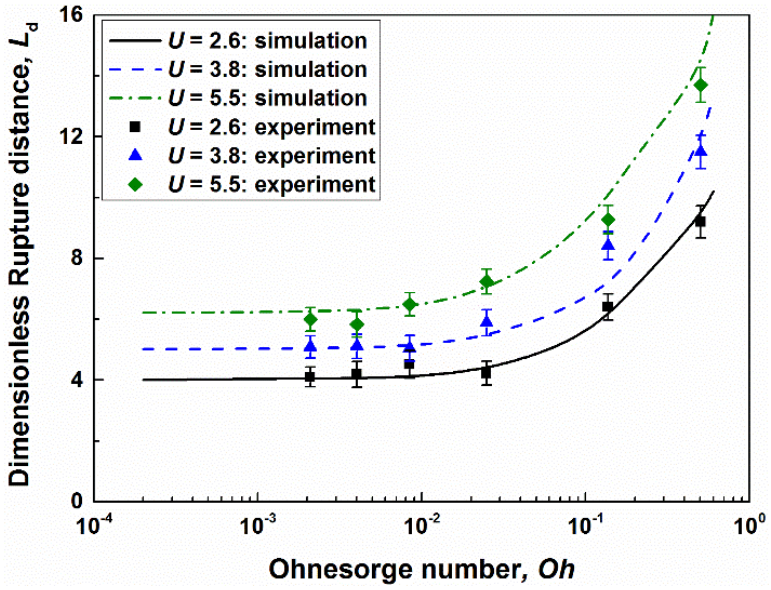

Figure 3.16: Predicted (lines) and experimental (symbols) results of the dimensionless rupture distance as a function of the Ohnesorge number for different stretching velocities.

3.4.4 Relative Rupture Location and Partial Liquid Volume

In Section 3.4.3, we discussed the relative rupture location switching as local anomalies observed in the stretching velocity dependence of the rupture distance. To illustrate this more systematically, we show the predicted and experimentally measured relative rupture locations L_m/L_d in Fig. 3.17 as a function of the dimensionless stretching velocity. Results are shown for bridges made of water and an 80% glycerol solution. We refer to cases where $L_m/L_d > 0.5$ as the upper point rupture mode and cases where $L_m/L_d < 0.5$ as the lower point rupture mode. For liquid bridges with a low value of *Oh* (e.g. water), the rupture location switches between the upper and lower potential rupture points at relatively low stretching velocities. When the stretching velocity is sufficiently large ($U > 1$), the rupture location switches back to and remains on the upper portion of the bridge. A similar trend is observed for a liquid bridge with a higher

value of *Oh* (80% glycerol solution) but with much smaller variations in the relative rupture distance as the switchings occur.

Another parameter of interest is the partial residual volume V_p, which is defined as the ratio of the volume V_b of the liquid remaining on the bottom disk after rupture and the total liquid volume V. Figure 3.18 shows variation in the partial volume as a function of the dimensionless stretching velocity for liquid bridges with different values of *Oh*. Under static conditions or extremely small stretching velocities, the partial volume is approximately 0.5 as the bridge breaks up symmetrically. Note that the two disks are nominally identical with the same contact angles in all cases considered in the present study. The symmetric rupture is consistent with the results of previously reported liquid partitioning studies [51]–[53].

As the stretching velocity increases, the relative rupture location switches between the lower to the upper potential rupture points. For the lower point rupture cases, the partial volume is less than 0.5 and the larger portion of the liquid will remain pendant to the top disk. For the upper point rupture cases, the partial volume is larger than 0.5 at higher stretching velocities as a larger portion of the liquid forms a long thread at the bottom.

Note that the rupture distance anomaly caused by the thread shape change does not influence the increase in the partial volume with increasing stretching velocity. As inertial effects become dominant over surface tension effects, more liquid remains on the lower portion of the liquid thread despite such a shape change.

For the liquid bridge with the higher *Oh* (an 80% glycerol solution), the partial volume remains relatively insensitive to the stretching velocity when the velocity is relatively small. As the relative rupture location switches from the lower to the upper potential rupture points, the

partial volume increases with the stretching velocity. Compared with the bridge with the lower *Oh*, the effects of the rupture location switching and thread shape change on the partial volume is less pronounced due to the damping effect of viscosity over surface tension.

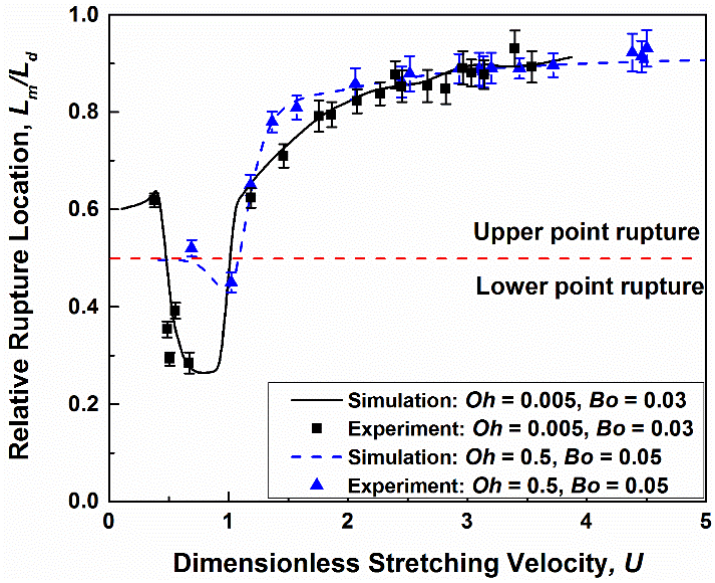

Figure 3.17: Simulation and experimental results of the partial volume as a function of the stretching velocity for water (*Oh* = 0.005, *Bo* = 0.03) and an 80% Glycerol solution (*Oh* = 0.5, *Bo* = 0.05).

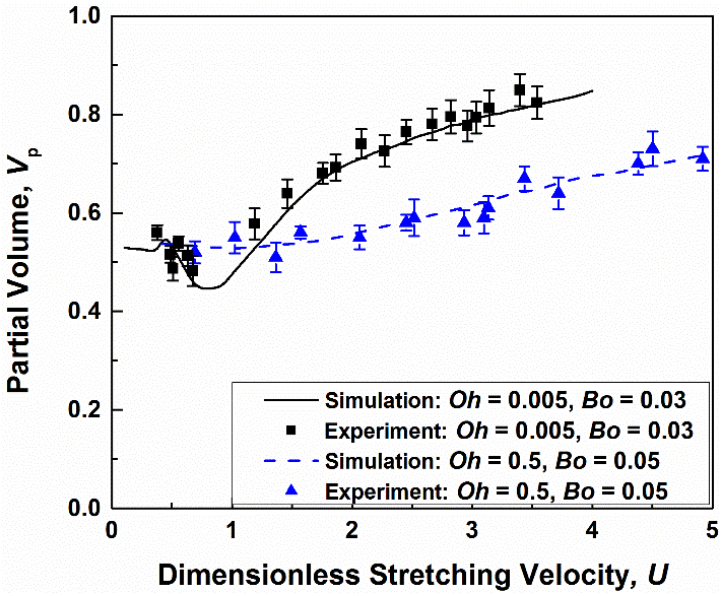

Figure 3.18: Simulation and experimental results of the partial volume as a function of the stretching velocity for water (Oh = 0.005, Bo = 0.03) and an 80% Glycerol solution (Oh = 0.5, Bo = 0.05).

3.4.5 Symmetric stretching

To gain further insight into the observed velocity-dependence of the rupture distance, we extended our numerical simulations to symmetric stretching situations under otherwise identical conditions. Under symmetric stretching, the top and bottom disks are stretched in opposing directions, each at half the total target stretching speed.

Note that we considered only asymmetric stretching in the main manuscript where only the top disk is in motion at the target speed whereas the bottom disk remains stationary.

The predicted dimensionless rupture distances L_d under the symmetric and asymmetric stretching conditions are shown in Fig. 3.19 as a function of the stretching velocity U. Four different values of the Ohnesorge number are considered. Figure 3.20 compares the predicted liquid bridge profiles under the asymmetric stretching conditions (left panel) and the symmetric

stretching conditions (right panel) right before rupture occurs. The results are presented for different stretching velocities and Ohnesorge numbers (*Oh* = 0.008 and 0.3).

Under symmetric stretching, the liquid bridge ruptures at two (upper and lower) potential rupture points simultaneously while under asymmetric stretching the relative location of the liquid bridge rupture shifts as a function of the stretching velocity (see Fig. 3.20). As expected, when the stretching velocity is very low (*U* of approximately 0.3 and below), there is no obvious difference between the symmetric and asymmetric stretching conditions).

At higher stretching velocities, due to the increasing inertial effects, the rupture distances under the symmetric and asymmetric stretching conditions significantly deviate from each other. The asymmetric stretching leads to more pronounced development of the upper potential rupture point and thereby reduces the rupture distance.

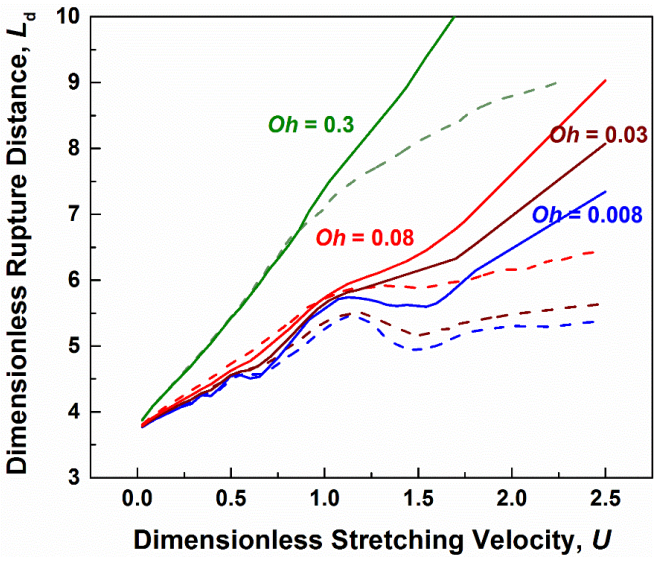

Figure 3.19: The predicted rupture distances L_d as a function of the stretching velocity U for liquid bridges with different values of the Ohnesorge number under the symmetric (solid) and asymmetric (dash) stretching conditions. The Bond number Bo is set to be zero.

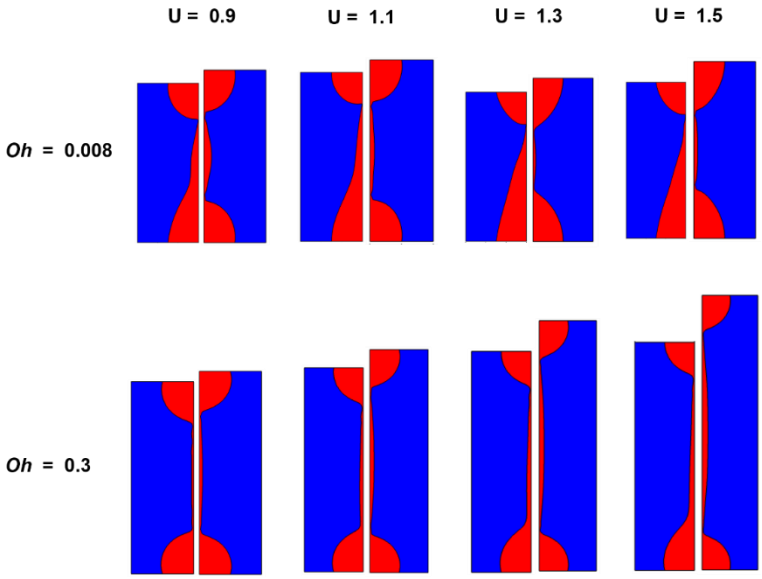

Figure 3.20: Comparison between the predicted liquid bridge profiles under the asymmetric (left panel) and symmetric (right panel) stretching conditions right before rupture for different stretching velocities for liquid bridges with Oh = 0.008 and 0.3.

3.5 Summary

In this chapter, the effects of inertial, viscous and surface tension forces on the dynamics of stretching liquid bridges are investigated using a combined experimental and numerical simulation study. The experiments and simulations are carried out for a wide range of dimensionless stretching velocities and Ohnesorge numbers. The rupture distance of a liquid bridge generally increases with stretching velocity due in part to the stabilizing effect of viscous and inertia force. For low-Oh liquid bridges, local anomalies in the rupture distance, such as the

relative rupture position switching and the thread shape change, occur as the stretching velocity is varied. Such anomalies are less visible for high-*Oh* liquid bridges. The partial volume of the liquid remaining on the bottom disk after rupture generally increases with increasing stretching velocity. Our study provides direct experimental validation of the numerical simulation approach based on the moving mesh scheme for capturing dynamics of capillary confined liquid bridges and their rupture. Our work helps develop a systematic design tool for utilizing liquid bridges as mechanical, electrical or thermal interfaces.

The present study focused exclusively on axisymmetric liquid bridges formed between two identical full-wetted disks. We note, however, that contact line motions on more general solid substrates can significantly affect the statics and dynamics of liquid bridge[71], including the bridge deformation and rupture patterns[53], [72]. Further studies on this rich topic, including accurate modeling of the mechanics of contact line pinning and unpinning[73] would be worthy extension of our work.

Chapter 4

Dynamics of Damped Oscillations during Capillarity-Driven Self-Alignments

In a capillarity-driven self-alignment process, a solid object suspended on a liquid bridge is aligned onto a desired position on the pre-patterned substrate through the combined action of capillary and dissipative forces. We report a study of the dynamics of damped oscillations during such self-alignment processes where we directly track the deformation of liquid menisci and motion of contact lines. Quantitative comparison with the experimental data reveal that the viscous shear stress exerted by mesoscale liquid flows is insufficient to explain the observed damping ratios. We identify an additional dissipative force arising from moving contact lines as a possible explanation for the discrepancy. Our model predictions based on an independently obtained friction coefficient show quantitatively good agreement with the experimental data.

4.1 Background

Capillary self-alignment is an intriguing approach that uses capillary forces exerted by deformed liquid bridges to register micro- and meso-scale objects on pre-patterned substrates. It is promising for various applications, including fabrication and/or packaging of micromachined devices, solar cell segments and biological samples through massively parallel alignments and assemblies on rigid and flexible substrates [74]–[77]. Self-assembly techniques have also been explored for accurate micro-handling and micro-positioning tasks in robotics and 3D integration [78]–[81].

Early studies of these self-assembly processes developed simplified models based on the energy minimization approach to predict capillary forces from the quasi-static geometries of liquid menisci. The contact lines were most often assumed to be spatially fixed. Dynamic responses of capillary assembly systems were then described using the predicted capillary forces while only approximately accounting for the viscous forces [82]–[86].

These rather simplistic models, however, were found insufficient in describing self-assembly processes involving relatively large displacements [87]–[89]. Here, one must accurately account for dissipated forces associated with contact line motions and internal liquid flows as well as capillary forces associated with large meniscus deformations. A recent study recognized the impact of contact line motion on initial acceleration but only considered its impact on capillary forces under the quasi-static approximation [90].

To circumvent the limitation of early quasi-static models, we develop a model that dynamically tracks the deformation of liquid menisci and the motion of contact lines by directly solving the Navier-Stokes equations. By directly comparing our model prediction with

experimental data for damped harmonic oscillations, we elucidate the relative importance of the line friction arising from contact line motion and the viscous forces arising from internal liquid flows.

4.2 Numerical model

We model transient liquid flows inside the liquid bridge by solving the Navier-Stokes equations using a time-dependent finite-element solver based on the backward difference scheme. The liquid (water) is assumed to be incompressible with the constant density, viscosity and liquid-air interface surface tension. We employ the Arbitrary Lagrangian-Eulerian (ALE) moving mesh method to handle dynamic deformation of the simulation domains and the moving boundaries [30]–[32]. We directly track the evolution of the interfaces using the instantaneous normal velocities of the liquid at the interface obtained from the solutions of the Navier-Stokes equations. At each adaptively determined time step, new mesh coordinates are generated to account for the movement of the interfaces.

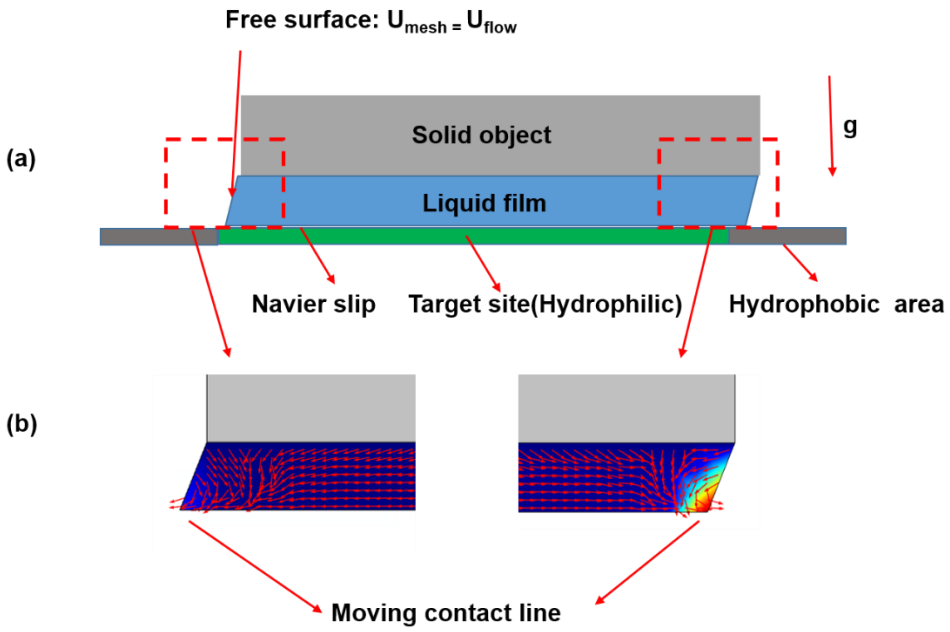

Figure 4.1: (a) Schematic of a self-assembly system where a solid substrate is floating on a thin liquid film within a target binding site; (b) the corresponding simulation domains and boundary conditions with red arrows showing the flow velocity distribution around the contact line.

Figure 4.1 shows the schematic of a self-assembly system where a solid substrate is floating on a thin liquid film within a target binding site and the corresponding simulation domains and boundary conditions. In traditional elastic models, the contact line is ideally fixed and thus no motion at the contact line is allowed. However, the contact line cannot be perfectly pinned in place in practical experimental conditions. In our model, the contact line is free to move along the substrate. To allow contact line motion, the solid liquid interface is imposed with the Navier slip boundary condition with a constant slip length. The Navier slip boundary condition enforces the slip condition $\boldsymbol{u} \cdot \boldsymbol{n}_{\text{substrate}} = 0$ and adds a friction force in the form of $F_{\text{fr}} = -\mu / \beta \cdot \boldsymbol{u}$, where $\boldsymbol{u}$ is the fluid velocity vector, μ is the viscosity of the liquid and β is the slip

length, which is typically in the order of 10 nm [91]. A slip length of 50 nm is used in the simulation and the variation of slip length has been proved to have negligible effect on the results by conducting simulations with slip length range from 1nm to 200 nm.

At the liquid solid contact point, an equilibrium contact angle boundary condition is applied to take into account the effect of substrate surface conditions. In experimental conditions, the target binding area is a hydrophilic island surrounded by hydrophobic areas. This imposes a chemical confinement on the liquid film to be within the binding area. To simulate this chemical confinement, hydrophilic and hydrophobic contact angles are specified for boundary conditions within and outside the target site respectively. A small buffer area with a length of 10 μm between the binding site and the surrounding area is used to allow a continuous transition from the hydrophilic to hydrophobic contact angle and avoid convergence issues due to the disruptive change of contact angle at the transition point.

The capillary and viscous shear forces exerted on the solid object by the liquid bridge and its internal flow are calculated at each time step. The resulting lateral displacement and velocity of the solid object are then used as boundary conditions for the next time step. The mesh quality gradually degrades as the simulation domains deform. An automated re-meshing method is adopted to periodically generate a new mesh when the mesh quality index falls below a threshold value. The maximum allowed time step is limited to 10^{-3} ms. The liquid volume is monitored during the entire simulation process to confirm that any variation stays below 0.1%.

4.3 Results and discussions

4.3.1 Experimental validation of the model

A typical self-assembly process consists of three dynamic regimes: transient wetting, acceleration and damped harmonic oscillation[89]. Upon the release of a solid object from its initial misaligned state, a liquid layer placed on the binding site wets the bottom surface of the object and forms a liquid bridge. Under the action of the capillary forces of the deformed meniscus, the object experiences acceleration towards its aligned "equilibrium" position. As the object overshoots the equilibrium position, the capillary forces reverse the direction and pull the object back towards the equilibrium position. Under the added actions of dissipative forces, the object undergoes damped oscillations until it stops at the final rest position.

The oscillation frequency and the damping ratio are typically used to describe a damped harmonic oscillation process. The oscillation frequency is calculated by the inverse of the oscillation period and the damping ratio by equation: $c = 2m \ln (A_0 / A_1) / dt$, where m is the mass of the solid component, A_0 and A_1 are the peak displacements at t_0 and t_1 respectively and $dt = t_1 - t_0$.

Figure 4.2 compares the experimentally obtained and numerically simulated results of a self-assembly process with an initial misalignment of 500 μm. In these simulations, the contact line is free to move along the substrate surface. While our numerical simulation results capture the damped harmonic oscillation qualitatively, the actual damping rate is substantially underpredicted. Here, the damping rate is defined as the damping ratio of the first full oscillation cycle. This suggests the presence of additional dissipative forces.

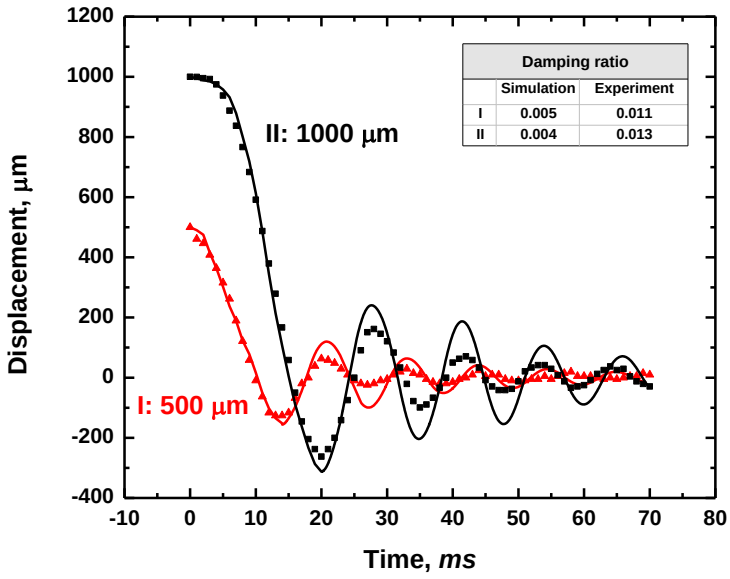

Figure 4.2: Predicted and experimentally determined displacements during a self-assembly process as a function of time. The Experimental data were replicated from an independent early study [92].

Wetting dynamics may be described in terms of the disturbance of absorption equilibrium at the contact line. Its motion is explained by statistical movement of molecular movement at the vicinity of the contact line [93]. A phase field theory introduces a free energy function to describe phenomena such as dynamic contact angle and moving contact line. Previous studies applied this theory to modeling of the dynamics of spreading liquid droplets in sub-millimetric scales [93]–[95]. In these experiments, a droplet (R ~ 0.5 mm) held at the tip of a needle is brought into contact with a dry solid substrate. The droplet is actuated through a micro pump to ensure a very low flow speed. Simulations are then built to replicate the same spreading process while considering the effect of contact line dynamics. These studies found significant impact of so-called line friction, representing microscopic interactions between the liquid and solid surface

at the contact line. A phenomenological parameter called friction factor μ_f was determined by comparing experimentally measured temporal trajectories of spreading liquid droplets with model prediction to represent the line friction force as a function of the contact line velocity [93], [94], [96].

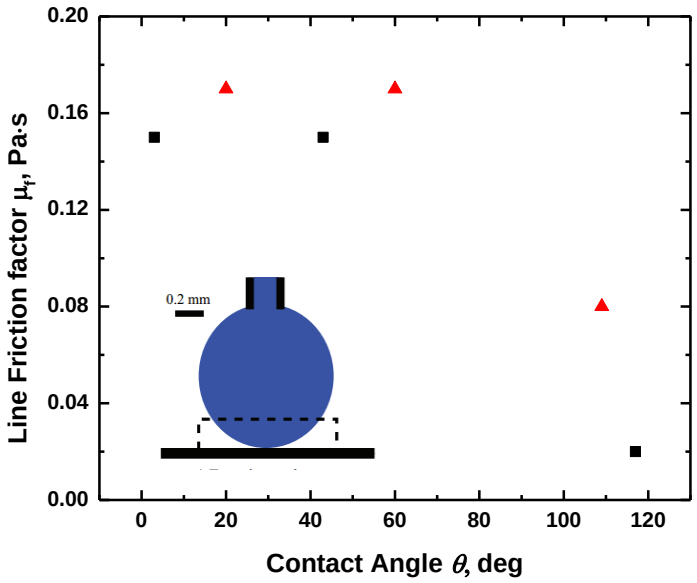

Figure 4.3: The line friction factor as a function of static contact angle of the solid substrate (red triangles are data from an early study [96] and black squares are simulation results replicated from another study [97] using a similar model). Inset image shows the experiment setup where a droplet (R = 0.5 mm) held at the tip of a needle and brought into contact with a dry solid substrate.

Figure 4.3 shows line friction factor μ_f as a function of the static contact angle of the solid surfaces. Generally, as the contact angle increases, the line friction factor decreases. The effect of line friction due to moving contact line is then incorporated into the model, which is modeled as a friction force applied to the solid object as a result of the interaction between the

liquid film and the solid object. The line friction force (with a unit of Nm) is calculated as $f_{line} = \mu_f U_c$, where μ_f is the friction factor and U_c is the lateral velocity of the contact line. At each time step in a typical simulation, the friction force is calculated based on the contact line velocity obtained from solving the fluid dynamics. This line friction force is then applied as a load boundary condition onto the solid object for solving its dynamic motion.

The initial misalignment is an important factor in determining the dynamics of a self-assembly process. For a small initial misalignment, the liquid layer may fully wet the whole solid surface while a large initial offset may not. We first conduct simulations regarding different initial offsets for direct comparison to experimental observations.

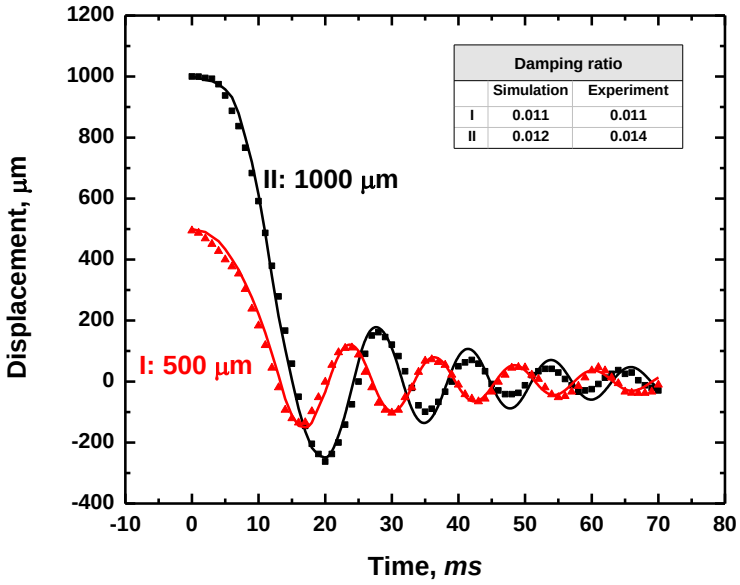

Figure 4.4: Predicted and experimentally determined displacements of the solid substrate as a function of time with an initial misalignment of 500 μm and 1000 μm.

Figure 4.4 compares the experimental and simulation results of a self-assembly process with initial misalignments of 1000 μm and 500 μm. The geometry and surface conditions of the solid substrates are kept the same.

For both initial misalignment values, the trajectory of the solid substrate clearly shows the three sequential dynamic regimes of transient wetting, constant acceleration and underdamped harmonic oscillation. A larger initial misalignment induces a larger acceleration of the solid substrate initially and subsequently a larger displacement to the equilibrium position. As can be observed in Figure 4.4, during the harmonic oscillation regime, larger damping ration is achieved for a larger initial misalignment due to faster contact line motion and thus larger viscous forces. Generally, reasonably good agreement is achieved between simulation and experimental results.

Another important factor in the dynamics of self-assembly process is the contact angle of the solid and substrate surface. The surface conditions significantly contribute to the capillary forces, meniscus geometry and the contact line dynamics. We conduct simulations for two types of substrates and compare with existing experimental results.

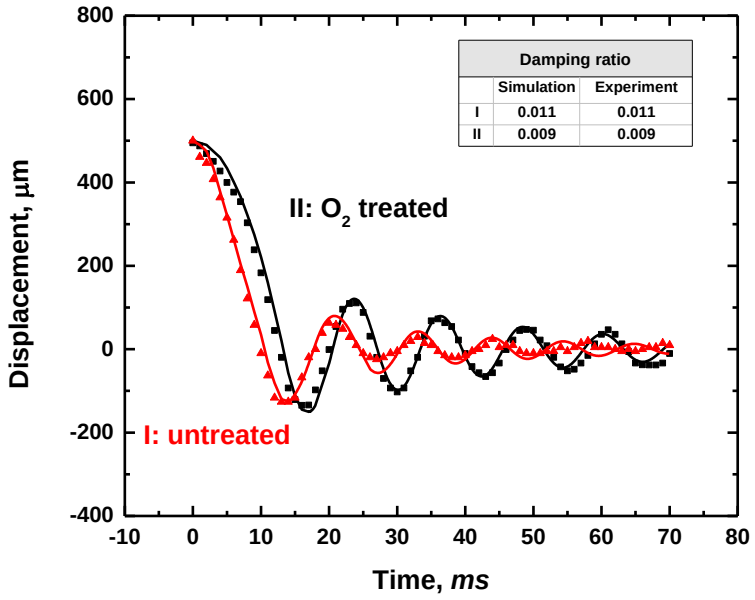

Figure 4.5: Predicted and experimentally determined displacement of the solid substrate as a function of time with untreated and Oxygen treated surfaces.

Figure 4.5 compares the simulation and experimental results of self-assembly processes with an initial misalignment of 500 μm for Oxygen treated and untreated substrates. As shown in Figure 4.5, for oxygen treated substrate with a smaller contact angle, a higher acceleration rate is achieved during the constant acceleration regime and thus a larger displacement from the equilibrium position. In addition, the contact line velocity is smaller, resulting in a smaller dissipative viscous force and thus the damping ratio smaller.

Figure 4.6 shows the predicted trajectories of the contact line motion as a function of time for three different experimental conditions. In this plot, a negative value of contact line motion means the contact line moves beyond the target binding boundary while a positive value means

the contact line moves within the target binding boundary. As shown in Fig. 6, for a larger initial misalignment, the contact line moves farer away from the binding site boundary and meanwhile a larger contact line velocity, resulting in a larger line friction force. For an untreated substrate, the contact line displacement is larger than an oxygen treated surface with the same initial misalignment due to a larger contact angle. Each trajectory of the contact line motion closely represents a significantly damped harmonic oscillation, where the contact line displacement from the binding site boundary rapidly reduces to zero in a few cycles. These predictions from Fig. 4.6 accords to the experimental observations in Fig. 4.4 and Fig. 4.5.

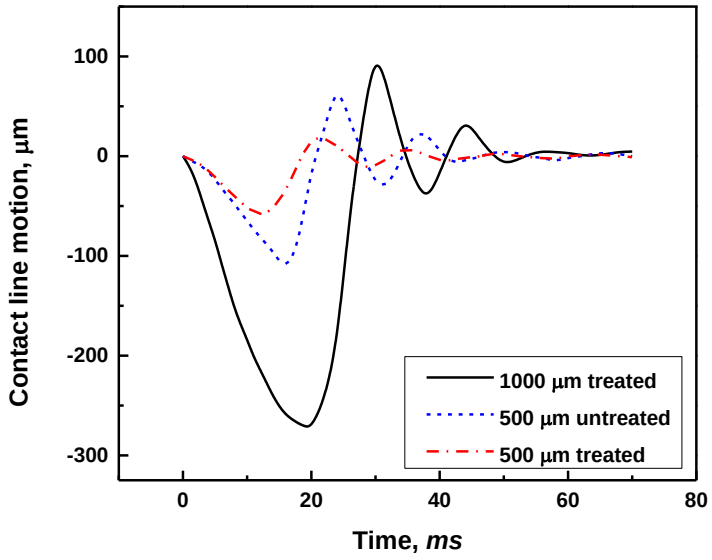

Figure 4.6: Predicted contact line motion as a function of time with different initial misalignments and surfaces conditions of the substrate.

Figure 4.7 shows the predicted viscous force and line friction force per unit length as a function of time for different combinations of initial misalignment and substrate surface

conditions. For a larger initial misalignment, the contact line friction force is larger while the viscous force is almost the same (Fig. 4.7a). Similarly, for an untreated substrate, the contact line friction force is larger while the viscous force is almost the same (Fig. 4.7b). For each trajectory in Fig. 4.7, the line friction force rapidly decreases while the viscous force reduces much slowly. In addition, the line friction force dominates over the viscous forces during the first a few oscillation cycles and become comparable to viscous forces when the solid object is about to reach its rest position. These predictions accords to the previous experimental observations in Fig. 4.4 and Fig. 4.5.

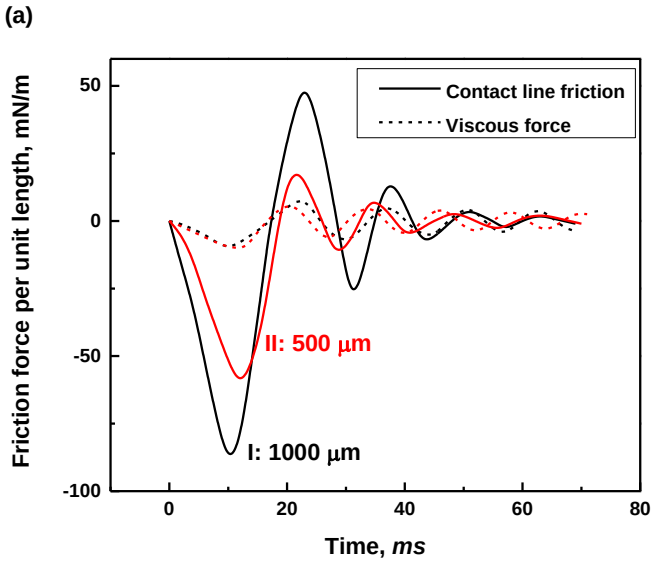

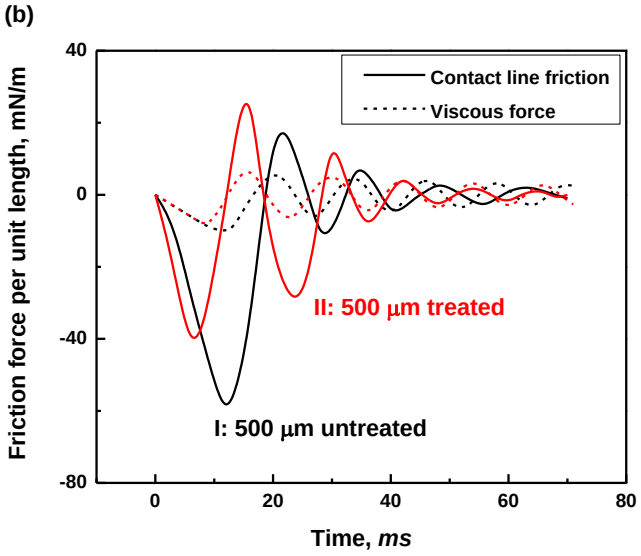

Figure 7: Predicted viscous force and line friction force per unit length as a function of time for (a) 1000 μm and 500 μm initial misalignment; (b) untreated and oxygen treated substrates.

4.3.2 Effects of initial displacement, contact angle and liquid film thickness on capillary self-assembly

With the established coupled model, we perform series of simulations to understand the dynamics of the uniaxial self-assembly for different parameters of the system.

The initial misalignment of the solid object is an important factor to the self-assembly process. While maintaining other parameters such as liquid film thickness, substrate geometry and contact angles constant, simulations are performed for different initial offset ranging from 50 to 500 μm.

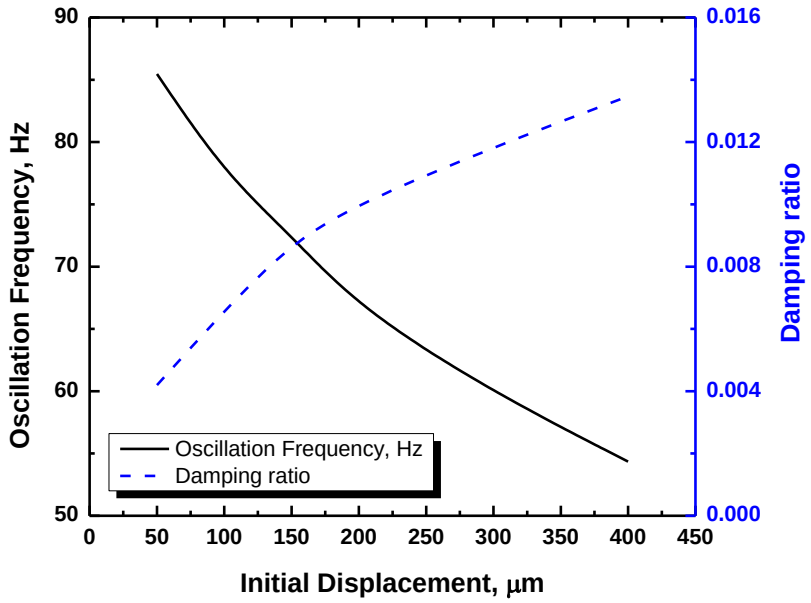

Figure 4.6: Predicted determined oscillation frequency and damping ratio of the solid substrate in its damped harmonic oscillation regime as a function of the initial offset.

Figure 4.6 shows the oscillation frequency and damping ratio of the harmonic oscillation regime in a self-assembly process as a function of initial misalignment. As the initial offset increases, the solid substrate responses slower (the oscillation frequency decreases). The damping ratio, however, increases with the initial misalignment. This can be explained by the fact that the contact line velocity increases as the restoring forces increases for a larger displacement from the equilibrium position.

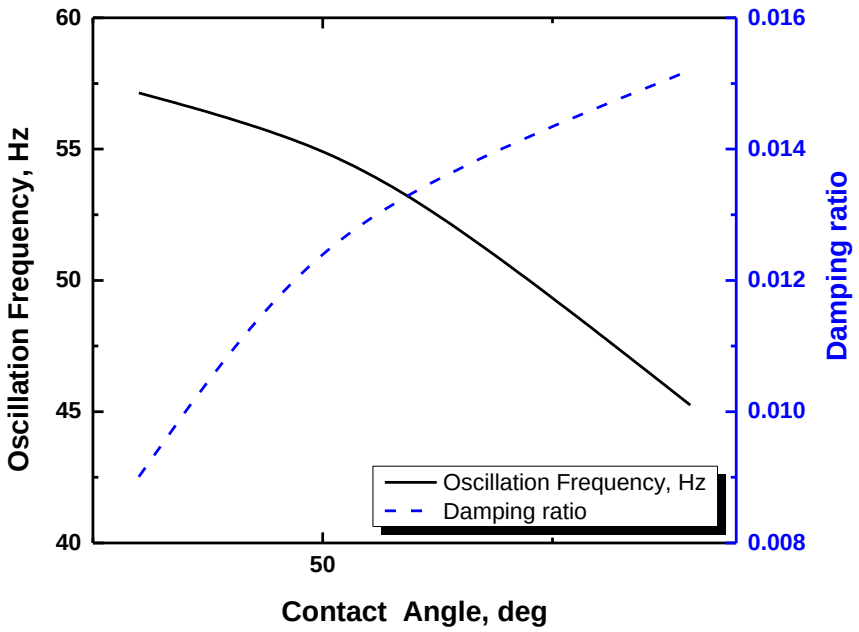

Figure 4.7: Predicted determined oscillation frequency and damping ratio of the solid substrate in its damped harmonic oscillation regime as a function of the static contact angle.

Simulations are also conducted to demonstrate the effect of substrate static contact angle on the dynamic of self-assembly process especially the harmonic oscillation regime. Figure 4.7 shows the oscillation frequency and damping ratio of the harmonic oscillation regime in a self-assembly process as a function of the static contact angle. As the static contact angle increases, the solid substrate responses slower (the oscillation frequency decreases). Meanwhile, the damping ratio increases due to the increased contact line velocity.

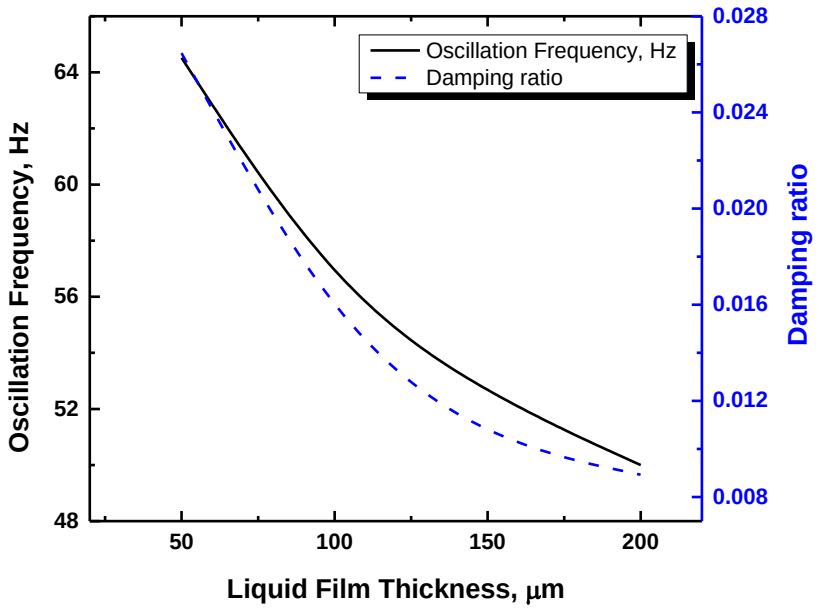

Figure 4.8: Predicted determined oscillation frequency and damping ratio of the solid substrate in its damped harmonic oscillation regime as a function of the liquid film thickness.

The thickness of the supporting liquid film not only affects the stability of the solid substrate, but also has effects on the dynamics of the self-assembly process. Figure 4.8 shows the oscillation frequency and damping ratio of the harmonic oscillation regime in a self-assembly process as a function of the liquid film thickness. As the static contact angle increases, the solid substrate responses slower (the oscillation frequency decreases). As the liquid film gets thicker and thicker, the disturbing effect from the motion of the solid substrate on the contact line decreases, reducing the contact line velocity and thus the damping ration decreases.

4.4 Summary

In this chapter, the dynamics of capillary-driven self-alignment processes is investigated using numerical simulations. The model directly couples the fluid dynamics of the supporting

liquid bridge and the motion of the suspended solid object while directly tracking the deformation of liquid menisci and motion of contact lines. Model predictions accounting for only the viscous shear stress associated with mesoscale liquid motions underpredict damping ratios. We identify an extra dissipative force arising from the motion of triple-phase contact line as a possible explanation for the discrepancy. Model predictions based on an independently determined value of the line friction coefficient capture reasonable well the experimentally observed temporal trajectories of the suspended solid object.

Chapter 5

Mechanical Design and Modeling of Deployable and Conformal Devices for Minimally Invasive Brain Functional Monitoring

A design concept for a deployable planar microdevice and the modeling and experimental validation of its mechanical behavior is present in this chapter. The device consists of foldable membranes that are suspended between flexible stems and actuated by push-pull wires. Such a deployable device can be introduced into a region of interest in its compact "collapsed" state and then deployed to conformally cover a large two-dimensional surface area for minimally invasive biomedical operations and other engineering applications.

We develop and experimentally validate theoretical models based on the energy minimization approach to examine the conformality and figures of merit of the device. The experimental results obtained using model contact surfaces agree well with the prediction and quantitatively highlight the importance of the membrane bending modulus in controlling surface conformality. The present study establishes an early foundation for the mechanical design of this and related deployable planar microdevice concepts.

5.1 Introduction

Deployable devices that can be introduced into a region of interest in their compact collapsed states and then deployed to cover large volumes or surface areas are of great interest to various engineering and biomedical applications [8]–[12]. These include deployable sensor networks for structural health monitoring or robotics applications, compact launch-volume structures for space applications and stents/catheters/optoelectrode arrays for minimally invasive diagnosis and treatments of cardiovascular and neuronal diseases.

Existing deployable devices and tools, in particular those employed for minimally invasive bio-medical procedures, are mostly limited to mechanical functionalities. They also target limited geometries, as they very often rely on inflatable balloons for deployment [13], [14]. Adapting these device designs for planar configurations while at the same time providing the ability to incorporate electrical, optoelectronic and other sensing and actuation capabilities are highly desirable to further expand the usage of deployable devices and to facilitate the exploration of novel applications.

A conceptual design of our deployable planar device is shown in Figure 5.1. Foldable thin-film membranes, which may incorporate 2D electrode arrays or other electronic or optical components, as demonstrated in many recent studies on flexible electronics [98], are suspended between semi-flexible stems via embedded wire guides. The device may be introduced through a small burr hole in its compact collapsed state (the membranes fully folded). The push-pull wires then allow the membranes to be deployed *in situ* along a gap and cover a large surface area.

The membranes must be sufficiently flexible to conformally contact typical engineering surfaces or tissues that contain topographical features. Previous studies reported mechanical modeling of the behavior of flexible conformal membranes. Kim *et al.* [99] predicted the tensile and compressive strains of epidermal electrodes that may be conformally attached to human skin. Other studies examined the deformation of thin membranes under elastocapillary effects. An analytic model reported in [100], for example, describes the folding and reopening processes of capillary-driven origami structures. In this and related models, the behavior of thin membranes subjected to capillary forces are studied by considering the mutual interaction between the surface and elastic energies [101].

We extend these past efforts and develop analytic models to investigate the conformality of flexible membranes as they contact surfaces and experimentally validate the models. We note that our goal for this analytic modeling is to help establish a basic understanding of the mechanics involved using simplified test cases rather than to examine complex geometric situations of a specific application.

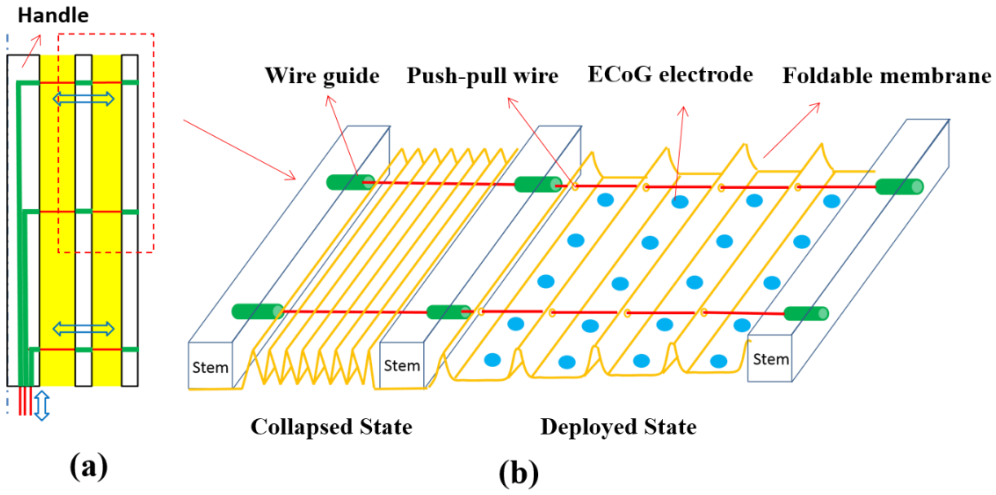

Figure 5.1: (a) Conceptual design of the deployable ECoG electrode array. Foldable membranes incorporating the electrodes are suspended between stems via push-pull wires. (b) Zoomed view of the device in its collapsed and deployed state.

5.2 Mechanical models

To help quantify the conformality of the membranes, we define the bending angle θ_l as the angle between a membrane and a push-pull control wire (Figure 5.2). Our basic approach is to find this bending angle as a function of the relevant physical and geometric parameters of the membrane by identifying a minimum energy state of the membrane when in contact with a model cortical surface.

We consider a single membrane fold and approximate it as linearly interconnected segments, each of a uniform radius of curvature. The total energy E_t of the fold is the sum of its elastic strain energy E_e and the interfacial energy E_s (in contact with the cortical surface via an interfacial fluid): $E_t = E_e + E_s$. The equilibrium bending angle is considered the one that minimizes E_t under a given geometric constraint.

The elastic strain energy per unit area e of a membrane segment that bent to a radius of curvature R can be written as $e = B/2R^2$, where $B = Eh^3 / [12\ (1-\nu^2)]$ is the bending modulus of the membrane. Here, E is the Young's modulus, ν is the Poisson's ratio, and h is the thickness of the membrane [102]–[104]. The present analytic model considers only 2D deformation of the membrane and all the energy terms are considered per unit width (into the page) of the membrane. The total elastic strain energy E_e can be obtained as the sum of the strain energies of all the segments:

$$E_e = \sum_{i=1}^{n} e_i A_i \quad (5.1)$$

where A_i is the area of the membrane segment with a radius of curvature R_i.

The surface/interfacial energy E_s can be generally expressed as $E_s = \gamma_{sg}A_{sg} + \gamma_{lg}A_{lg} + \gamma_{sl}A_{sl}$ where γ's are the surface tension coefficients and A's are the corresponding areas of solid-gas, liquid-gas, and solid-liquid interfaces.

We consider two different surface topographies in the present study: 1) a featureless flat surface 2) a flat surface incorporating a sulcus (or valley). The former emulates a cortical surface of typical lower-order animals and the latter emulates gyrii in humans or apes with radii of curvature much greater than the length of the single membrane fold.

5.2.1 Flat featureless surface

Based on our experimental observations, we approximately represent a single fold of the membrane using seven segments: one flat segment of length l_2, two sets of two bent segments with radii of curvature, R_1 and R_2, respectively, and two unbent segments of length l_1 (Figure 5.2). These geometric parameters of the membrane are inter-related:

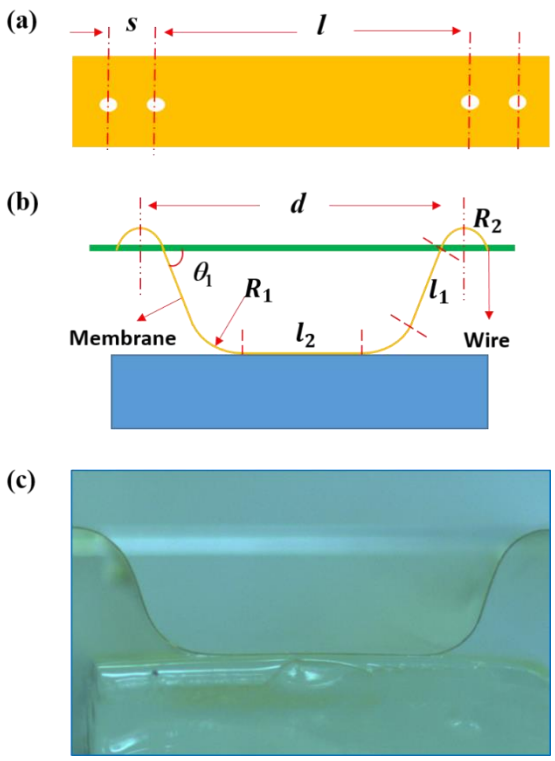

Figure 5.2: Geometric model of the membrane in contact with a featureless flat surface: (a) top view of membrane in complete released state; (b) side view. (c) Optical image of the membrane in side view.

$$2l_1 + 2R_1\theta_1 + l_2 = l \quad (5.2)$$

$$2l_1\cos\theta_1 + 2R_1\sin\theta_1 + 2R_2\sin\theta_1 + l_2 = d \quad (5.3)$$

$$2R_2\theta_1 = s \quad (5.4)$$

The total energy is next expressed as a function of the bending angle θ_1. After algebraic manipulation, we write

$$E_t = B(\frac{\theta_1}{R_1} + \frac{2\theta_1^2}{s}) + \gamma_{sg}l - (\gamma_{sg} + \gamma_{lg} - \gamma_{sl})l_2 + \gamma_{lg}d \quad (5.5)$$

where

$$l_2 = \frac{l\theta_1 \cos\theta_1 - d\theta_1 + s\sin\theta_1 - 2R_1\theta_1(\cos\theta_1 - \sin\theta_1)}{\theta_1(\cos\theta_1 - 1)} \qquad (5.6)$$

5.2.2 Substrate incorporating a sulcus

We next consider a flat surface with a sulcus illustrated in Figure 5.3. The sulcus is located in the middle of the flat substrate and modeled using two circular arcs of radius R_s. The membrane is assumed to bend with a constant radius of curvature R_3 over the sulcus. A second bending angle θ_2 is used to quantify the ability of the membrane to conformally follow the contour of the sulcus.

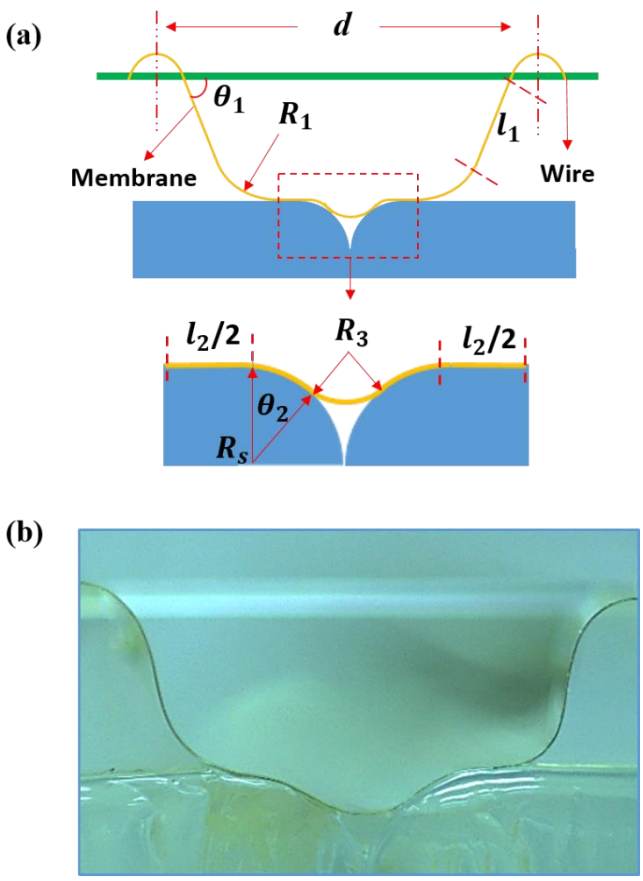

Figure 5.3: (a) Geometric model of the membrane in contact with a featureless flat surface in side view; (b) Optical image of the membrane in side view.

Similar to our model for the featureless flat substrate, we first relate the geometric parameters of the bent membrane:

$$2l_1 + 2R_1\theta_1 + l_2 + 2(R_3 + R_s)\theta_2 = l \quad (5.7)$$

$$2l_1\cos\theta_1 + 2R_1\sin\theta_1 + 2R_2\sin\theta_1 + l_2 + 2R_s = d \quad (5.8)$$

$$(R_3 + R_s)\sin\theta_2 = R_s \quad (5.9)$$

$$2R_2\theta_1 = s \quad (5.10)$$

The total energy of the membrane is then written as

$$E_t = B(\frac{\theta_1}{R_1} + \frac{2\theta_1^2}{s} + \frac{\theta_2}{R_s} + \frac{\theta_2}{R_v}) + \gamma_{sg} l - (\gamma_{sg} + \gamma_{\mathrm{lg}} - \gamma_{sl})(l_2 + 2R_v\theta_2) + \gamma_{\mathrm{lg}} d \qquad (5.11)$$

Where

$$l_2 = \frac{l\theta_1 \cos\theta_1 \sin\theta_2 - d\theta_1 \sin\theta_2 + s \sin\theta_1 \sin\theta_2 - 2R_1\theta_1 \sin\theta_2(\theta_1 \cos\theta_1 - \sin\theta_1) + 2R_s\theta_1(\theta_2 \cos\theta_1 - \sin\theta_2)}{\theta_1(\cos\theta_1 - 1)\sin\theta_2}$$

(5.12)

5.2.3 Non-dimensionalization

To help gain further physical insights and "generalize" our models, we recast the equations for identifying the minimum energy states in their dimensionless forms.

We define an elastocapillary length [15] L_{EC} as $L_{\mathrm{EC}} = (B/\gamma)^{1/2}$ where B is once again the bending modulus of the membrane $B = Eh^3/[12\ (1-\nu^2)]$ and $\gamma \approx \gamma_{\mathrm{sg}} + \gamma_{\mathrm{lg}} - \gamma_{\mathrm{sl}}$. A membrane longer than this characteristic length will be significantly deflected by the surface tension force.

Using the featureless flat surface as an example, we write the first order derivatives of the total energy in their dimensional form and set them equal to zero:

$$\frac{\partial E_t}{\partial \theta_1} = B(\frac{1}{R_1} + \frac{4\theta_1}{s}) - (\gamma_{sg} + \gamma_{\mathrm{lg}} - \gamma_{sl})\frac{\partial l_2}{\partial \theta_1} = 0 \quad (5.13)$$

$$\frac{\partial E_t}{\partial R_1} = B(-\frac{1}{R_1^2}) - (\gamma_{sg} + \gamma_{\mathrm{lg}} - \gamma_{sl})\frac{\partial l_2}{\partial R_1} = 0 \quad (5.14)$$

After non-dimensionalizing all the relevant geometric parameters (R_1, s, l, d) using L_{EC}, we obtain

$$\frac{1}{\tilde{R}_1}+\frac{4\theta_1}{\tilde{s}}-\frac{\sin\theta_1}{(\cos\theta_1-1)^2}[2\tilde{R}_1(\theta_1-\sin\theta_1)+\tilde{d}-\tilde{l}+\frac{(\theta_1\cos\theta_1-\sin\theta_1)}{\theta_1^2}\tilde{s}]=0 \quad (5.15)$$

$$\frac{\theta_1}{\tilde{R}_1^2}-\frac{2(\theta_1\cos\theta_1-\sin\theta_1)}{\cos\theta_1-1}=0 \quad (5.16)$$

We further define two dimensionless parameters that characterize the extent of membrane deployment and the dimension of the sulcus: deployment factor $D_f = (d - l)/s$ and dimensionless sulcus radius $S_f = 2R_s/d$. The deployment factor governs the lower bound θ_{min} of the bending angle ($\theta > \theta_{min}$).

5.3 Experiments

To help validate our models, we constructed single folds of membranes of a range of thicknesses (3.8 ~ 12.7 μm) and measured respective bending angles on two different types of model surfaces. We chose polyimide as our membrane material as it has been widely used as substrates to construct thin film ECoG electrodes [104]–[107]. The polyimide has a Young's modulus of 2.3 GPa and Poisson's ration of 0.34 and surface tension of γ_{sl} = 0.042 N/m, γ_{lg} = 0.073 N/m, and a contact angle of 70° with water.

A liquid solution of polyimide (PI-2545, HD MicroSystems™) was first spin coated on a glass side and cured at 250 ℃ for 0.5 hour and again at 350 ℃ for 0.5 hour. The cured

membrane was then peeled off from the glass side. The membrane was attached to two glass slides that served as rigid mechanical supports. The membranes were suspended using wires (0.20 mm in diameter, Como Nylon filament) inserted through mechanically punctured holes.

Model cortical surfaces were prepared using Agar gels to simulate the mechanical properties of brain tissues [108]. An Agar solution (0.5g / 100ml DI water) was first heated at 200℃ until it boiled and then cooled down to form thick (~ 3 mm) blocks of gel. Some of the blocks were formed on a mold to create sulci.

The experimental setup is shown in Fig. 5.4. The two glass slides holding each membrane were mounted on two translational stages so that we could adjust the deployment distance *d* (see Figure 5.2). At the beginning of each experiment, an Agar block was gradually lifted up using a vertical translation stage until it made a contact with the membrane such that the membrane suspended free from the wire. A digital camera captured the images of the membrane, which were then analyzed to determine the bending angles. For each membrane, experiments were repeated while varying the deployment distance *d*.

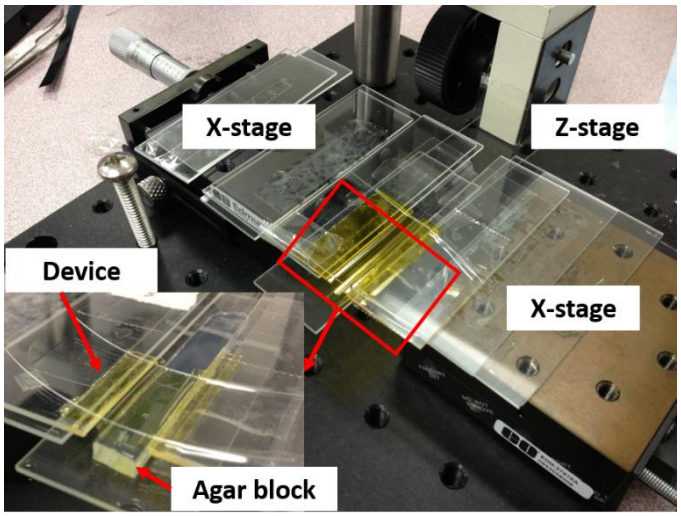

Figure 5.4: Experimental setup of bending angle measurements with zoomed view of deployable device in contact with Agar block.

5.4 Results and discussions

5.4.1 Featureless flat surface

Figure 5.5 shows representative captured images of the polyimide membranes under different deployment conditions on the featureless flat surfaces. The bending angle of the membrane after making contact with the Agar surface is determined by the dimensions of the device (*l*, *s*, *d*). As expected, for a given hole spacing *s* = 1.5 mm, the bending angle is larger for larger deployment distances (5a vs 5b and 5c vs 5d). A larger membrane thickness leads to a smaller bending angle (5a vs 5c and 5b vs 5d) due to larger bending modulus *B*.

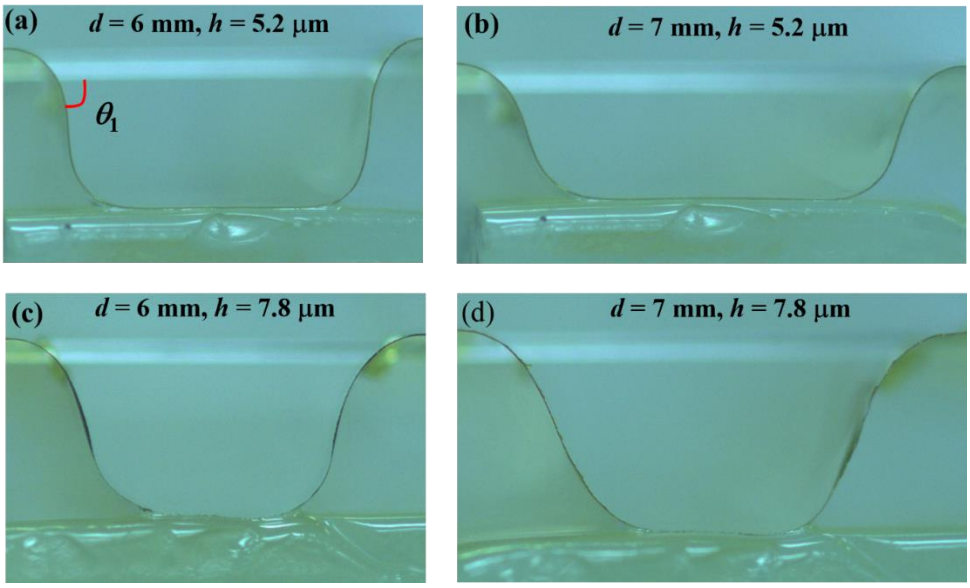

Figure 5.5: Optical images of membrane shapes under different deployment distances and thicknesses for featureless flat surface.

Figure 5.6 shows the predicted and experimentally observed bending angles for three different values of the deployment factor $D_f = (d - l)/s$ as a function of the normalized membrane length l/L_{EC}. The two results agree well with each other.

Under the same substrate surface conditions, the equilibrium state of membrane is merely determined by membrane material, dimensions and deployment. For a given D_f, the bending angle θ starts at the geometrically determined initial value θ_{min} and then increases as the normalized membrane length l/L_{EC} increases (or as the thickness of the membrane decreases). Note that, when the membrane length l (over a single fold) is fixed, the normalized membrane length is inversely proportional to L_{EC} and hence $h^{3/2}$. As mentioned previously, the elastocapillary length L_{EC} is the characteristic length of a membrane that measures its resistance

to bend in response to surface tension forces. A membrane with length l much larger than L_{EC} is strongly deflected by surface tension forces and thus gives rise to large bending angles. A shorter or thicker membrane (l smaller than L_{EC}) in contrast will not be significantly bent by surface tension forces.

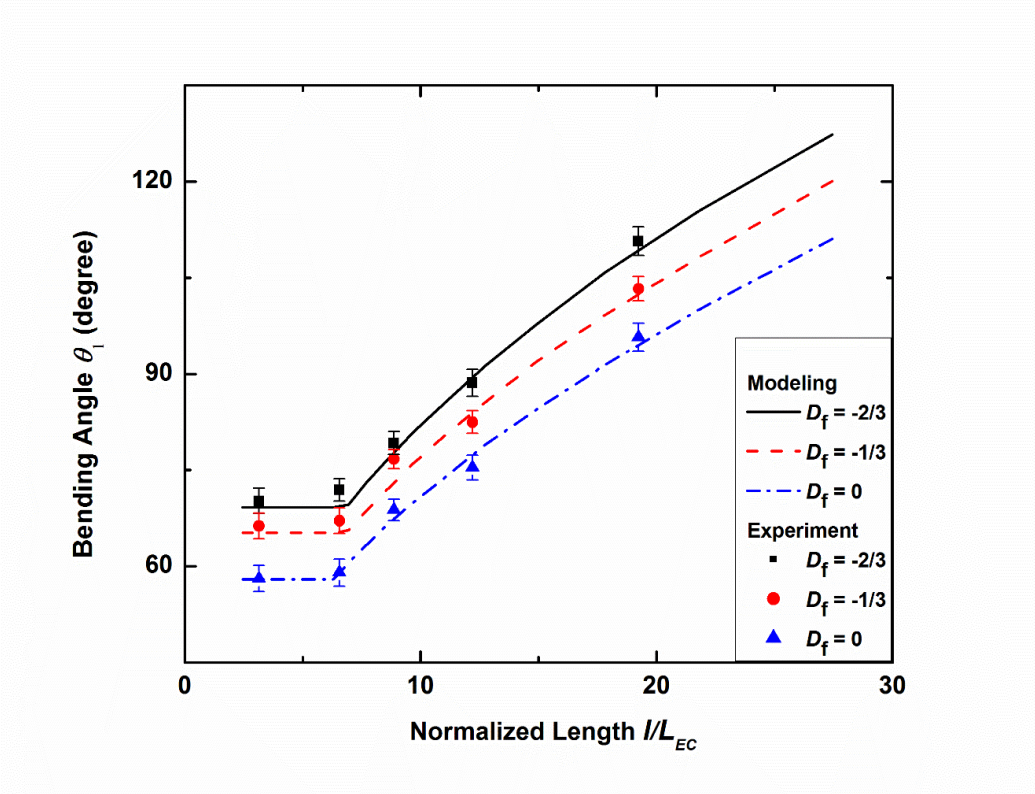

Figure 5.6: Modeling and experimental results of the bending angle on the featureless flat surfaces as a function of the normalized membrane length for different deployment factors.

The effect of normalized membrane length on bending behaviors of membrane is discussed above. Besides this, the way the membrane is deployed contributes to the final state of the membrane after contacting the surface. For a given normalized membrane length, higher deployment factors result in higher bending angles (Fig. 5.7). From the condition $0 < d < l + s$,

the possible values of D_f are within the range of (-l/s, 1). The deployment factor D_f governs the initial bending angle of the membrane before it makes any contact with the model cortical surface. Larger deployment factors result in larger initial bending angles. In fact, for a given membrane length l and a hole spacing s, a smaller deployment distance d leads to a larger deployment factor D_f and hence a larger initial bending angle. Once again, the experimental results agree well with the modeling results.

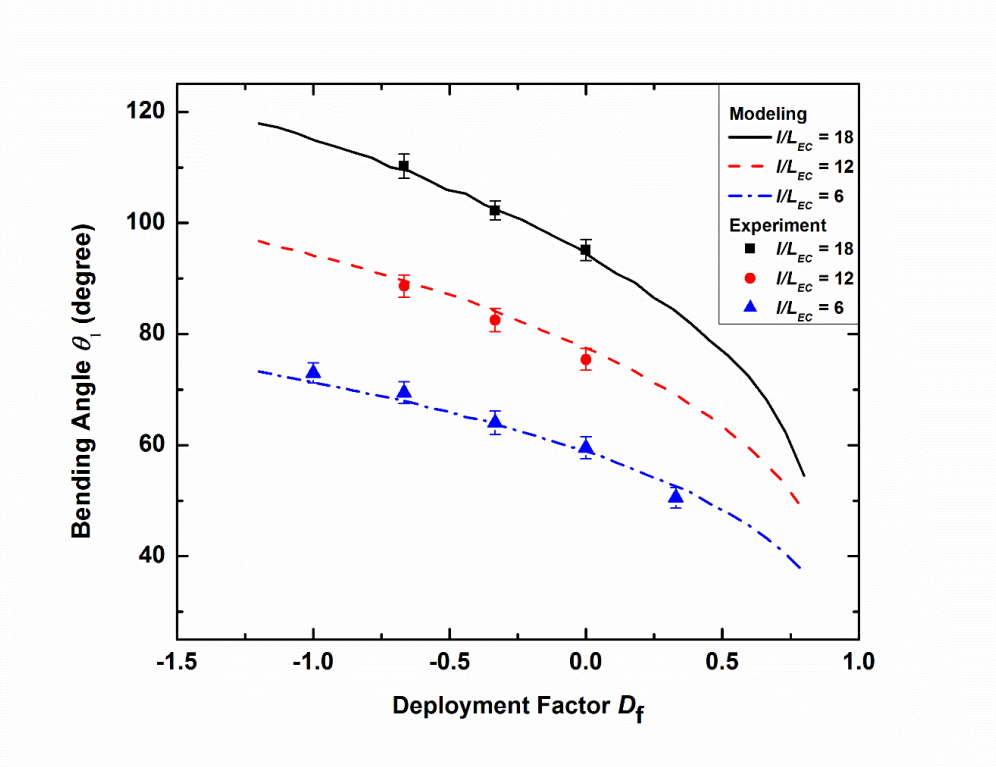

Figure 5.7: Modeling and experimental results of the bending angle as a function of deployment factor.

The bending angle helps quantify the conformality of the membrane contacting a cortical surface. Another important design consideration is how efficiently the membrane is utilized to achieve a large spatial coverage. We define two additional parameters to help quantify this

characteristic of our deployable membrane. 1) The fraction of the membrane area that makes contact with the cortical surface: membrane utilization ratio $r_u = (l_2 + 2R_s\theta_2)/l$ and 2) the fraction of the deployment area projection that is available for electrode placement: membrane coverage ratio $r_c = (l_2 + 2R_s\theta_2)/d$. Recall that l_2 is the length of the flat membrane segment in contact with the model cortical surface. For the featureless flat surface without a sulci, the same definitions is used with $R_s = 0$.

Figure 5.7 shows the calculated membrane utilization and coverage ratios as a function of the normalized membrane length for different values of the deployment factor D_f. For a given deployment factor, as the normalized length increases, the membrane is more readily deformed to make larger contact areas, leading to enhanced coverage and utilization ratios. The quantitative results allow selection of an optimal membrane thickness to achieve acceptable coverage or utilization ratios without severely compromising the mechanical robustness of the membrane.

The deployment factor also affects the coverage and utilization ratios but in different ways. As the deployment factor increases, the utilization ratio monotonically increases. The coverage ratio, in contrast, decreases with the increasing deployment factor when the normalized length is large ($l/L_{EC} > 10$ in Fig. 5.8a). When the normalized length is small ($l/L_{EC} < 5$ in Fig. 5.8a), the coverage ratio increases with the increasing deployment factor. This can be understood from the asymmetric behavior of the coverage ratio depending on whether the bending angle θ_1 is smaller or larger than 90 °. As schematically illustrated in Figure 9, for given values of l and s, the surface contact length l_2 increases with the deployment distance d when $\theta_1 < 90$ °whereas l_2 decreases with d when $\theta_1 > 90$ °.

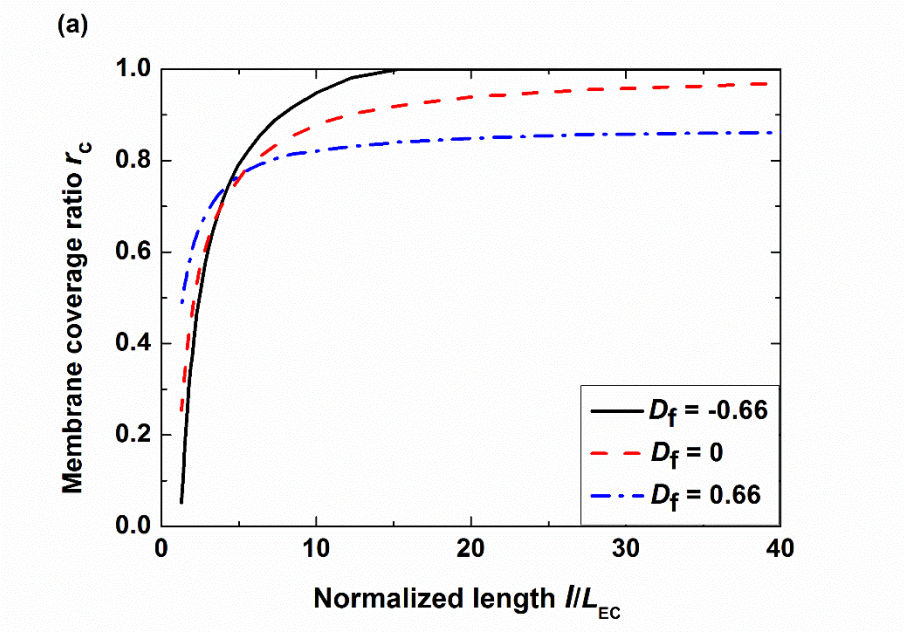

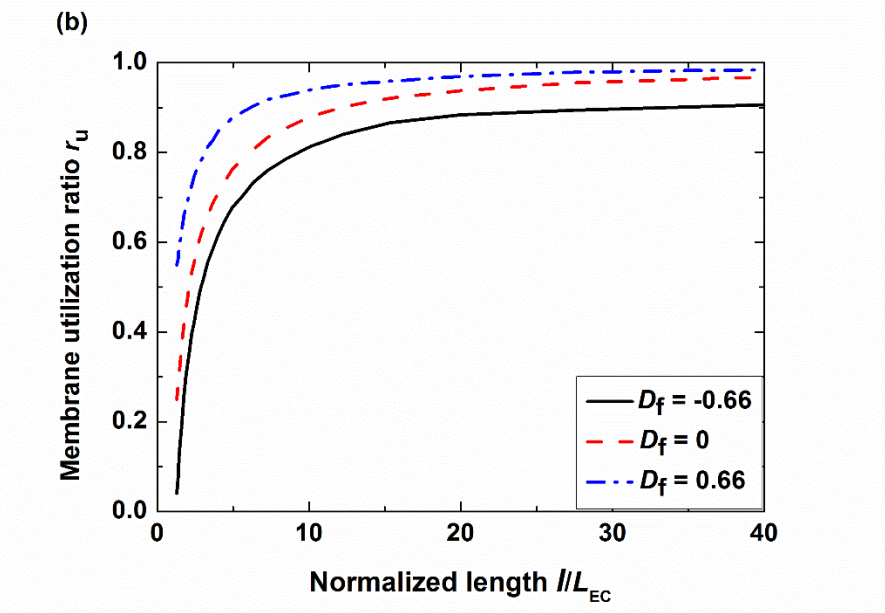

Figure 5.8: The predicted membrane coverage and utilization ratios as a function of the normalized length.

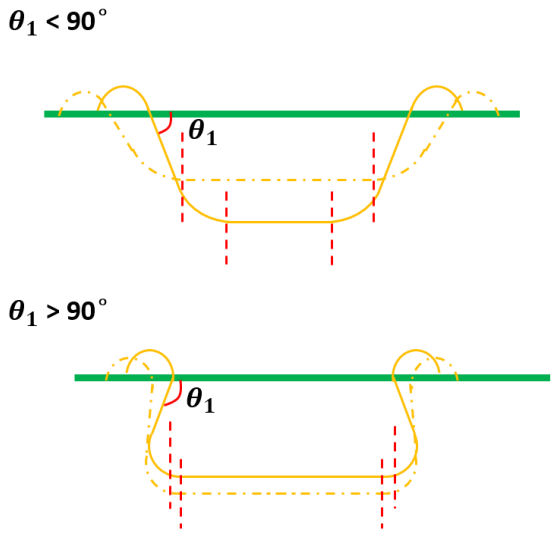

Figure 5.9: Schematic illustration of changes in the membrane bending behavior for different deployment factors when $\theta_1 < 90°$ and $\theta_1 > 90°$.

5.4.2 Flat surface incorporating a sulcus

For the model cortical surfaces with a single sulcus, Fig. 5.10 shows representative captured images of the polyimide membranes. For a given deployment factor, as the thickness of the membrane increases (and hence as the normalized length decreases), the two bending angles θ_1 and θ_2 decrease.

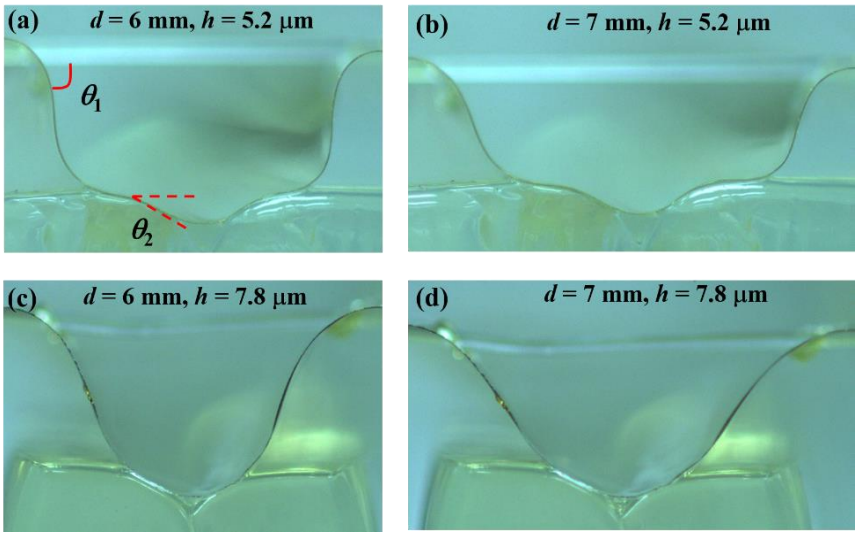

Figure 5.10: Optical images of the membranes under different deployment factors and normalized lengths for the surface incorporating single sulcus.

Figures 5.11a and 5.11b show the predicted and measured bending angles θ_1 and θ_2 as a function of the normalized membrane length. The general qualitative trend for θ_1 is similar to that of the featureless flat surfaces. Larger normalized membrane lengths lead to larger bending angles and therefore higher conformality. For the given set of the deployment factors and the radii of curvature of the sulci examined here, critical normalized lengths of the order of 20 and greater are necessary to achieve good conformality over the sulci.

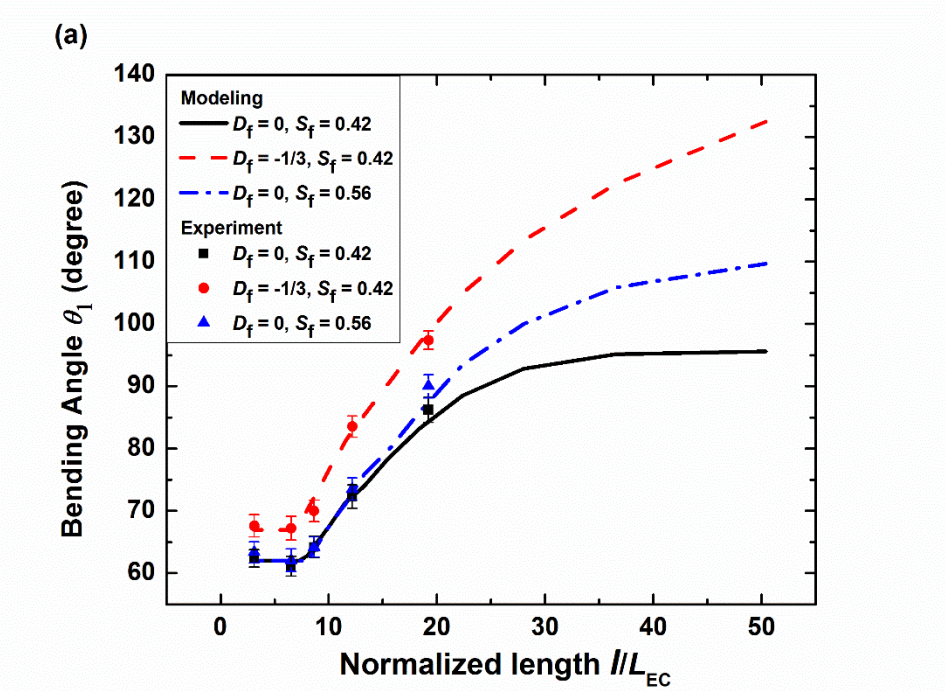
(a)
Modeling
D_f = 0, S_f = 0.42
D_f = -1/3, S_f = 0.42
D_f = 0, S_f = 0.56
Experiment
D_f = 0, S_f = 0.42
D_f = -1/3, S_f = 0.42
D_f = 0, S_f = 0.56
Bending Angle θ_1 (degree)
Normalized length l/L_{EC}

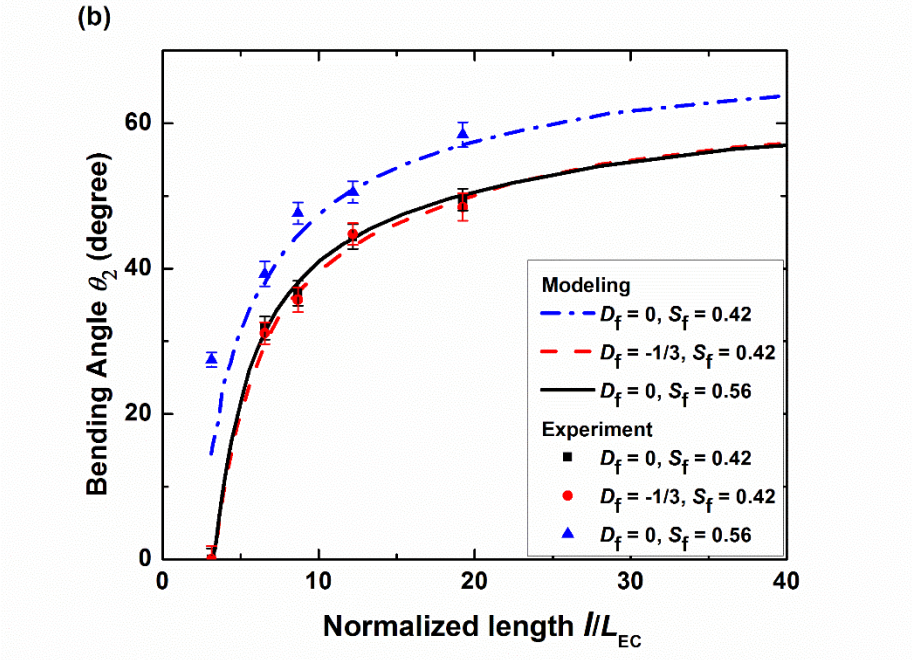
(b)
Modeling
D_f = 0, S_f = 0.42
D_f = -1/3, S_f = 0.42
D_f = 0, S_f = 0.56
Experiment
D_f = 0, S_f = 0.42
D_f = -1/3, S_f = 0.42
D_f = 0, S_f = 0.56
Bending Angle θ_2 (degree)
Normalized length l/L_{EC}

Figure 5.11: Modeling and experimental results of bending angle θ_1 (a) and θ_2 (b) as a function of normalized length for surface incorporating a sulcus.

The results of three different cases are shown in Fig. 11: I) $D_f = 0$, $S_f = 0.42$; II) $D_f = -1/3$, $S_f = 0.42$; III) $D_f = 0$, $S_f = 0.56$. Figure 5.12 shows the predicted and measured bending angles θ_1 and θ_2 as a function of the deployment factor when $S_f = 0.42$. For a normalized sulcus radius of curvature S_f of 0.42, the deployment factor has a significant effect on the top bending angle θ_1 but little effect on the bottom bending angle θ_2 (Case I and II). However, for a given deployment factor $D_f = 0$, θ_2 is a strong function of S_f whereas θ_1 is only a weak function of S_f. (Case I and III). The presence of the sulcus reduces the length of the top membrane segments (adjacent to the wires) and thereby decreases the top bending angle when compared with the membrane on the featureless flat surfaces. When the spatial extent of the sulcus is sufficiently small, the top membrane segments are separated by the flat segments from the bottom segments covering the sulcus. Therefore, the geometric details of the sulcus do not significantly influence the top bending angle. In contrast, θ_2 is dependent on the sulcus dimension, increasing with S_f.

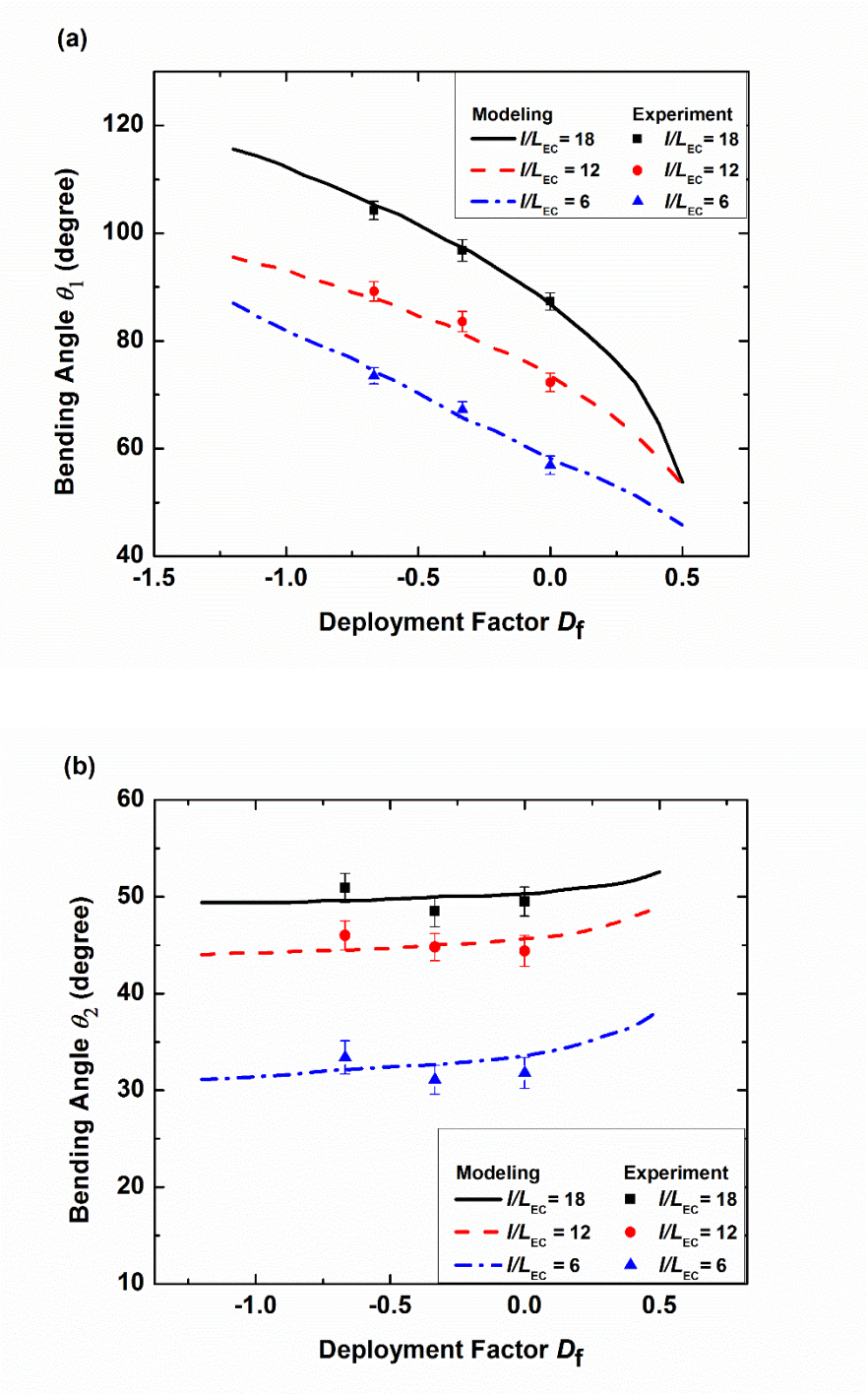

Figure 5.12: Modeling and experimental results of bending angles θ_1 (a) and θ_2 (b) as a function of deployment factor.

Figure 5.13a and b show the two bending angles as a function of the normalized sulcus radius of curvature S_f. As the normalized sulcus radius S_f increases, the bending angle θ_1 decreases whereas bending angle θ_2 increases. A larger radius of sulcus induces a longer membrane bent in the sulcus and thus a larger bending angle θ_2. Since the total membrane length is fixed and the increasing length of membrane bent in the sulcus, the effective membrane length is reduced and thus the bending angle θ_1 is decreased.

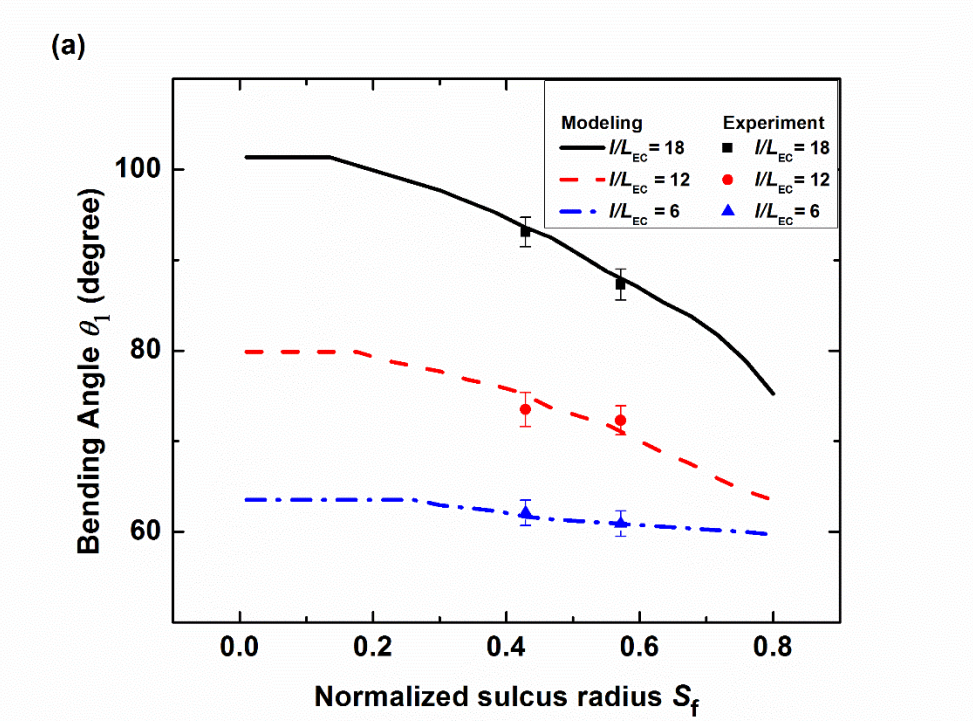

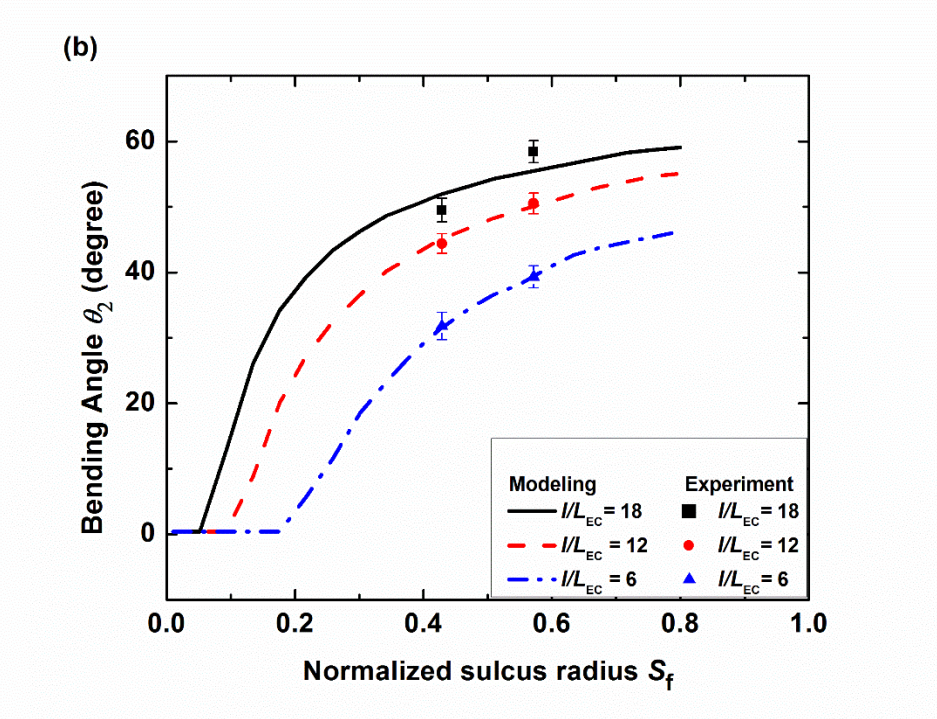

Figure 5.13: Modeling and experimental results of bending angles θ_1 (a) and θ_2 (b) as a function of sulcus length factor.

Figure 5.14 shows the calculated membrane utilization and coverage ratios as a function of the normalized membrane length for different values of the deployment factor D_f. For a given deployment factor, as the normalized length increases, the membrane is more readily deformed and thus has a larger coverage and utilization ratios. However, the presence of sulcus reduces the effective length of the membrane comparing to a featureless surface. Therefore, the membrane is less deformed and has smaller coverage and utilization ratios than a surface without a sulcus. Similar to a featureless surface, the deployment factor also affects the coverage and utilization ratios in different ways. As the deployment factor increases, the utilization ratio monotonically increases. The coverage ratio, in contrast, decreases with the increasing

deployment factor when the normalized length is large ($l/L_{EC} > 7$ in Fig. 5.14a). However, when the normalized length is small ($l/L_{EC} < 4$ in Fig. 5.14a), the coverage ratio increases with the increasing deployment factor. This can be explained by the asymmetric behavior of the coverage ratio between when the bending angle $\theta_1 < 90°$ and when $\theta_1 > 90°$. The surface contact length increases with the deployment distance d when $\theta_1 < 90°$ whereas it decreases with d when $\theta_1 > 90°$ for given values of l and s.

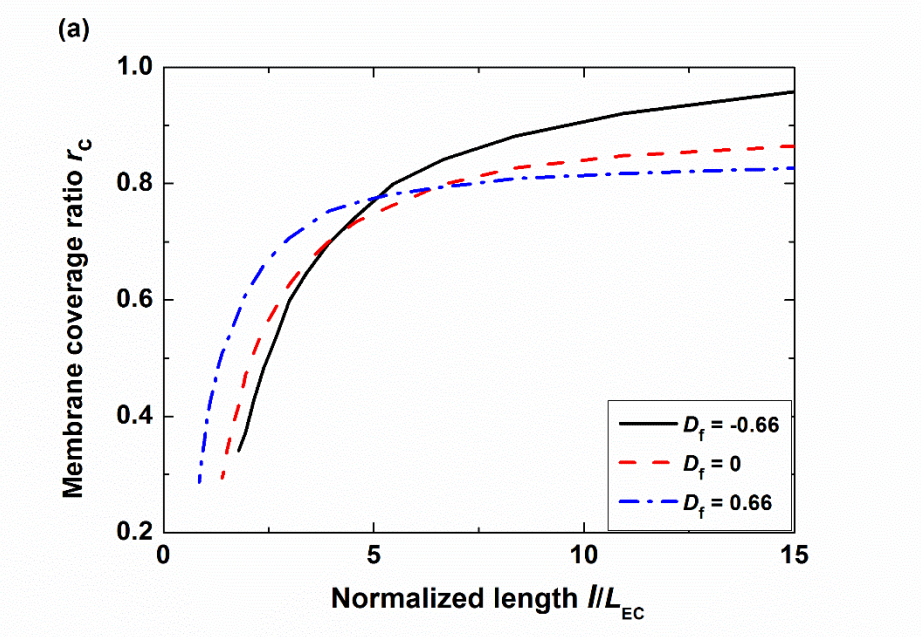

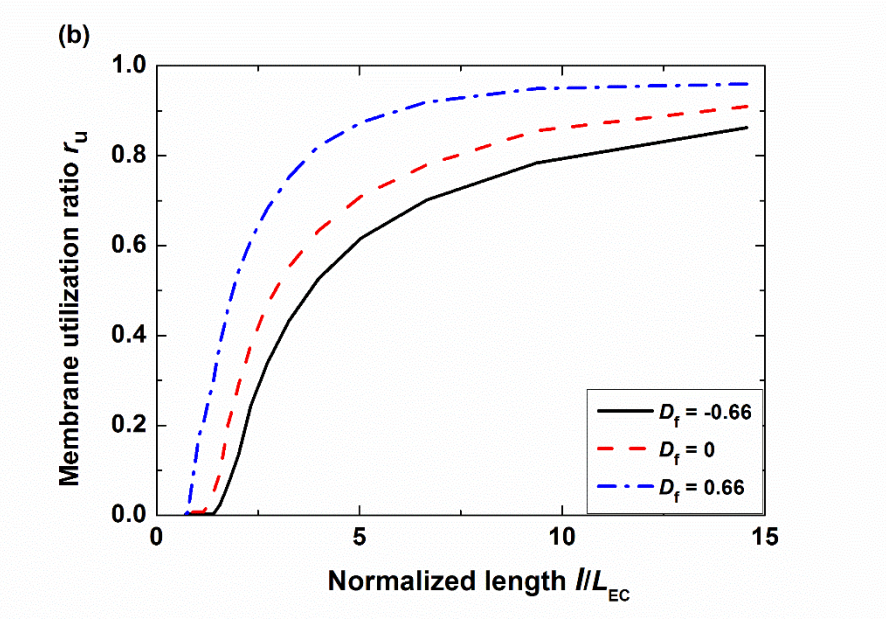

Figure 5.14: Modeling result of membrane coverage ratio (a) and utilization ratio (b) as a function of normalized length.

5.5 Summary

In this paper, a deployable device with subdural ECoG electrode array for minimally invasive monitoring of brain activity is introduced. The ECoG based device can be introduced into the subdural gap in a collapsed state and deployed by actuating wires. The membrane shapes under different device dimensions and surface conditions are modeled based on the minimization of elastic and surface energy to predict the bending angles and spatial coverage of the membrane. Experimental results are then obtained, showing good agreement with the modeling. The modeling method has been proven to predict the conformality and spatial coverage of membrane under various situations and therefore will help optimize mechanical design of the deployable device. Our work proves the early feasibility of the deployable ECoG device, however this and other related device architectures will enable new generations of

flexible and stretchable optoelectronic biomedical devices for smart minimally invasive surgical procedures.

Chapter 6

A Tunable Hemispherical Platform for Non-Stretching Curved Flexible Electronics and Optoelectronics

One major challenge in incorporating flexible electronics or optoelectronics on curved surfaces is the requirement of significant stretchability. We report a tunable platform for incorporating flexible and yet *non-stretching* device layers on a hemisphere. In this configuration, an array of planar petals contractively maps onto the surface of an inflatable hemisphere through elastocapillary interactions mediated by an interface liquid. A mechanical model is developed to elucidate the dependence of the conformality of the petal structures on their elastic modulus and thickness and the liquid surface tension. The modeling results are validated against experimental results obtained using petal structures of different thicknesses, restoring elastic spring elements of different spring constants, and liquids with different surface tension coefficients. Our platform will enable facile integration of *non-stretching* electronic and optoelectronic components prepared using established planar fabrication techniques on tunable hemispherical surfaces.

6.1 Background

There recently have been growing interests in so-called flexible electronics and optoelectronics for a wide variety of applications, in particular, smart biomedical devices, biomimetic imaging devices, [109], [110] wearable electronics, and robotics [111]. Some classes of the flexible device concepts, such as spherically curved focal plane detector arrays, require fabrication of electronics and optoelectronics on spherical surfaces. Such non-planar geometry is difficult to achieve in part because of the intrinsically planar nature of established micromachining techniques for semiconductor devices.

To deform a planar substrate into a spherical shape, one must stretch the center of the substrate isotropically and/or compress its perimeter tangentially. This is problematic because the resulting strains exceed the yield or fracture strength of most materials. To circumvent this issue, previous studies had to adopt a complex and challenging lift-off process sequence [112] or relied on "stretchable" conductors, such as thin interconnections that bend out of their planes, to accommodate the large strains [109], [113]–[115]. These highly customized fabrication and integration strategies may lead to increased costs and degraded mechanical reliability/performance (e.g., fill factor) of target devices and systems.

It is therefore of great interest to develop alternative mechanical architectures for spherical electronics or optoelectronics that utilize *non-stretching* substrates and conductors while still taking full advantage of established planar fabrication processes. In this article, we report the design, micro-mechanical modeling, and experimental validation of an alternative architecture

based on the contractive wrapping for possible applications in *tunable hemispherical* electronics. The architecture exploits high conformality and bendability of ultra-thin plastic, metal, or paper substrates and can deliver tunability often reserved only for devices incorporating stretchable substrates/conductors.

6.2 Tunable Platform Design

A basic design of our tunable hemispherical device is schematically illustrated in Fig. 6.1. Its main component is a flexible membrane (for example, a thin polyimide layer in the present study) that is patterned into a radial array of petals and then bends to wrap a hemisphere (Fig. 1a).

In conventional origami, a flat polygon of paper is folded along creases into a 3D object, a process that may be represented mathematically as a non-crossing isometric mapping. There, however, is no isometric folding of a flat surface into an object with infinitely many points of non-zero Gaussian curvature, such as a sphere. One approach to approximate a sphere is based on contractive wrapping[116]. In the petal wrappings employed in the present study, the contours of the petals are defined as

$$b = \tan^{-1}(\sin c \tan(\pi/n)) \qquad (6.1)$$

Here, b is the angular width of the petal at an angular location c ($0 \leqslant c \leqslant \pi$) measured along the meridian and n is the number of the petals used to approximate a sphere (Fig. 6.1a). The length contraction can be achieved by forming continuous infinitesimal crinkling, by juxtaposing “semi”-flat triangles like in a geodesic dome [117], or by targeting a sphere of

slightly larger diameter although at the expense of leaving finite gaps between some of the petals. The third approach is adopted here.

In the present implementation, a tunable hemisphere is formed and actuated by pneumatically inflating an elastomer membrane made of polydimethylsiloxane (PDMS). As depicted in Fig. 1c, the elastomer membrane is sandwiched between two clamping metal plates. The top plate has a center hole of radius R to define the hemisphere and the bottom plate has a small gas inlet for actuation. The capillary force exerted by a liquid confined in the gap between the elastomer membrane and each of the petals is used to maintain conformal contact while allowing the petals to glide freely on the elastomer membrane and the top metal plate as the elastomer membrane is inflated or deflated. The petals can *reversibly* return to their planar states when the elastomer membrane is deflated through the action of the peripheral elastic spring elements shown in Fig. 6.1. The elastic spring elements are made by bonding elastomeric joints on pre-folded segments of the polyimide film.

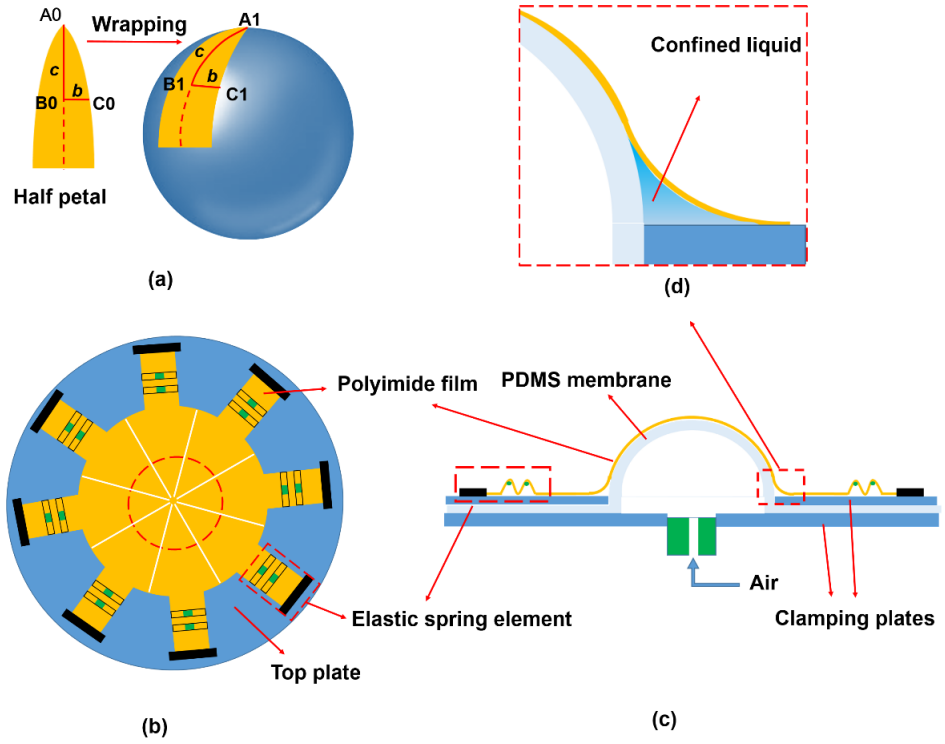

Figure 6.1: Conceptual design of the tunable hemispherical platform: (a) A single petal in its flat state and in its bent state to contractively map the surface of a hemisphere. (b) Top view of the tunable hemisphere platform with an array of the petals. (c) Side view of the hemisphere (d) Zoomed view near the edge of the hemisphere. The petal structures shown in (b, c) include extended strips that accommodate the elastic spring elements.

Figure 6.2a shows an optical image of the fabricated tunable hemispherical platform. An array of eight polyimide petals is conformally mapped on the surface of the elastomer membrane. As discussed before, small but finite gaps between the petals were intentionally incorporated into the design to eliminate crinkling or bulging associated with contractive mapping.

For further illustration, we also present in Fig. 6.2b a separate side view of a single isolated petal on the surface of a fully inflated elastomer membrane. The upper and middle portions of the petal are in good conformal contact with the elastomer membrane whereas the lower portion is lifted away from the membrane. The lower portion still maintains contact with the elastomer membrane and the top metal plate via a liquid bridge through its capillary interactions.

In actual integration of optoelectronic or electronic devices, one may first fabricate the devices using established planar fabrication techniques and then transfer bond them on petals made of thin polyimide films or comparable flexible "substrates." These petals are then mounted on the tunable hemisphere platform using a non-volatile liquid with negligible vapor pressure, such as ionic liquids.

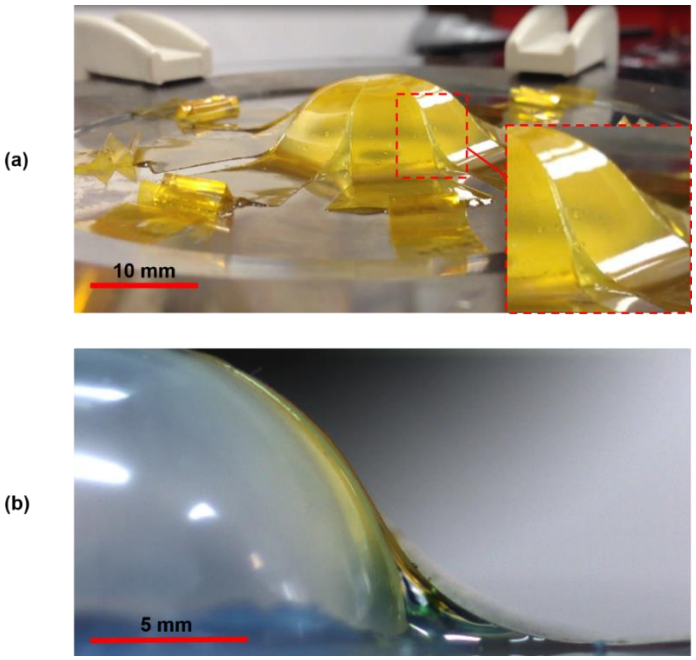

Figure 6.2: (a) Optical image of the tunable hemispherical platform with an array of 8 petals in contact with an inflated elastomer membrane. The inset shows a zoomed view of the two adjacent petals. (b) The

contour of a single isolated petal on the surfaces of a fully inflated elastomer hemisphere and the top metal plate.

6.3 Mechanical Model

A mechanical model is developed to predict the geometric contour of a single polyimide petal bent under elastocapillary interactions on the inflated elastomer membrane surface. As illustrated in Fig. 6.3a, the bent petal structure is approximated as two arc segments AB and BC with a radius of curvature R and r, respectively. The coverage angle θ of the petal segment AB is used as a quantitative measure of the conformality of the petals. The coverage angle and the two radii of curvature are interrelated: $r(1-\cos(\theta)) = R\cos(\theta)$. We determine the coverage angle θ from the minimization of the total energy, which is the sum of the elastic energy E_e and the interfacial energy E_s.

The elastic energy E_e, which is a sum of the strain energy of the bent petal and the elastic energy of the elastic spring element, is written as

$$E_e = \frac{2B_P}{R^2} S_{AB} + \frac{B_P}{r^2} S_{BC} + \frac{k}{2} dl^2 \quad (6.2)$$

Here, the arc segment AB is modeled as a thin shell with the principal curvature equal to $1/R$ and the arc segment BC is modeled with a curvature of $1/r$. The bending stiffness B_P for a film of thickness h, elastic modulus E_P, and Poisson ratio ν is $B_p = E_p h^3/12(1-\nu^2)$. The net horizontal elongation of the elastic spring element dl is given as

$$dl = l_{AB} + l_{BC} - l_{OC} = (R+r)(\theta - \sin(\theta)) \quad (6.3)$$

The interfacial energy of the liquid in the gap E_s is approximated by ignoring variations in the curvature along the long edges of the petal (Fig. 3b) as

$$E_s = \alpha\gamma_{lg}\left[2r^2(\tan(\frac{\theta}{2}) - \frac{\theta}{2}) + S_{AB} + S_{BC}\right] (4)$$

where γ_{lg} is the surface tension of the liquid in the unit of N/m. The associated interface areas S_{AB} and S_{BC} are obtained from

$$\begin{aligned} S_{AB} &= R^2 \int_0^{\theta} b(c)dc \\ S_{BC} &= R^2 \int_{\theta}^{\theta'} b(c)dc \end{aligned} \qquad (6.5)$$

where $\theta' = l_{AC}/R$ and b is the angular width of the petal that varies as a function of the meridian coordinate c as shown in Eq. (5.1) and Fig. 5.1. The liquid wetting factor α is defined as the ratio of the wetted surface area S_{CD} of the petal segment CD to the sum of the petal surface area S_{BC} and the air-liquid interface area at the gap S_{CDE}: $\alpha = S_{CD}/(S_{BC}+S_{CDE})$.

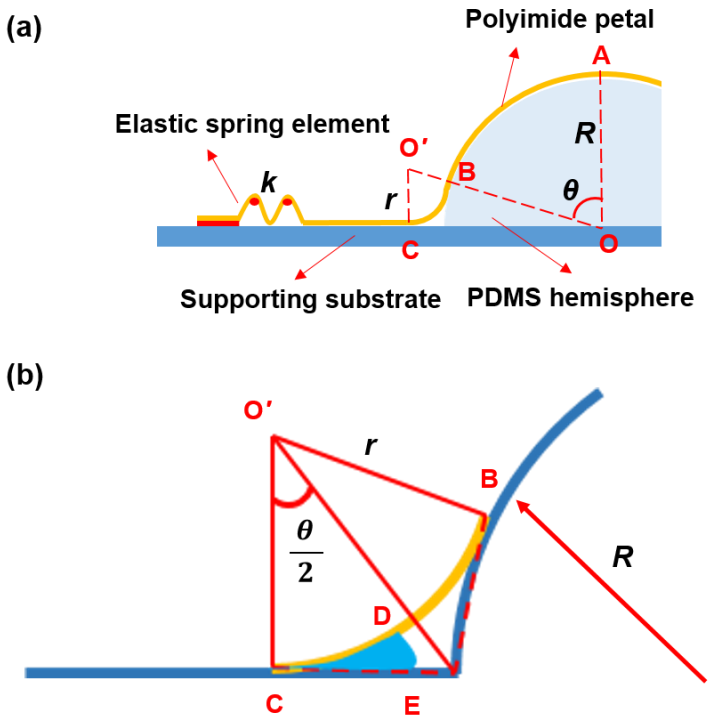

Figure 6.3: A geometric model of a petal structure and an elastic spring element designed to reversibly wrap the hemisphere through contractive mapping.

6.4 Experimental

To experimentally validate our model, we prepared thin polyimide films of varying thicknesses (3.6 ~ 12.7 μm) by spin coating a precursor solution (PI-2545, HD MicroSystems™) on a glass substrate at different speeds, curing them at 250 ℃ for 30 minutes, and then baking them for another 30 minutes at 350 ℃. The polyimide film has an elastic modulus of 2.5 GPa and a Poisson's ratio of 0.34.

Each of the cured polyimide films was peeled off from the glass substrate and cut into the petal structure with extended strips where elastic spring elements were to be formed. One such patterned polyimide film was mounted on the actuation platform incorporating an inflatable

elastomer membrane. A liquid was next applied to fill the gap between the polyimide petals and the elastomer membrane. For a given petal structure connected to an elastic spring element with a given spring constant, we performed experiments using three different liquids: water, glycerin and silicone oil with a surface tension coefficient γ_{lg} of 73 mN/m, 64 mN/m, and 20 mN/m, respectively. In each set of experiments, a set volume of liquid was first applied using a pipette. Additional amounts of the liquid were then added in a small increment to investigate the effect of the total liquid volume. A digital camera was used to capture the profiles of the polyimide petal under given experimental conditions, which were then analyzed using ImageJ. The spring constants of the elastic spring elements were measured independently by mounting each element between a mechanical stage and an analytic balance.

6.5 Results and Discussion

The elastocapillary length $L_{EC} = (B_P/\alpha\gamma_{lg})^{1/2}$ is used to describe the deformation of the polyimide petals under capillary interactions [118]. It can be roughly interpreted as a measure of the length of the polyimide petal segment that can stay flat (due to elasticity) while counteracting the capillary forces. To make our model for hemispherical platforms more generally applicable, we non-dimensionalize the hemisphere radius R and liquid volume V using the elastocapillary length L_{EC}: $\bar{R} = R/L_{EC}$ and $\bar{V} = V/L_{EC}^3$. In addition, we define the dimensionless spring constant $\bar{k} = k/\gamma_{lg}$ to help quantify the mutual interaction between the elasticity of the spring element and the capillary forces mediated by the interfacial liquid [119].

The contour of the polyimide petal structure is governed not only by the elastocapillary interactions but also by the elasticity of the spring element. For a given spring constant k, the smaller the elastocapillary length L_{EC} is, the larger the coverage angle θ is.

Figure 6.4 shows the modeled and experimentally measured coverage angles as a function of the normalized radius of the hemisphere. Larger normalized hemisphere radii (or smaller L_{EC}) result in larger values of θ, signifying better conformality. The spring element counteracts the capillary forces exerted on the petal, effectively increasing the elastocapillary length. The coverage angle, therefore, is reduced as the spring constant of the elastic spring element (or the dimensionless spring constant) increases (Figs. 6.4 and 6.5). Our approximate analytic model captures the two trends observed experimentally reasonably well.

The capillary effect itself is mainly a function of the surface tension coefficient γ_g. The higher the surface tension coefficient is, the smaller the elastocapillary length is. As a result, the petal has larger coverage angles for liquids with higher surface tension coefficients as illustrated in Fig. 6.5.

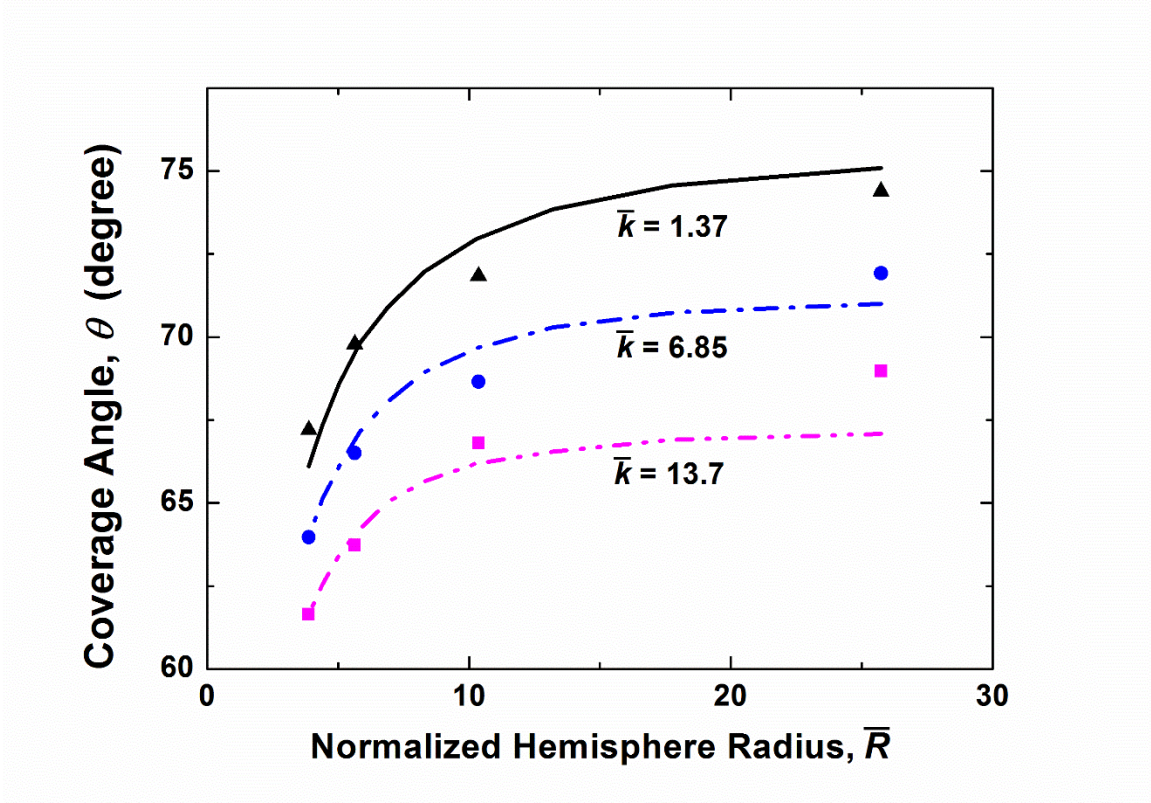

Figure 6.4: Modeling (lines) and experimental (symbols) results of the coverage angle θ for different values of the dimensionless spring constant $\bar{k}$. The results are plotted as a function of the normalized hemisphere radius $\bar{R}$.

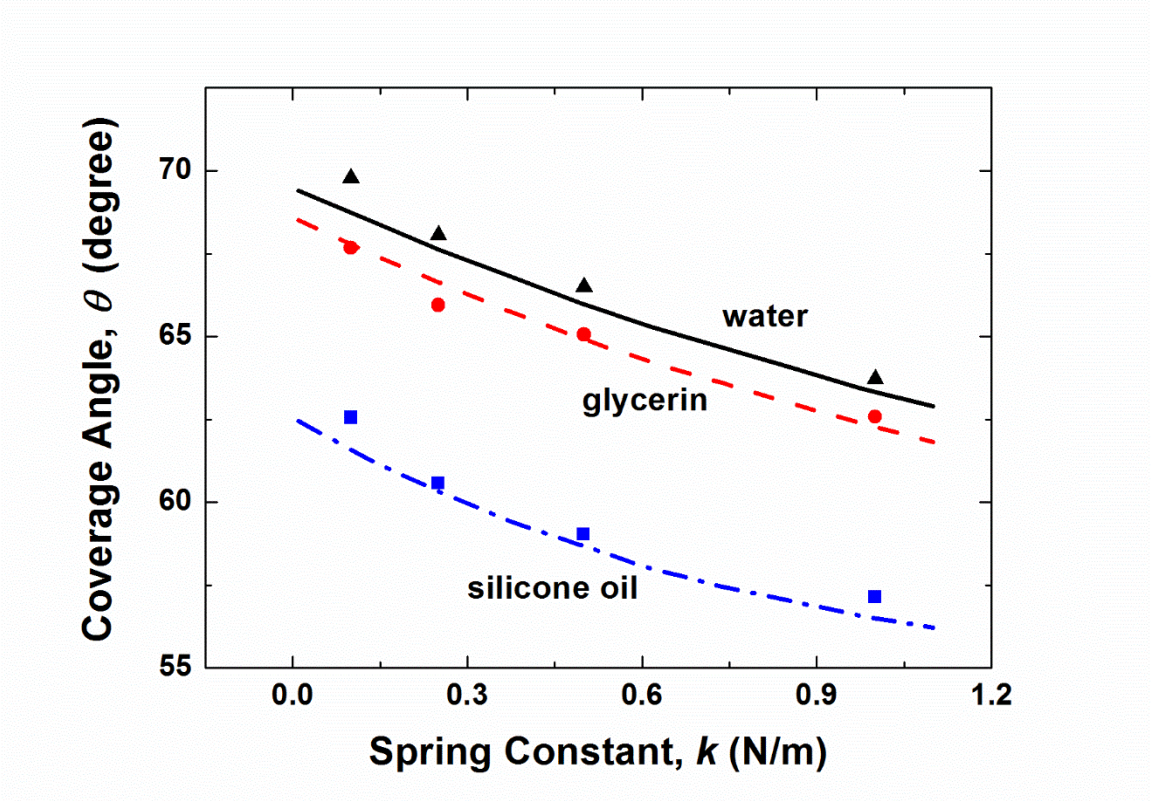

Figure 6.5: Modeling (lines) and experimental (symbols) results of the coverage angle θ for different liquids. The results are plotted as a function of the spring constant k of the elastic spring elements. The normalized hemisphere radii $\bar{R}$ are 5.5, 5.2 and 2.9 for water, glycerin and silicone oil, respectively.

Figure 6.6 shows the modeling results of the coverage angle as a function of the dimensionless spring constant for different values of the normalized radius. As shown above in Fig. 6.4 and Fig. 6.5, larger spring constants or smaller surface tension coefficients and thus larger values of the dimensionless spring constant lead to smaller coverage angles for a given normalized radius.

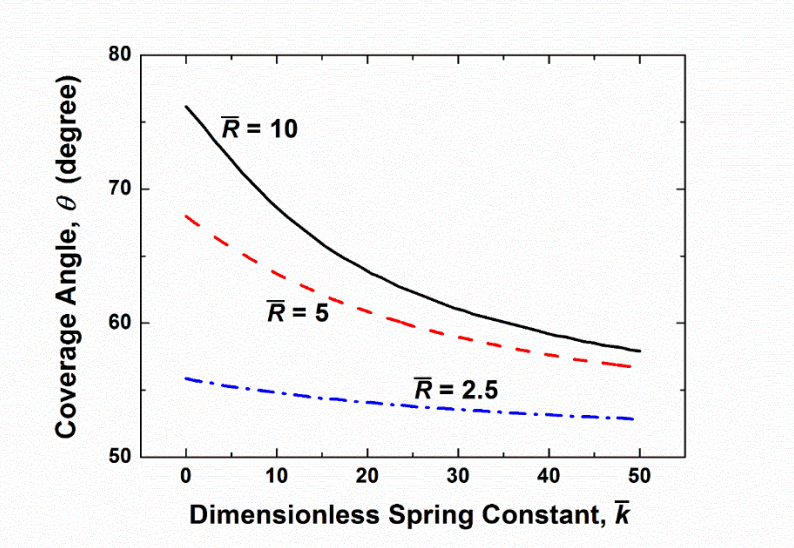

Figure 6.6: The predicted coverage angle θ as a function of the dimensionless spring constant $\bar{k}$ for different values of the normalized radius $\bar{R}$.

The liquid confined in the gap between the petal and the elastomer membrane forms liquid bridges with different shapes and wetting areas for different volumes of the liquid. When the liquid volume is insufficient to fill the entire gap, disconnected liquid bridges are formed around the edge of the hemisphere. As the liquid volume is increased, a larger area of the petal is wet. The increased wetting factor α leads to a smaller elastocapillary length, which in turn results in a larger coverage angle. Referring back to Fig. 6.3, we note that although both the wetted petal surface area S_{CD} and the liquid-gas interface area S_{CDE} increase with the liquid volume V, the former is much larger and therefore has a larger effect on the liquid wetting factor.

At sufficiently large liquid volumes, the entire petal structures are wetted by the liquid and thus the wetted petal surface area S_{CD} remains constant. Any accumulation of the excess liquid

in the gap causes the coverage angle to decrease with further increase in the liquid volume. The model prediction once again agrees well with the experimental data as shown in Fig. 6.7.

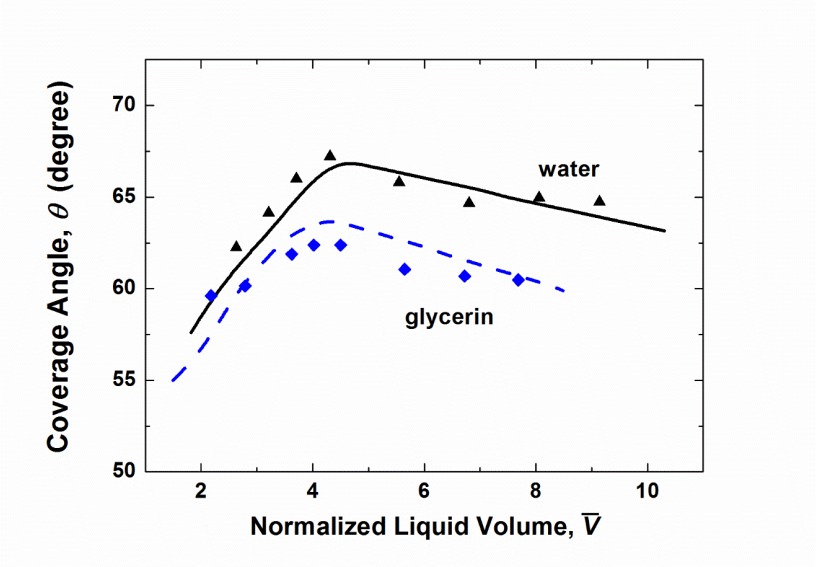

Figure 6.7: Modeling and experimental results of the coverage angle θ as a function of the normalized liquid volume $\bar{V}$ for two different liquids. The normalized hemisphere radii $\bar{R}$ are 5.5 and 5.2 for water and glycerin, respectively.

We use the coverage angle θ as a quantitative measure of the conformality of the petal. This coverage angle is governed by the normalized radius $\bar{R}$ and the dimensionless spring constant $\bar{k}$. For a given bending stiffness of the petal, one reaches a maximum coverage angle θ_m (or a minimum radius of curvature r_m) when $\bar{k} = 0$. This extreme condition allows us to separately illustrate the intrinsic effect of the bending stiffness on the conformality of the petal.

Figure 6.8 shows this theoretical maximum coverage angle θ_m as a function of the bending stiffness for two different liquids. From this plot one can determine the upper limit of the bending stiffness for a targeted coverage angle. The actual limit for elastic spring elements with

finite spring constants will be lower. The limit on the bending stiffness in turn constrains the acceptable elastic modulus and/or thickness of the petal. The elastic moduli of common flexible polymeric or rubbery materials are of the order of 100 MPa. With minimum practical layer thicknesses of the order of 1 μm, one has a practical lower bound in the bending stiffness of the order of 10^{-10} N m. As a practical upper bound, bending stiffness values of the order of 10^{-3} N m are obtained for very "stiff" films of thickness 50 μm and elastic modulus 100 GPa.

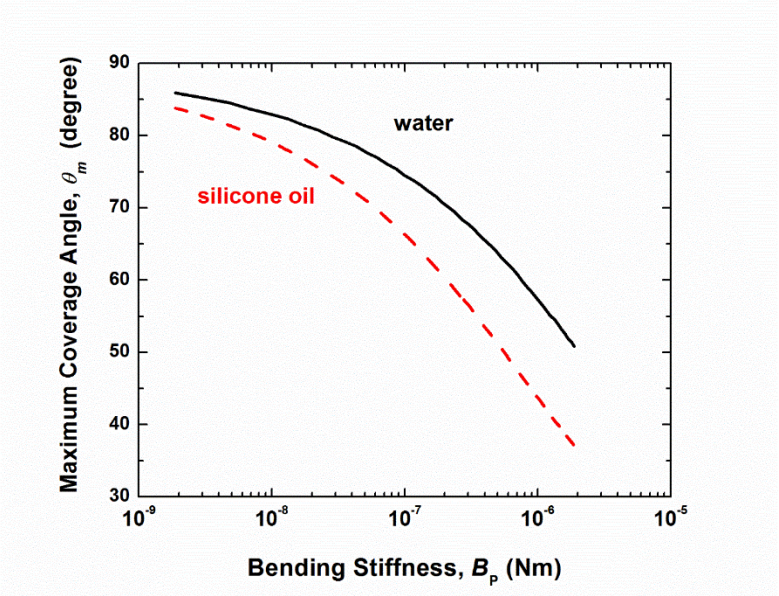

Figure 6. 8: Predicted values of the maximum coverage angle θ as a function of bending stiffness B_P for two different liquids.

When designing a specific system, one needs to choose a combination of the normalized hemisphere radius $\bar{R}$ and the dimensionless spring constant $\bar{k}$ consistent with a targeted value of the coverage angle θ. Figure 6.8 provides the maximum possible coverage angle, which one

may achieve in the limit $\bar{k} = 0$. In practice, the elastic spring elements with a finite spring constant ($k \neq 0$) are necessary to provide restoring forces and achieve reversible operations. Figure 6.9 shows predicted contour lines of the coverage angle as a function of the normalized hemisphere radius $\bar{R}$ and the dimensionless spring constant $\bar{k}$. For each contour line (that is, for a given targeted coverage angle), the normalized hemisphere radius increases with the dimensionless spring constant and diverges when $\bar{k}$ reaches a certain critical value.

When the dimensionless spring constant is relatively small (as an example, Region I for $\theta =$ 70 °in Fig. 6.9), the required normalized hemisphere radii are small and hence the petal bending stiffness B_p can be large. Recall that $\bar{R} \sim R / B_p^{0.5}$. A smaller spring constant is generally preferred because the resulting coverage angle is larger. However, "soft" elastic springs ($k < 0.1$ N/m) may not provide sufficient restoring forces to enable reliable reversible operations. This imposes a limit on the minimum acceptable value of the dimensionless spring constant $\bar{k}$. In the opposite limit of very "stiff" elastic spring elements (Region III in Fig. 6.9), the required normalized hemisphere radii are large and hence the petal bending stiffness B_p must be small. In this region, petals can only be made of very flexible materials with small elastic moduli and/or have very small thicknesses.

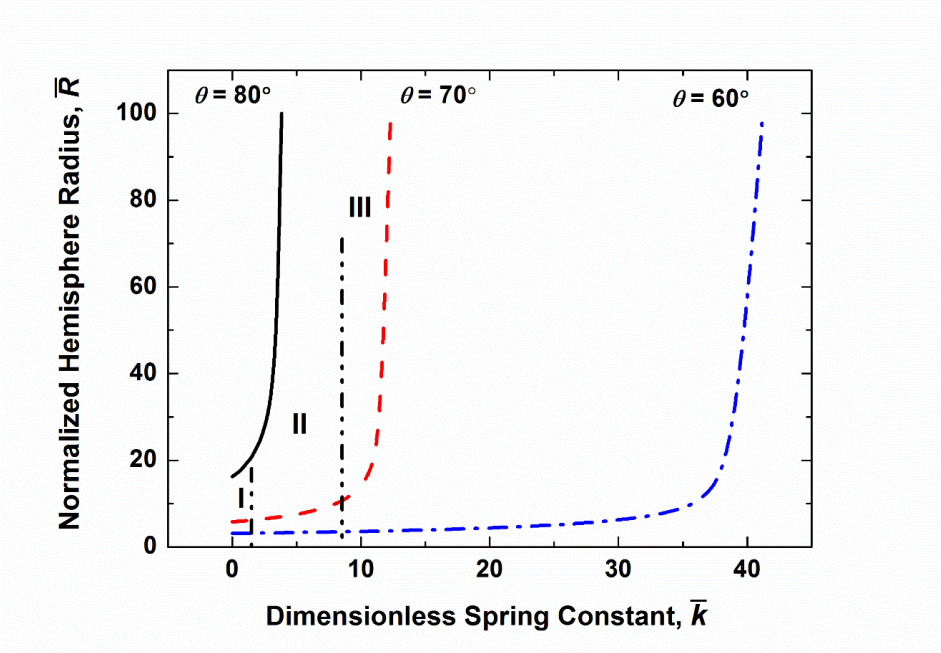

Figure 6.9: The predicted normalized radius $\bar{R}$ as a function of the dimensionless spring constant $\bar{k}$ for different values of the coverage angle θ.

6.5 Summary

In summary, a mechanical design of a tunable hemispherical platform for non-stretching substrates is reported for possible flexible electronic and optoelectronic applications. The tunable transformation of a planar substrate incorporating electronic or optoelectronic components into a hemisphere is achieved via contractive wrapping of petal-shaped structures on a pneumatically actuated elastomeric membrane. The conformality of the film wrapping on the hemispherical elastomer surface under various circumstances is predicted using an analytical model accounting for elasto-capillary interactions. The predicted values of the coverage angle and its dependence on the design parameters (the bending stiffness of the petal, the surface tension of the interface liquid, and the spring constant of the elastic spring elements) all show

good agreement with our experimental results. This study demonstrates the early feasibility of such non-stretching mechanical architectures for use in tunable hemispherical opto-electronic and other related devices and provides possible design parameter spaces.

Chapter 7

Summary and Recommendations

The present work demonstrates the concept of mechanical liquid interfaces as a new alternative for flexible, stretchable and deployable electronics. Mechanical liquid interfaces decouple direct loading from brittle rigid electronic components and thus allows the use of existing planar electronic components fabricated on “thick” or flexible yet non-stretching substrates. Such liquid interfaces also exploits and utilizes the elasto-capillary effect to enable non-stretching flexible and deployable devices on curved surfaces.

We extensively study the static and dynamic responses of the mechanical liquid interfaces for rigid devices to comprehensively understand the underlying physics and provide design tools for practical applications of such interfaces. We design a mechanical liquid interface based on capillary confined microscale liquid bridges and numerically investigate its quasi-static capillary forces, rupture behaviors under various loading scenarios. We also numerically and experimentally characterize the dynamic response of an axisymmetric liquid bridge being stretched at high velocity ranges. In addition, we present a numerical study for capillary self-alignment based on a confined liquid bridge to fully investigate its dynamic response and motion of the floating solid object.

We also design and characterize the mechanical liquid interfaces for non-stretching flexible and deployable devices. By utilizing the fluid solid interactions, the so-called elasto-capillary effect, we demonstrate a tunable hemispherical platform for non-stretching curved electronics. We then discuss a deployable planar device that can be introduced into a small space and then deploy to cover a large spatial area.

The following recommendations are made for future research on mechanical liquid interfaces for flexible, stretchable and deployable electronics.

In the scope of this research, the statics and dynamic response of the mechanical liquid interfaces have been numerically and experimentally studied. To provide a more comprehensive design tool for such related applications, further modeling and experiments can be conducted to gain insight on strain/stress distribution of the rigid component itself. A 2-D or 3-D simulation can be conducted to obtain the mechanics of the brittle rigid component and explore its limits regarding material strengths, dimensions and composition.

A further investigation on the dynamics of a mechanical interface with multiple liquid bridges can be performed. The dynamic response of the brittle substrate supported by the liquid interface can be numerically and/or experimentally characterized under various loading scenarios. This would help to understand the effects of such liquid interface exerted on the rigid substrate and provide a more mature design tool for future applications.

References

[1] A. J. Baca, J. H. Ahn, Y. Sun, M. A. Meitl, E. Menard, H.-S. Kim, W. M. Choi, D.-H. Kim, Y. Huang, and J. A. Rogers, "Semiconductor Wires and Ribbons for High- Performance Flexible Electronics," *Angew. Chem. Int. Ed.*, vol. 47, no. 30, pp. 5524–5542, Jul. 2008.

[2] Y. Sun and J. A. Rogers, "Inorganic Semiconductors for Flexible Electronics," *Adv. Mater.*, vol. 19, no. 15, pp. 1897–1916, Aug. 2007.

[3] H. Jiang, D. Y. Khang, J. Song, Y. Sun, Y. Huang, and J. A. Rogers, "Finite deformation mechanics in buckled thin films on compliant supports," *Proc. Natl. Acad. Sci.*, vol. 104, no. 40, pp. 15607–15612, Oct. 2007.

[4] D.-Y. Khang, H. Jiang, Y. Huang, and J. A. Rogers, "A stretchable form of single-crystal silicon for high-performance electronics on rubber substrates," *Science*, vol. 311, no. 5758, pp. 208–212, Jan. 2006.

[5] D. H. Kim, J. Song, W. M. Choi, H.-S. Kim, R. H. Kim, Z. Liu, Y. Y. Huang, K. C. Hwang, Y. Zhang, and J. A. Rogers, "Materials and noncoplanar mesh designs for integrated circuits with linear elastic responses to extreme mechanical deformations," *Proc. Natl. Acad. Sci.*, vol. 105, no. 48, pp. 18675–18680, Dec. 2008.

[6] K. Huang, R. Dinyari, G. Lanzara, J. Y. Kim, J. Feng, C. Vancura, F. K. Chang, and P. Peumans, "An Approach to Cost-Effective, Robust, Large-Area Electronics using Monolithic Silicon," in *Electron Devices Meeting, 2007. IEDM 2007. IEEE International*, 2007, pp. 217–220.

[7] D. S. Gray, J. Tien, and C. S. Chen, “High-Conductivity Elastomeric Electronics,” *Adv. Mater.*, vol. 16, no. 5, pp. 393–397, Mar. 2004.

[8] L. Puig, A. Barton, and N. Rando, “A review on large deployable structures for astrophysics missions,” *Acta Astronaut.*, vol. 67, no. 1–2, pp. 12–26, Jul. 2010.

[9] P. Gruber, S. Häuplik, B. Imhof, K. Özdemir, R. Waclavicek, and M. A. Perino, “Deployable structures for a human lunar base,” *Acta Astronaut.*, vol. 61, no. 1–6, pp. 484–495, Jun. 2007.

[10] K. Kuribayashi, K. Tsuchiya, Z. You, D. Tomus, M. Umemoto, T. Ito, and M. Sasaki, “Self-deployable origami stent grafts as a biomedical application of Ni-rich TiNi shape memory alloy foil,” *Mater. Sci. Eng. A*, vol. 419, no. 1–2, pp. 131–137, Mar. 2006.

[11] Z. Guo, K. Kim, G. Lanzara, N. Salowitz, P. Peumans, and F.-K. Chang, “Micro-fabricated, expandable temperature sensor network for macro-scale deployment in composite structures,” in *2011 IEEE Aerospace Conference*, 2011, pp. 1–6.

[12] B. L. Jordan, M. A. Batalin, and W. J. Kaiser, “NIMS RD: A Rapidly Deployable Cable Based Robot,” in *2007 IEEE International Conference on Robotics and Automation*, 2007, pp. 144–150.

[13] D. H. Kim, N. Lu, R. Ghaffari, Y.-S. Kim, S. P. Lee, L. Xu, J. Wu, R.-H. Kim, J. Song, Z. Liu, J. Viventi, B. de Graff, B. Elolampi, M. Mansour, M. J. Slepian, S. Hwang, J. D. Moss, S. M. Won, Y. Huang, B. Litt, and J. A. Rogers, “Materials for multifunctional balloon catheters with capabilities in cardiac electrophysiological mapping and ablation therapy,” *Nat. Mater.*, vol. 10, no. 4, pp. 316–323, Apr. 2011.

[14] G. H. Sandmann, P. Ahrens, C. Schaeffeler, J. S. Bauer, C. Kirchhoff, F. Martetschläger, D. Müller, S. Siebenlist, P. Biberthaler, U. Stöckle, and T. Freude, “Balloon osteoplasty—a

new technique for minimally invasive reduction and stabilisation of Hill–Sachs lesions of the humeral head: a cadaver study," *Int. Orthop.*, vol. 36, no. 11, pp. 2287–2291, Nov. 2012.

[15] B. Roman and J. Bico, "Elasto-capillarity: deforming an elastic structure with a liquid droplet," *J. Phys. Condens. Matter*, vol. 22, no. 49, p. 493101, 2010.

[16] C. Py, P. Reverdy, L. Doppler, J. Bico, B. Roman, and C. N. Baroud, "Capillary Origami: Spontaneous Wrapping of a Droplet with an Elastic Sheet," *Phys. Rev. Lett.*, vol. 98, no. 15, p. 156103, Apr. 2007.

[17] X. Guo, H. Li, B. Y. Ahn, E. B. Duoss, K. J. Hsia, J. A. Lewis, and R. G. Nuzzo, "Two- and three-dimensional folding of thin film single-crystalline silicon for photovoltaic power applications," *Proc. Natl. Acad. Sci.*, vol. 106, no. 48, pp. 20149–20154, Dec. 2009.

[18] D. h. Gracias, V. Kavthekar, J. c. Love, K. e. Paul, and G. m. Whitesides, "Fabrication of Micrometer-Scale, Patterned Polyhedra by Self-Assembly," *Adv. Mater.*, vol. 14, no. 3, pp. 235–238, Feb. 2002.

[19] X. Guo, H. Li, B. Y. Ahn, E. B. Duoss, K. J. Hsia, J. A. Lewis, and R. G. Nuzzo, "Two- and three-dimensional folding of thin film single-crystalline silicon for photovoltaic power applications," *Proc. Natl. Acad. Sci.*, vol. 106, no. 48, pp. 20149–20154, Dec. 2009.

[20] K. A. Brakke, "The Surface Evolver," *Exp. Math.*, vol. 1, no. 2, pp. 141–165, Jan. 1992.

[21] E. J. De Souza, M. Brinkmann, C. Mohrdieck, A. Crosby, and E. Arzt, "Capillary Forces between Chemically Different Substrates," *Langmuir*, vol. 24, no. 18, pp. 10161–10168, Sep. 2008.

[22] E. J. De Souza, M. Brinkmann, C. Mohrdieck, and E. Arzt, "Enhancement of Capillary Forces by Multiple Liquid Bridges," *Langmuir*, vol. 24, no. 16, pp. 8813–8820, Aug. 2008.

[23] G. Cha and Y. S. Ju, “Reversible thermal interfaces based on microscale dielectric liquid layers,” *Appl. Phys. Lett.*, vol. 94, no. 21, p. 211904, May 2009.

[24] G. Lian, C. Thornton, and M. J. Adams, “A Theoretical Study of the Liquid Bridge Forces between Two Rigid Spherical Bodies,” *J. Colloid Interface Sci.*, vol. 161, no. 1, pp. 138–147, Nov. 1993.

[25] C. W. Hirt and B. D. Nichols, “Volume of fluid (VOF) method for the dynamics of free boundaries,” *J. Comput. Phys.*, vol. 39, no. 1, pp. 201–225, Jan. 1981.

[26] D. Gao, N. B. Morley, and V. Dhir, “Numerical simulation of wavy falling film flow using VOF method,” *J. Comput. Phys.*, vol. 192, no. 2, pp. 624–642, Dec. 2003.

[27] D. Lörstad and L. Fuchs, “High-order surface tension VOF-model for 3D bubble flows with high density ratio,” *J. Comput. Phys.*, vol. 200, no. 1, pp. 153–176, Oct. 2004.

[28] S. Osher and R. P. Fedkiw, “Level Set Methods: An Overview and Some Recent Results,” *J. Comput. Phys.*, vol. 169, no. 2, pp. 463–502, May 2001.

[29] P. Yue, C. Zhou, J. J. Feng, C. F. Ollivier-Gooch, and H. H. Hu, “Phase-field simulations of interfacial dynamics in viscoelastic fluids using finite elements with adaptive meshing,” *J. Comput. Phys.*, vol. 219, no. 1, pp. 47–67, Nov. 2006.

[30] H. H. Hu, N. A. Patankar, and M. Y. Zhu, “Direct Numerical Simulations of Fluid–Solid Systems Using the Arbitrary Lagrangian–Eulerian Technique,” *J. Comput. Phys.*, vol. 169, no. 2, pp. 427–462, May 2001.

[31] R. Scardovelli and S. Zaleski, “Direct Numerical Simulation of Free-Surface and Interfacial Flow,” *Annu. Rev. Fluid Mech.*, vol. 31, no. 1, pp. 567–603, 1999.

[32] J. Donea, A. Huerta, J.-P. Ponthot, and A. Rodr ́guez-Ferran, "Arbitrary Lagrangian–Eulerian Methods," in *Encyclopedia of Computational Mechanics*, John Wiley & Sons, Ltd, 2004.

[33] D. H. Kim, J. Xiao, J. Song, Y. Huang, and J. A. Rogers, "Stretchable, curvilinear electronics based on inorganic materials," *Adv. Mater. Deerfield Beach Fla*, vol. 22, no. 19, pp. 2108–2124, May 2010.

[34] D.-H. Kim, R. Ghaffari, N. Lu, and J. A. Rogers, "Flexible and Stretchable Electronics for Biointegrated Devices," *Annu. Rev. Biomed. Eng.*, vol. 14, no. 1, pp. 113–128, 2012.

[35] Meseguer, J, "The Breaking of Axisymmetric Slender Liquid Bridges," *J Fluid Mech*, vol. 130, p. 123.

[36] R. M. S. M. Schulkes, "Nonlinear dynamics of liquid columns: A comparative study," *Phys. Fluids Fluid Dyn. 1989-1993*, vol. 5, no. 9, pp. 2121–2130, Sep. 1993.

[37] V. Tirtaatmadja and T. Sridhar, "A filament stretching device for measurement of extensional viscosity," *J. Rheol. 1978-Present*, vol. 37, no. 6, pp. 1081–1102, Nov. 1993.

[38] S. H. Spiegelberg, D. C. Ables, and G. H. McKinley, "The role of end-effects on measurements of extensional viscosity in filament stretching rheometers," *J. Non-Newton. Fluid Mech.*, vol. 64, no. 2–3, pp. 229–267, Jun. 1996.

[39] T. Y. Chen, J. A. Tsamopoulos, and R. J. Good, "Capillary bridges between parallel and non-parallel surfaces and their stability," *J. Colloid Interface Sci.*, vol. 151, no. 1, pp. 49–69, Jun. 1992.

[40] X. Zhang, R. S. Padgett, and O. A. Basaran, "Nonlinear deformation and breakup of stretching liquid bridges," *J. Fluid Mech.*, vol. 329, pp. 207–245, Dec. 1996.

[41] E. J. De Souza, M. Brinkmann, C. Mohrdieck, A. Crosby, and E. Arzt, “Capillary Forces between Chemically Different Substrates,” *Langmuir*, vol. 24, no. 18, pp. 10161–10168, Sep. 2008.

[42] D. J. Broesch, F. Dutka, and J. Frechette, “Curvature of Capillary Bridges as a Competition between Wetting and Confinement,” *Langmuir*, vol. 29, no. 50, pp. 15558–15564, Dec. 2013.

[43] E. J. De Souza, M. Brinkmann, C. Mohrdieck, and E. Arzt, “Enhancement of Capillary Forces by Multiple Liquid Bridges,” *Langmuir*, vol. 24, no. 16, pp. 8813–8820, Aug. 2008.

[44] H. Kusumaatmaja and R. Lipowsky, “Equilibrium Morphologies and Effective Spring Constants of Capillary Bridges,” *Langmuir*, vol. 26, no. 24, pp. 18734–18741, Dec. 2010.

[45] D. J. Broesch and J. Frechette, “From Concave to Convex: Capillary Bridges in Slit Pore Geometry,” *Langmuir*, vol. 28, no. 44, pp. 15548–15554, Nov. 2012.

[46] A. Virozub, N. Haimovich, and S. Brandon, “Three-Dimensional Simulations of Liquid Bridges between Two Cylinders: Forces, Energies, and Torques,” *Langmuir*, vol. 25, no. 22, pp. 12837–12842, Nov. 2009.

[47] G. Arutinov, E. C. P. Smits, P. Albert, P. Lambert, and M. Mastrangeli, “In-Plane Mode Dynamics of Capillary Self-Alignment,” *Langmuir*, vol. 30, no. 43, pp. 13092–13102, Nov. 2014.

[48] R. D. Gillette and D. C. Dyson, “Stability of fluid interfaces of revolution between equal solid circular plates,” *Chem. Eng. J.*, vol. 2, no. 1, pp. 44–54, 1971.

[49] J. Meseguer Ruiz and D. Rivas, “One-dimensional self-similar solution of the dynamics of axisymmetric slender liquid bridges,” *J. Fluid Mech.*, vol. 138, no. http://dx.doi.org/10.1017/S0022112084000185, pp. 417–429, Jan. 1984.

[50] H. A. S. M. Tjahjadi, “Satellite and subsatellite formation in capillary breakup,” *J. Fluid Mech.*, vol. 243, pp. 297 – 317, 1992.

[51] Chadov, A. V., Yakhnin, E. D., “Study of liquid transfer from one hard surface to another. I. Equilibrium transfer. Method of approximate calculation,” *Colloid J Russ. Acad. Sci.*, vol. 47, p. 817, 1979.

[52] Yakhnin, E. D., Chadov, A. V., “Study of the transfer of liquid from one solid surface to another. 2. Dynamic transfer,” *Colloid J Russ Acad Sci*, vol. 45, p. 1183, 1983.

[53] S. Kumar, “Liquid Transfer in Printing Processes: Liquid Bridges with Moving Contact Lines,” *Annu. Rev. Fluid Mech.*, vol. 47, no. 1, pp. 67–94, 2015.

[54] B. Hu, L. Xue, P. Yang, and Y. Han, “Variable-Focus Liquid Microlenses with Adjustable 3-D Curved Housings,” *Langmuir*, vol. 26, no. 9, pp. 6350–6356, May 2010.

[55] Y. Jia, G. Cha, and Y. S. Ju, “Switchable Thermal Interfaces Based on Discrete Liquid Droplets,” *Micromachines*, vol. 3, no. 1, pp. 10–20, Jan. 2012.

[56] G. Cha and Y. S. Ju, “Reversible thermal interfaces based on microscale dielectric liquid layers,” *Appl. Phys. Lett.*, vol. 94, no. 21, p. 211904, May 2009.

[57] J. V. I. Timonen, M. Latikka, L. Leibler, R. H. A. Ras, and O. Ikkala, “Switchable Static and Dynamic Self-Assembly of Magnetic Droplets on Superhydrophobic Surfaces,” *Science*, vol. 341, no. 6143, pp. 253–257, Jul. 2013.

[58] Y. Zhan, G. Cha, J. Zhuang, Y. Jia, and Y. S. Ju, “Microscale liquid-based mechanical elements for multifunctional integration,” *J. Compos. Mater.*, vol. 47, no. 1, pp. 65–75, Jan. 2013.

[59] A. Sanz and J. L. Diez, “Non-axisymmetric oscillations of liquid bridges,” *J. Fluid Mech.*, vol. 205, pp. 503–521, Aug. 1989.

[60] A. Sanz, “The influence of the outer bath in the dynamics of axisymmetric liquid bridges,” *J. Fluid Mech.*, vol. 156, pp. 101–140, Jul. 1985.

[61] J. Tsamopoulos, T.-Y. Chen, and A. Borkar, “Viscous oscillations of capillary bridges,” *J. Fluid Mech.*, vol. 235, pp. 579–609, Feb. 1992.

[62] J. B. Valsamis, M. Mastrangeli, and P. Lambert, “Vertical excitation of axisymmetric liquid bridges,” *Eur. J. Mech. - BFluids*, vol. 38, pp. 47–57, Mar. 2013.

[63] R. Kröger, S. Berg, A. Delgado, and H. J. Rath, “Stretching behaviour of large polymeric and Newtonian liquid bridges in plateau simulation,” *J. Non-Newton. Fluid Mech.*, vol. 45, no. 3, pp. 385–400, Dec. 1992.

[64] J. Eggers and T. F. Dupont, “Drop formation in a one-dimensional approximation of the Navier–Stokes equation,” *J. Fluid Mech.*, vol. 262, pp. 205–221, Oct. 1994.

[65] O. E. Yildirim and O. A. Basaran, “Deformation and breakup of stretching bridges of Newtonian and shear-thinning liquids: comparison of one- and two-dimensional models,” *Chem. Eng. Sci.*, vol. 56, no. 1, pp. 211–233, Jan. 2001.

[66] J. Donea, A. Huerta, J.-P. Ponthot, and A. Rodr ́guez-Ferran, “Arbitrary Lagrangian–Eulerian Methods,” in *Encyclopedia of Computational Mechanics*, John Wiley & Sons, Ltd, 2004.

[67] H. H. Hu, N. A. Patankar, and M. Y. Zhu, “Direct Numerical Simulations of Fluid–Solid Systems Using the Arbitrary Lagrangian–Eulerian Technique,” *J. Comput. Phys.*, vol. 169, no. 2, pp. 427–462, May 2001.

[68] R. Scardovelli and S. Zaleski, “Direct Numerical Simulation of Free-Surface and Interfacial Flow,” *Annu. Rev. Fluid Mech.*, vol. 31, no. 1, pp. 567–603, 1999.

[69] G. P. Association, *Physical Properties of Glycerine and Its Solutions*. Glycerine Producers' Association, 1963.

[70] S. R. Coriell, S. C. Hardy, and M. R. Cordes, "Stability of liquid zones," *J. Colloid Interface Sci.*, vol. 60, no. 1, pp. 126–136, Jun. 1977.

[71] J. H. Snoeijer and B. Andreotti, "Moving Contact Lines: Scales, Regimes, and Dynamical Transitions," *Annu. Rev. Fluid Mech.*, vol. 45, no. 1, pp. 269–292, 2013.

[72] S. Dodds, M. Carvalho, and S. Kumar, "Stretching liquid bridges with moving contact lines: The role of inertia," *Phys. Fluids 1994-Present*, vol. 23, no. 9, p. 092101, Sep. 2011.

[73] M. Mastrangeli, G. Arutinov, E. C. P. Smits, and P. Lambert, "Modeling capillary forces for large displacements," *Microfluid. Nanofluidics*, vol. 18, no. 4, pp. 695–708, Sep. 2014.

[74] K. Sato, K. Ito, S. Hata, and A. Shimokohbe, "Self-alignment of microparts using liquid surface tension—behavior of micropart and alignment characteristics," *Precis. Eng.*, vol. 27, no. 1, pp. 42–50, Jan. 2003.

[75] H. O. Jacobs, A. R. Tao, A. Schwartz, D. H. Gracias, and G. M. Whitesides, "Fabrication of a Cylindrical Display by Patterned Assembly," *Science*, vol. 296, no. 5566, pp. 323–325, Apr. 2002.

[76] U. Srinivasan, D. Liepmann, and R. T. Howe, "Microstructure to substrate self-assembly using capillary forces," *J. Microelectromechanical Syst.*, vol. 10, no. 1, pp. 17–24, Mar. 2001.

[77] R. R. A. Syms, E. M. Yeatman, V. M. Bright, and G. M. Whitesides, "Surface tension-powered self-assembly of microstructures - the state-of-the-art," *J. Microelectromechanical Syst.*, vol. 12, no. 4, pp. 387–417, Aug. 2003.

[78] G. Arutinov, M. Mastrangeli, E. C. P. Smits, G. van Heck, J. M. J. den Toonder, and A. Dietzel, "Foil-to-Foil System Integration Through Capillary Self-Alignment Directed by Laser Patterning," *J. Microelectromechanical Syst.*, vol. 24, no. 1, pp. 126–133, Feb. 2015.

[79] V. Sariola, M. Jääskeläinen, and Q. Zhou, "Hybrid Microassembly Combining Robotics and Water Droplet Self-Alignment," *IEEE Trans. Robot.*, vol. 26, no. 6, pp. 965–977, Dec. 2010.

[80] "Wiley-IEEE Press: Robotic Micro-Assembly - Micha ël Gauthier, St éphane Regnier." [Online]. Available: http://www.wiley.com/WileyCDA/WileyTitle/productCd-0470484179,miniSiteCd-IEEE2.html. [Accessed: 17-Dec-2015].

[81] T. Fukushima, E. Iwata, Y. Ohara, M. Murugesan, J. Bea, K. Lee, T. Tanaka, and M. Koyanagi, "Multichip-to-Wafer Three-Dimensional Integration Technology Using Chip Self-Assembly With Excimer Lamp Irradiation," *IEEE Trans. Electron Devices*, vol. 59, no. 11, pp. 2956–2963, Nov. 2012.

[82] J. Berthier, S. Mermoz, K. Brakke, L. Sanchez, C. Fr étigny, and L. D. Cioccio, "Capillary self-alignment of polygonal chips: a generalization for the shift-restoring force," *Microfluid. Nanofluidics*, vol. 14, no. 5, pp. 845–858, Dec. 2012.

[83] J. B. V. M. Mastrangeli, "Lateral Capillary Forces of Cylindrical Fluid Menisci: A Comprehensive Quasi-Static Study," *J. Micromechanics Microengineering*, vol. 20, no. 7, p. 075041, 2010.

[84] S. Gao and Y. Zhou, "Self-alignment of micro-parts using capillary interaction: Unified modeling and misalignment analysis," *Microelectron. Reliab.*, vol. 53, no. 8, pp. 1137–1148, Aug. 2013.

[85] J. Berthier, K. Brakke, F. Grossi, L. Sanchez, and L. D. Cioccio, "Self-alignment of silicon chips on wafers: A capillary approach," *J. Appl. Phys.*, vol. 108, no. 5, p. 054905, Sep. 2010.

[86] P. Lambert, M. Mastrangeli, J.-B. Valsamis, and G. Degrez, “Spectral analysis and experimental study of lateral capillary dynamics for flip-chip applications,” *Microfluid. Nanofluidics*, vol. 9, no. 4–5, pp. 797–807, Mar. 2010.

[87] T. Fukushima, E. Iwata, Y. Ohara, M. Murugesan, J. Bea, K. Lee, T. Tanaka, and M. Koyanagi, “Multichip-to-Wafer Three-Dimensional Integration Technology Using Chip Self-Assembly With Excimer Lamp Irradiation,” *IEEE Trans. Electron Devices*, vol. 59, no. 11, pp. 2956–2963, Nov. 2012.

[88] G. Arutinov, E. C. P. Smits, M. Mastrangeli, G. van Heck, J. van den Brand, H. F. M. Schoo, and A. Dietzel, “Capillary self-alignment of mesoscopic foil components for sensor-systems-in-foil,” *J. Micromechanics Microengineering*, vol. 22, no. 11, p. 115022, 2012.

[89] G. Arutinov, M. Mastrangeli, E. C. P. Smits, H. F. M. Schoo, J. Brugger, and A. Dietzel, “Dynamics of capillary self-alignment for mesoscopic foil devices,” *Appl. Phys. Lett.*, vol. 102, no. 14, p. 144101, Apr. 2013.

[90] M. Mastrangeli, G. Arutinov, E. C. P. Smits, and P. Lambert, “Modeling capillary forces for large displacements,” *Microfluid. Nanofluidics*, vol. 18, no. 4, pp. 695–708, Sep. 2014.

[91] J. M. Drake and J. Klafter, “Dynamics of confined molecular systems,” *Phys. Today*, vol. 43, pp. 46–55, May 1990.

[92] G. Arutinov, E. C. P. Smits, P. Albert, P. Lambert, and M. Mastrangeli, “In-Plane Mode Dynamics of Capillary Self-Alignment,” *Langmuir*, vol. 30, no. 43, pp. 13092–13102, Nov. 2014.

[93] A. Carlson, M. Do-Quang, and G. Amberg, “Modeling of dynamic wetting far from equilibrium,” *Phys. Fluids 1994-Present*, vol. 21, no. 12, p. 121701, Dec. 2009.

[94] S. Guo, M. Gao, X. Xiong, Y. J. Wang, X. Wang, P. Sheng, and P. Tong, "Direct Measurement of Friction of a Fluctuating Contact Line," *Phys. Rev. Lett.*, vol. 111, no. 2, p. 026101, Jul. 2013.

[95] A. Carlson, G. Bellani, and G. Amberg, "Universality in dynamic wetting dominated by contact line friction," *Phys. Rev. E*, vol. 85, no. 4, Apr. 2012.

[96] A. Carlson, G. Bellani, and G. Amberg, *Measuring contact line dissipation in dynamic wetting*. 200AD.

[97] J. C. Bird, S. Mandre, and H. A. Stone, "Short-Time Dynamics of Partial Wetting," *Phys. Rev. Lett.*, vol. 100, no. 23, p. 234501, Jun. 2008.

[98] B. Mimoun, V. Henneken, A. van der Horst, and R. Dekker, "Flex-to-Rigid (F2R): A Generic Platform for the Fabrication and Assembly of Flexible Sensors for Minimally Invasive Instruments," *IEEE Sens. J.*, vol. 13, no. 10, pp. 3873–3882, 2013.

[99] D. H. Kim, N. Lu, R. Ma, Y.-S. Kim, R.-H. Kim, S. Wang, J. Wu, S. M. Won, H. Tao, A. Islam, K. J. Yu, T. Kim, R. Chowdhury, M. Ying, L. Xu, M. Li, H.-J. Chung, H. Keum, M. McCormick, P. Liu, Y.-W. Zhang, F. G. Omenetto, Y. Huang, T. Coleman, and J. A. Rogers, "Epidermal Electronics," *Science*, vol. 333, no. 6044, pp. 838–843, Aug. 2011.

[100] C. Py, P. Reverdy, L. Doppler, J. Bico, B. Roman, and C. N. Baroud, "Capillary Origami: Spontaneous Wrapping of a Droplet with an Elastic Sheet," *Phys. Rev. Lett.*, vol. 98, no. 15, p. 156103, Apr. 2007.

[101] X. Guo, H. Li, B. Y. Ahn, E. B. Duoss, K. J. Hsia, J. A. Lewis, and R. G. Nuzzo, "Two- and three-dimensional folding of thin film single-crystalline silicon for photovoltaic power applications," *Proc. Natl. Acad. Sci.*, vol. 106, no. 48, pp. 20149–20154, Dec. 2009.

[102] L. D. Landau and E. M. Lifshitz, *Theory of Elasticity*. Elsevier, 1986.

[103] S. Timoshenko and S. WOINOWSKY-KRIEGER, *Theory of Plates and Shells ... Second Edition*. McGraw-Hill Book Company, 1959.

[104] "Surface Energy Data for Polyimide." Kapton, CAS # 25038-81-7.

[105] L. J. Matienzo and F. D. Egitto, "Polymer oxidation downstream from oxygen microwave plasmas," *Polym. Degrad. Stab.*, vol. 35, no. 2, pp. 181–192, 1992.

[106] K. L. Mittal, *Polymer Surface Modification: Relevance to Adhesion*. BRILL, 2009.

[107] "Polyimide Film General Specifications." Dupont Kapton, Bulletin GS-96-7.

[108] Z. J. Chen, W. C. Broaddus, R. R. Viswanathan, R. Raghavan, and G. T. Gillies, "Intraparenchymal drug delivery via positive-pressure infusion: experimental and modeling studies of poroelasticity in brain phantom gels," *IEEE Trans. Biomed. Eng.*, vol. 49, no. 2, pp. 85–96, 2002.

[109] Y. M. Song, Y. Xie, V. Malyarchuk, J. Xiao, I. Jung, K.-J. Choi, Z. Liu, H. Park, C. Lu, R.-H. Kim, R. Li, K. B. Crozier, Y. Huang, and J. A. Rogers, "Digital cameras with designs inspired by the arthropod eye," *Nature*, vol. 497, no. 7447, pp. 95–99, May 2013.

[110] D. Floreano, R. Pericet-Camara, S. Viollet, F. Ruffier, A. Brückner, R. Leitel, W. Buss, M. Menouni, F. Expert, R. Juston, M. K. Dobrzynski, G. L'Eplattenier, F. Recktenwald, H. A. Mallot, and N. Franceschini, "Miniature curved artificial compound eyes," *Proc. Natl. Acad. Sci.*, vol. 110, no. 23, pp. 9267–9272, Jun. 2013.

[111] M. Kaltenbrunner, T. Sekitani, J. Reeder, T. Yokota, K. Kuribara, T. Tokuhara, M. Drack, R. Schwödiauer, I. Graz, S. Bauer-Gogonea, S. Bauer, and T. Someya, "An ultra-lightweight design for imperceptible plastic electronics," *Nature*, vol. 499, no. 7459, pp. 458–463, Jul. 2013.

[112] P. I. Hsu, R. Bhattacharya, H. Gleskova, M. Huang, Z. Xi, Z. Suo, S. Wagner, and J. C. Sturm, "Thin-film transistor circuits on large-area spherical surfaces," *Appl. Phys. Lett.*, vol. 81, no. 9, pp. 1723–1725, Aug. 2002.

[113] P. J. Hung, K. Jeong, G. L. Liu, and L. P. Lee, "Microfabricated suspensions for electrical connections on the tunable elastomer membrane," *Appl. Phys. Lett.*, vol. 85, no. 24, pp. 6051–6053, Dec. 2004.

[114] R. Dinyari, S. B. Rim, K. Huang, P. B. Catrysse, and P. Peumans, "Curving monolithic silicon for nonplanar focal plane array applications," *Appl. Phys. Lett.*, vol. 92, no. 9, p. 091114, Mar. 2008.

[115] G. Shin, I. Jung, V. Malyarchuk, J. Song, S. Wang, H. C. Ko, Y. Huang, J. S. Ha, and J. A. Rogers, "Micromechanics and Advanced Designs for Curved Photodetector Arrays in Hemispherical Electronic-Eye Cameras," *Small*, vol. 6, no. 7, pp. 851–856, 2010.

[116] E. D. Demaine, M. L. Demaine, J. Iacono, and S. Langerman, "Wrapping spheres with flat paper," *Comput. Geom.*, vol. 42, no. 8, pp. 748–757, Oct. 2009.

[117] R. A. Street, W. S. Wong, and R. Lujan, "Curved electronic pixel arrays using a cut and bend approach," *J. Appl. Phys.*, vol. 105, no. 10, p. 104504, May 2009.

[118] B. Roman and J. Bico, "Elasto-capillarity: deforming an elastic structure with a liquid droplet," *J. Phys. Condens. Matter*, vol. 22, no. 49, p. 493101, Dec. 2010.

[119] S. Jung, C. Clanet, and J. W. M. Bush, "Capillary instability on an elastic helix," *Soft Matter*, vol. 10, no. 18, pp. 3225–3228, Apr. 2014.